

# IsoDAR@Yemilab: Preliminary Design Report - Volume I: Cyclotron Driver

*Abstract:* This Preliminary Design Report (PDR) describes the IsoDAR electron-antineutrino source in two volumes which are mostly site-independent and describe the cyclotron driver, providing a 10 mA proton beam, and the medium energy beam transport line and target, respectively. The IsoDAR driver and target will produce a mole of electron-antineutrinos over the course of five years. Paired with a kton-scale liquid scintillator detector, it will enable an impressive particle physics program including searches for new symmetries, new interactions and new particles. Here in Volume I, we describe the driver, which includes the ion source, low energy beam transport, and cyclotron. The latter features radiofrequency quadrupole (RFQ) direct axial injection and represents the first accelerator purpose-built to make use of so-called vortex motion.

Section Editors (in alphabetical order): M. Abs<sup>1</sup>, J.R Alonso<sup>2</sup>, J.M. Conrad<sup>2</sup>, S.J.B. Engebretson<sup>2</sup>, E. Forton<sup>1</sup>, A. Herrod<sup>1</sup>, D. Joassin<sup>1</sup>, J. Moon<sup>2</sup>, S. de Neuter<sup>1</sup>, E. Van der Kraaij<sup>1</sup>, G. Wéry<sup>1</sup>, D. Winklehner<sup>2</sup>, E. Winkler<sup>2</sup>

*for the IsoDAR collaboration*

<sup>1</sup>Ion Beam Applications, 3 chemin du cyclotron Louvain-la-Neuve, BELGIUM

<sup>2</sup>Massachusetts Institute of Technology, 77 Massachusetts Ave. Cambridge, MA, USA

*Corresponding Authors: Joshua Spitz (spitzj@umich.edu) and Daniel Winklehner (winklehn@mit.edu)*

V2.0

# Contents

<b>1</b>	<b>Introduction</b>	<b>5</b>
1.1	The IsoDAR Physics Case . . . . .	7
1.1.1	Fluxes in IsoDAR . . . . .	7
1.1.2	New Particles: Experimentally and Theoretically Motivated . . . . .	8
1.1.3	New Symmetries: Strong CP Violation and the QCD Axion . . . . .	9
1.1.4	New Interactions: Tests via Precision Electroweak Physics . . . . .	10
1.2	Requirements for the Proton Driver . . . . .	11
1.3	Overview of the Accelerator Layout . . . . .	11
<b>2</b>	<b>Design of the Front End</b>	<b>13</b>
2.1	The Ion Source . . . . .	13
2.1.1	Operating Principle . . . . .	13
2.1.2	Mechanical Design . . . . .	15
2.1.2.1	MIST-2 vs. MIST-1 . . . . .	15
2.1.3	Electrical Design . . . . .	16
2.1.4	Beam Dynamics . . . . .	17
2.1.5	Performance . . . . .	18
2.1.5.1	Goals & Measurement Methods . . . . .	18
2.1.5.2	Optimization of Ion Source Parameters . . . . .	18
2.1.5.3	Latest Optimized Results . . . . .	19
2.1.5.4	Magnet Study . . . . .	20
2.1.5.5	Results with the MIST-2 back plate . . . . .	20
2.1.6	Risks and Mitigation . . . . .	21
2.2	The Low Energy Beam Transport . . . . .	22
2.2.1	Design Overview . . . . .	22
2.2.2	Beam Steering & Chopping . . . . .	23
2.2.3	Beam Dynamics . . . . .	23
2.2.4	Risks and Mitigations . . . . .	25

2.3	The Radiofrequency Quadrupole . . . . .	26
2.3.1	Technical Design . . . . .	26
2.3.2	Beam Dynamics . . . . .	27
2.3.3	Risks and Mitigation . . . . .	28
<b>3</b>	<b>Design of the Cyclotron</b>	<b>29</b>
3.1	Magnet Yoke . . . . .	29
3.1.1	Design and Fabrication of the Cyclotron Magnet . . . . .	30
3.2	Cyclotron magnetic performance . . . . .	32
3.2.1	Isochronization . . . . .	33
3.2.2	Risks and Mitigation . . . . .	34
3.3	Interface with the RFQ . . . . .	35
3.4	Central Region . . . . .	37
3.4.1	Spiral Inflector Overview & Design Considerations . . . . .	39
3.4.2	Designing the Inflector . . . . .	39
3.4.3	Geometric Refinements . . . . .	40
3.4.4	Characterization of Spiral Inflector . . . . .	41
3.4.5	Orbit Matching and Beam Centering . . . . .	43
3.4.6	Low Energy Collimation . . . . .	45
3.4.7	Risks and Mitigation . . . . .	45
3.5	Vacuum Chamber . . . . .	46
3.5.1	Risks and Mitigation . . . . .	47
3.6	Coil configuration . . . . .	47
3.7	Cyclotron RF System . . . . .	47
3.8	RF Cavities (Dees, Stems and Liners) . . . . .	48
3.8.1	Integration of preliminary central region in RF Cavities . . . . .	49
3.8.2	RFQ Integration in RF Cavities . . . . .	50
3.8.3	RFQ getter pumps in RF Cavities . . . . .	51
3.8.4	RF Cavities design optimization . . . . .	52
3.8.4.1	Performance requirement target . . . . .	52
3.8.4.2	Parametric optimization of the design . . . . .	53
3.8.5	RF cavity computation results . . . . .	54

3.8.5.1	Detailed power analysis . . . . .	56
3.8.5.2	Radial voltage dependency . . . . .	59
3.8.6	RF Tuning System . . . . .	59
3.8.7	RF Amplifiers . . . . .	59
3.8.8	RF Lines and Couplers . . . . .	60
3.8.9	LLRF Electronics . . . . .	61
3.8.10	Risks and Mitigation . . . . .	62
3.9	Cyclotron Particle Simulations . . . . .	63
3.9.1	Fieldmaps . . . . .	63
3.9.2	Probes . . . . .	63
3.9.3	Simulation Results . . . . .	64
3.9.4	Electrostatic Extraction Channels . . . . .	65
3.9.5	Magnetic Extraction Channels . . . . .	66
3.9.6	Risks and Mitigation . . . . .	67
<b>4</b>	<b>Installation in the Yemilab Setting</b>	<b>68</b>
4.1	Transport of Components . . . . .	69
4.2	Assembly underground . . . . .	71
4.2.1	Risks and Mitigations . . . . .	73
<b>5</b>	<b>Conclusion</b>	<b>74</b>
5.1	Summary . . . . .	74
5.1.1	Ion Source and LEBT Summary . . . . .	74
5.1.2	RFQ Summary . . . . .	75
5.1.3	Cyclotron Design Summary . . . . .	75
5.1.4	Installation Summary . . . . .	76
5.2	Outlook . . . . .	76
5.3	Acknowledgements . . . . .	76

# Chapter 1

## Introduction

IsoDAR will be the first high-intensity, proton-driven source to be located alongside an underground multi-kiloton-scale scintillator detector. The first version of IsoDAR will be constructed at the Yemilab facility [2] within the Handuk mine, located in South Korea where the “Liquid Scintillator Counter” (LSC)<sup>1</sup> is planned to be installed [3]. The novel source, consisting of a cyclotron, beam transport line, and a target/sleeve is shown in Fig. 1.1. In five calendar years (four live years), the source will produce 1.67 million  $\bar{\nu}_e + p \rightarrow e^+ + n$  (inverse beta decay or “IBD”) events and 7000  $\bar{\nu}_e + e^- \rightarrow \bar{\nu}_e + e^-$  (elastic scattering or ES) events in the LSC that can be used for searches for new physics. More than a mole of neutrons and mono-energetic photons are also produced in the target, and these may act as progenitors for new particles that enter the LSC and leave signatures from interactions and decays. IsoDAR can address a broad range of new physics manifested as new symmetries, new interactions and new particles that is inaccessible to traditional experiments. For further discussion see Refs. [4], [5].

<sup>1</sup>The LSC was renamed  $\nu$ Eye in March 2025, but for consistency throughout this document, we will refer to the detector as the LSC.

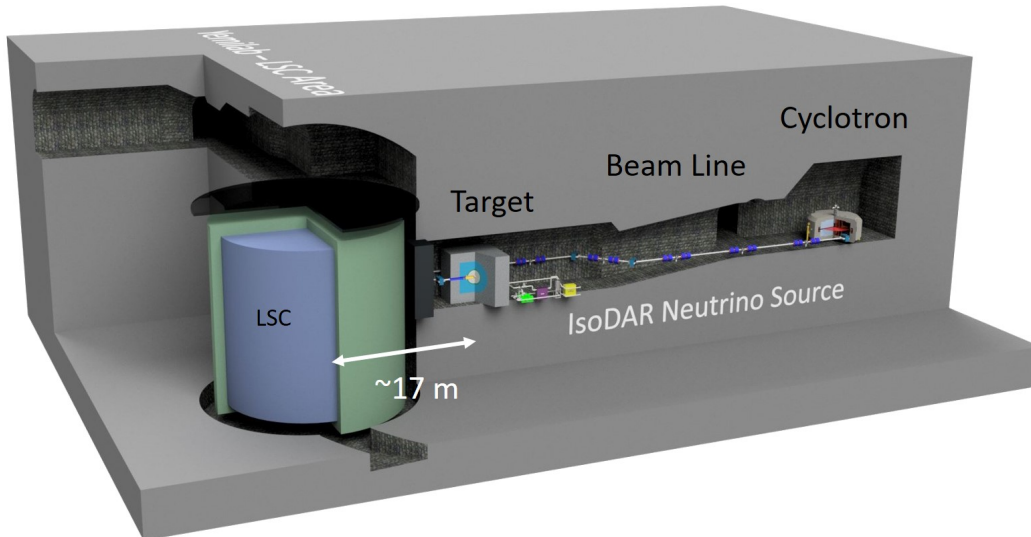


Figure 1.1: Schematic of the IsoDAR experiment installed at the Yemilab facility in South Korea. From right to left: The compact cyclotron with RFQ injector, the medium energy beam transport, the target, and the LSC neutrino detector. From Ref. [1].

This document is Volume I in a two-volume Preliminary Design Report (PDR) for IsoDAR that provides the engineering solutions necessary to establish credible solutions to the key issues and cost-drivers identified during the past decade of conceptual design and R&D. The contents of the PDR will cover the Technical Facility: the cyclotron, the beam transport and the target/sleeve. This document builds on the structure and text of the Conceptual Design Report (CDR) of the IsoDAR Technical Facility [6]. This step of producing a PDR substantially reduces risk related to IsoDAR approval: the remaining detailed engineering that will follow will build on these results and be straightforward to estimate in scope and cost.

Volume I describes the IsoDAR proton driver. This consists of a “front end” that delivers ions to a cyclotron for acceleration and extraction and the cyclotron itself. This document presupposes a basic understanding of cyclotrons; for an introduction to cyclotrons and a cost/benefit analysis of this choice of machine for IsoDAR, see the discussion in the CDR.

The 60 MeV/amu IsoDAR Proton Driver is exceptional in that it is designed and engineered to produce an order of magnitude higher current proton beams at extraction than commercial machines of similar energy. Achieving this high power necessitated three key breakthroughs. First, the cyclotron accelerates  $H_2^+$ , mitigating “space charge effects” (electromagnetic interactions between beam particles). Second, the beam is axially injected through an RFQ, acting as a high-efficiency buncher. Third, the design harnesses vortex motion, a complex effect previously observed at PSI Injector II [7], [8], inducing stable spiraling motion in the high-current accelerated beam, significantly reducing beam growth. For more concerning the accelerator physics that shapes the IsoDAR design, see Ref. [9], [10].

These three physics requirements for reaching high current drive many of the engineering choices presented in this PDR. The other design driver is the need to construct the cyclotron underground. The cavern for the IsoDAR Proton Driver has already been constructed at Yemilab, and so the dimensions and constraints are understood, leading to fully realistic engineering plans.

This PDR is structured as follows:

- **Chapter 1:** (This chapter) proceeds with an overview of the physics searches that will be possible with IsoDAR, followed by an overview of the requirements for the proton driver.
- **Chapter 2:** Describes engineering related to the IsoDAR front end.
- **Chapter 3:** Describes engineering related to the general IsoDAR cyclotron design.
- **Chapter 4:** Describes specifics of the design related to installation underground.

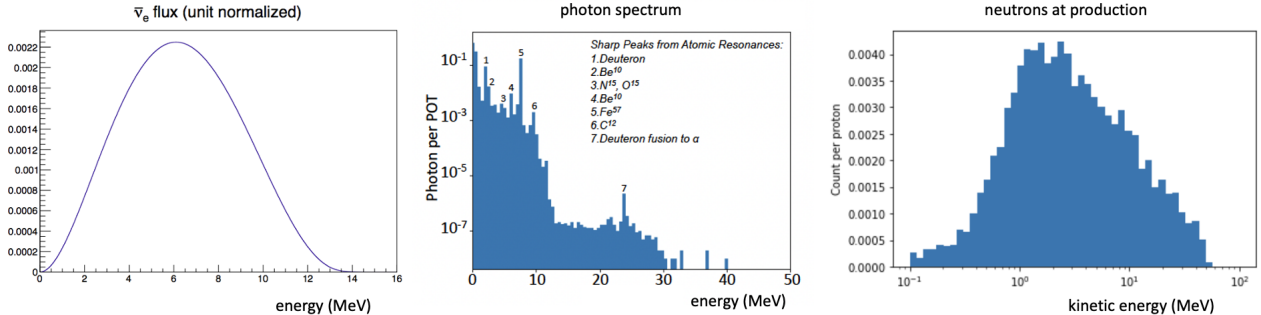


Figure 1.2: Energy dependence of fluxes. Left:  $\bar{\nu}_e$ , unit normalized; Middle: photons per proton on target (POT) from excited nuclei [4]. Right: kinetic energy of neutrons at production in target and sleeve, normalized per proton.

## 1.1 The IsoDAR Physics Case

IsoDAR offers a rich BSM physics program if paired with a kton-scale liquid scintillator detector like the proposed LSC at Yemilab [3]. The exceptional reach is owed to the high flux rates of  $\bar{\nu}_e$ , photons, and neutrons from the  $\approx 2 \cdot 10^{24}$  protons on target over 5 years (cf. Fig. 1.2), and placing the source very close to the detector. Here we briefly discuss the highlights of the IsoDAR BSM physics program enabled by a 2.26 kton detector like the LSC in three categories: “New Particles” - experimentally and theoretically motivated; “New Symmetries” - CP-violation and the QCD Axion; And “New Interactions” - Precision Electroweak Physics. See Refs. [4], [5], [11] for further details.

### 1.1.1 Fluxes in IsoDAR

We consider three fluxes of particles produced in the IsoDAR target for BSM physics searches: the  $\bar{\nu}_e$  flux, the neutron flux, and the  $\gamma$  flux from the excitation of nuclei as neutrons are moderated. These fluxes are shown in Fig. 1.2.

The  $\bar{\nu}_e$  flux stems from a single beta-decay of  ${}^8\text{Li}$ , which is produced by neutron capture on  ${}^7\text{Li}$  and is well-understood. It peaks at 6 MeV, which puts the majority of the events above backgrounds from the environment. These are clear advantages over reactor-neutrino fluxes. Interactions in the detector at these neutrino energies are exclusively inverse-beta-decay (IBD) and elastic scattering (ES). Cross sections for these reactions are known with uncertainties at  $< 1\%$  at these energies.

Neutrons in the IsoDAR target are primarily produced by spallation interactions of the beam protons with the beryllium target hemispheres. Additional secondary neutrons stem from interactions of the primary neutrons with beryllium in the target and sleeve. We model the processes in the target with Geant4 using an accurate representation of the latest target and sleeve design (see Refs. [12]). We show the resulting neutron energy spectrum in Fig 1.2 (right). Most neutrons capture on the  ${}^7\text{Li}$  in the sleeve. To ensure  $< 5$  neutrons per year enter the LSC veto region, the target is further shielded using boron-loaded concrete and steel [13].

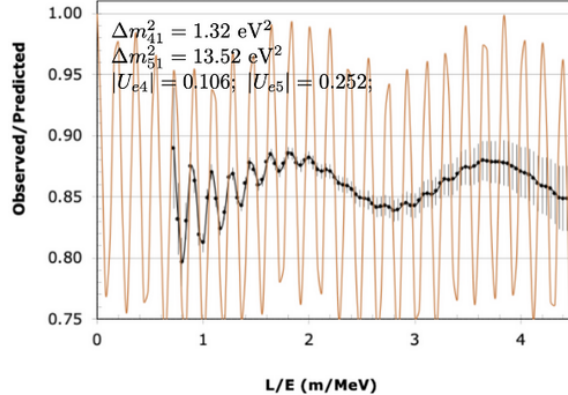


Figure 1.3: An example of a potential 3+2 signal in IsoDAR, orange—true signature, black—IsoDAR reconstruction with uncertainty shown.

The third flux we consider is that of photons as seen in Fig.1.2 (middle). Here, one can observe a line structure that stems from the transitions of excited nuclei and underlying smooth continuum due to bremsstrahlung. Again, the spectrum was generated using Geant4 using the full IsoDAR Target geometry [5].

### 1.1.2 New Particles: Experimentally and Theoretically Motivated

The original motivation for IsoDAR were the short baseline anomalies in neutrino oscillation experiments. IsoDAR provides a definitive search that is theory-agnostic and can observe signatures depending on  $L$  vs.  $E$ . The LSC records Inverse Beta Decay (IBD) events with  $\bar{\nu}_e$   $E$  resolution of  $< 6\%/\sqrt{E}$  and  $L$  determination to 40 cm (the  $1\sigma$  IsoDAR source size). Over 5 years of running, IsoDAR paired with the LSC will collect 1.67 million IBD events. The energy range (cf. Fig. 1.2 (left)) of the neutrinos is 3 to 13 MeV (the cut at 3 MeV is to reduce backgrounds). The baselines (due to the size of the detector) will be 9.5 m to 25.6 m. The capability to resolve several oscillation waves allows IsoDAR to examine models beyond the standard “3+1.” Examples are wavepacket decoherence [14], [15], 3+2 models (Fig.1.3), or 3+1+decay [16].

Another example of IsoDAR’s capability to look for new particles is the “ $X$ ,” which is a low mass mediator that would couple to the photons produced in the target [4]. The  $X$  would be a light new particle that decays to  $\bar{\nu}\nu$  and would leave a distinct signature above background in the IBD spectrum. Fig.1.4 (left) displays resulting signatures for various masses (see color bar) assuming 0.5%  $X$ -to-photon production. The IBD background from  $\bar{\nu}_e$  stemming from  ${}^8\text{Li}$  decays (gray) constitutes the primary background and has a distinct shape. The sensitivity is depicted in Fig.1.4 (right), where the blue region is excluded in the case of the SM. No existing limits are shown because this search is first-of-its-kind. A 17 MeV  $X$  particle is consistent with the Atomki anomaly.



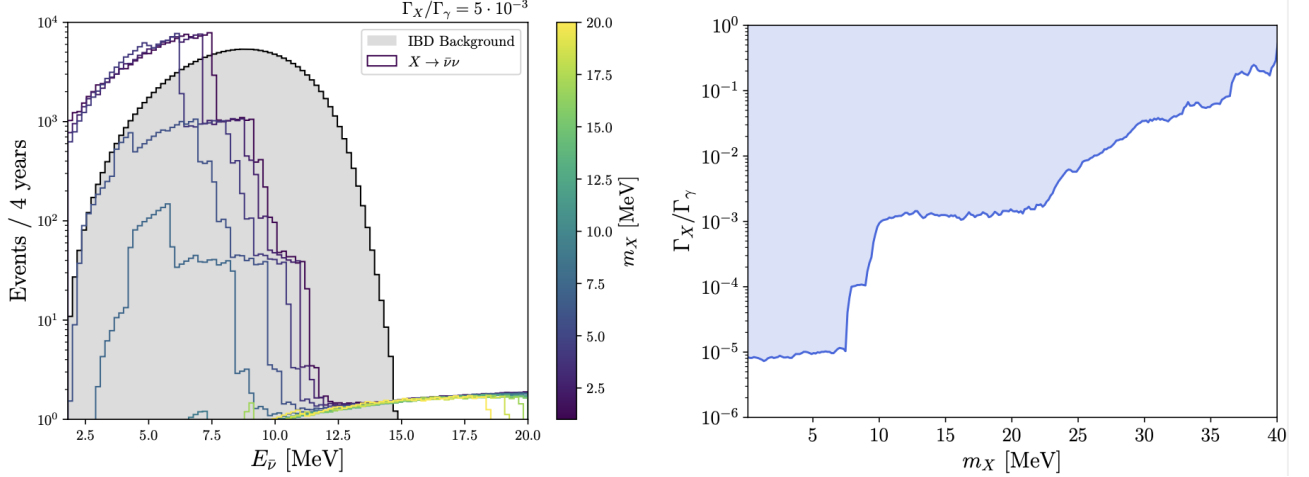


Figure 1.4: Left: Example  $X \rightarrow \nu\bar{\nu}$  signatures for 0.5% photon mixing with  ${}^8\text{Li}$ -produced  $\bar{\nu}_e$  background (gray). Right:  $X$  mass and  $X$ -to-photon production ratio 90% CL sensitivity. From Ref. [4].

### 1.1.3 New Symmetries: Strong CP Violation and the QCD Axion

The neutron beam/bottle experiment lifetime discrepancy [17]–[20] motivates neutron–dark sector couplings. Through  $n \rightarrow n' \rightarrow n$  transitions, we may see neutrons disappearing from the target and reappear in the LSC. The underground environment provides a low background and the LSC’s size further adds to the sensitivity [11]. Alternatively, if the  $n'$  are Majorana, then  $n \rightarrow n' \rightarrow \bar{n}$  may occur, depositing  $\sim 2$  GeV of energy in the LSC upon annihilation. This is a  $B$  violating effect with implications for the early universe [21].

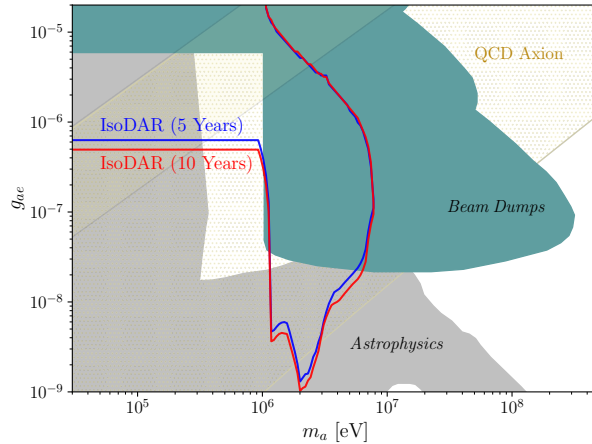


Figure 1.5: IsoDAR sensitivity for axions (a) with mass  $m_a$  coupling ( $g$ ) to electrons (lines) [5]. Gold dots–axion allowed; Teal–excluded regions; Gray–parameters with astrophysical implications.

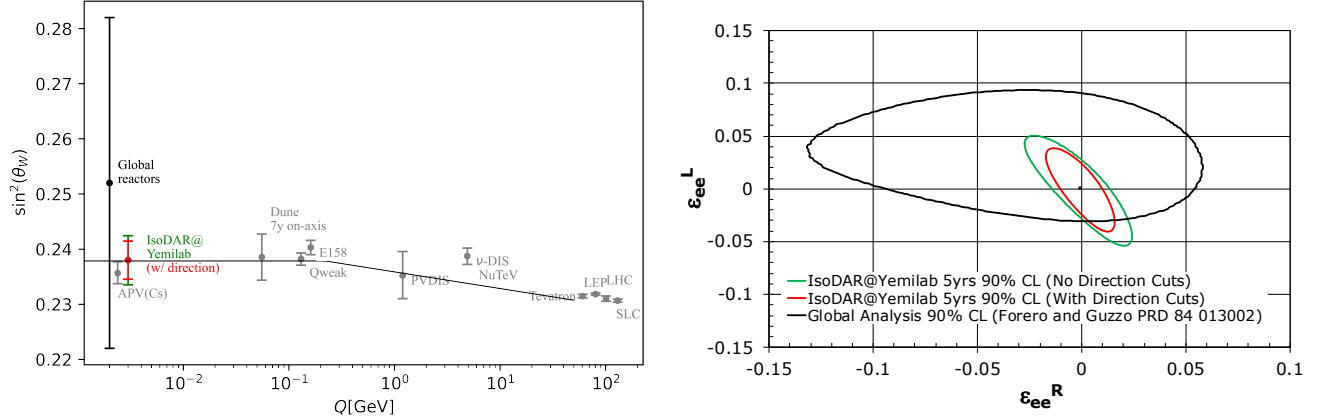


Figure 1.6: Left: Weak Mixing Angle expectation for IsoDAR compared to present results and the future DUNE expectation. Right: expectation for IsoDAR in NSI parameter space. From Ref. [4].

The photons and electrons in the target may also couple to axions and IsoDAR can probe uncharted territory with astrophysical and cosmological implications [5]. In Fig. 1.5 we show QCD axions coupling to electrons.

### 1.1.4 New Interactions: Tests via Precision Electroweak Physics

IsoDAR will record about 7000 elastic scatter events over its 4-year accumulated up-time. This constitutes the world’s largest sample at low momentum transfer. LEP and LHC data predict rate and energy dependency very precisely within the standard model [22]. With the normalization determined by the  $\approx 1.7\text{M}$  IBD events in the LSC, we will be able to measure  $\sin^2 \theta_W$  with a precision of 1.9% (see Fig.1.6 left).

As a neutrino-nucleon experiment, the observed deviation of NuTeV may stem from unaccounted-for nuclear physics effects; however, numerous possibilities have been investigated, but none fully explain the deviation. Alternatively, the deviation might signal new physics in the neutrino sector. If so, this BSM signature will also manifest in the IsoDAR ES measurement. Fig.1.6, right, presents two expectations for IsoDAR, where the red assumes background reduction from Cherenkov ring identification in LSC, while the green indicates the expectation without this additional information. Statistics limit the outcome, and further running can proceed with IsoDAR and DUNE as it comes online if a NuTeV-like deviation is observed.

The accurately predicted energy dependence of the ES sample enables a precise phenomenological search for non-standard neutrino interactions (NSIs). This powerful search for lepton-lepton couplings complements the lepton-quark coupling searches by the active, global coherent neutrino scattering program. The SM right- and left-handed couplings,  $g_R$  and  $g_L$ , are altered by NSI corrections for electron flavor antineutrino interactions with electrons (hence "ee") to  $\tilde{g}_R = g_R + \epsilon_{ee}^{eR}$  and  $\tilde{g}_L = g_L + \epsilon_{ee}^{eL}$ . The SM expectation for IsoDAR@Yemilab in the parameter space of these deviations is seen in Fig. 1.6 (right), where red assumes background reduction

using Cherenkov light, and green assumes only scintillation light reconstruction. This can be compared to the world result [23] in black, which is dominated by  $\nu_e$ -electron ES scattering from beam dump experiments and, hence, is rotated with respect to IsoDAR, which has a pure  $\bar{\nu}_e$  flux.

## 1.2 Requirements for the Proton Driver

As shown in Fig. 1.1, the Proton Driver consists of a 60 MeV/amu cyclotron accelerating and extracting 5 electrical milliamperes of  $H_2^+$ , a transport line that strips the  $H_2^+$  ions close to the extraction point, analyzes the stripped beam to monitor the health of the stripping foil, and transports the 10 milliamperes of protons to the target. The target consists of three nested hemispherical beryllium shells, the outermost being 20 cm in diameter, cooled with heavy water flowing around the shell structure. The proton beam is shaped, with quadrupoles and wobbler magnets to produce a distribution that allows for optimal heat transfer to the cooling water. Neutrons produced in the target system are moderated and flood into a roughly-spherical sleeve, about 1 meter in diameter, containing a mixture of beryllium chips and highly-enriched  $^7Li$ . The beta-decay of the  $^8Li$  resulting from the capture of neutrons produces the neutrinos of interest in the experiment.

The principal requirements for the accelerator system are to reliably produce a 10 mA beam of protons in the most efficient manner possible with the lowest possible loss of particles in the acceleration process. Particularly above the Coulomb threshold. The experience of the cyclotron system at PSI [24] is that keeping the total power of beam loss inside the cyclotron vault to less than 200 W still allows access for component maintenance. Considering that the total beam power is 600 kW, one sees that this is a very stringent requirement.

As mentioned above, Volume I of this PDR addresses the physics and engineering aspects of the 60 MeV/amu cyclotron. The final chapter addresses the complex issue of transport and assembly of large and heavy cyclotron components in the underground environment at Yemilab.

A forthcoming Volume II will address the details of the beam transport system and the target, along with shielding requirements for the environment of the target, including the prevention of fast neutrons from reaching the fiducial volume of the liquid scintillator detector.

## 1.3 Overview of the Accelerator Layout

To guide the reader through this PDR and, indeed, the path of an ion from genesis in the ion source to the full 60 MeV/amu and extraction, we provide an overview in Fig. 1.7. The main components of the system, which will be described in much detail in the following chapters, are:

- The ion source, providing 10 mA of  $H_2^+$  at an emittance  $< 0.1\pi$ -mm-mrad.
- The Low Energy Beam Transport (LEBT), shaping and guiding the beam to the RFQ and providing diagnostics, and chopping for commissioning and personnel- and machine

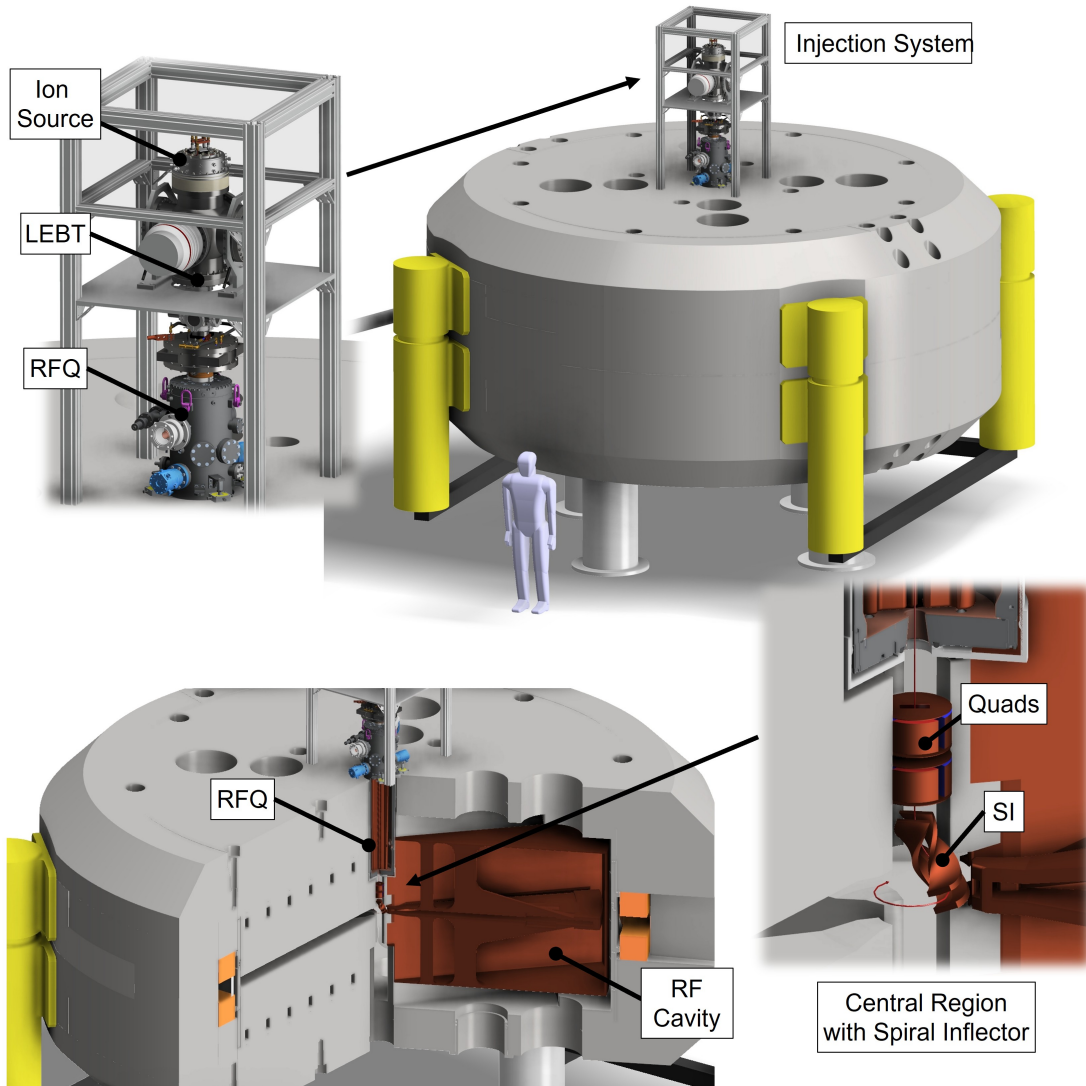


Figure 1.7: Overview of the components of the HCHC-60 Cyclotron System. Only one RF cavity is shown to not clutter the image.

protection.

- The Radiofrequency Quadrupole (RFQ), embedded in the cyclotron yoke, to bunch and pre-accelerate the beam to 35 keV/amu.
- The central region with electrostatic quadrupoles for transverse beam focusing, the spiral inflector to bring the beam from the vertical axis onto the median plane, and the specific RF electrode (aka “dees”) shapes to center the beam during the first turns.
- The main magnet and RF Cavities for acceleration to 60 MeV/amu.
- (not shown) The extraction system consisting of electrostatic and magnetic channels guiding the beam out of the cyclotron with the goal of extracting 5 mA of  $H_2^+$ .

# Chapter 2

## Design of the Front End

### 2.1 The Ion Source

The  $\text{H}_2^+$  beam to be injected into the cyclotron and accelerated to 60 MeV/amu will be produced by a filament-driven multicusp ion source. We have built a first prototype, the MIST-1 (Multicusp Ion Source at MIT - version 1), the technical details and first measured results of which are reported in Refs. [25]–[29]. Here we summarize these results and present ongoing upgrade work (MIST-2). The upgrade to MIST-2 improves on the MIST-1 by implementing several lessons learned during the systematic measurements and runtime experiences described below. A publication on the MIST-2 design and performance is forthcoming.

#### 2.1.1 Operating Principle

In a multicusp ion source [30], a plasma is confined by a set of permanent magnets that are arranged around the plasma chamber with alternating polarity, thereby creating “cusps” in the magnetic field. On average, the electrons and ions produced in the center of the chamber see an increasing magnetic field as they travel outward, which eventually turns them back. One notable exception are the cusps, which are the natural loss points of this configuration.

If the source is filament-driven<sup>1</sup>, electrons are emitted from a hot filament. A plasma discharge is initiated and sustained by applying a potential difference between the filament and (parts of) the source chamber. Thus, the filament acts as the cathode, and the source chamber acts as the anode of a discharge. Electron-impact ionization with neutral molecules and atoms in the source chamber produces secondary electrons and ions.

Neutral gas is fed into the source to facilitate the generation of a high-density plasma. The type of gas determines the ion species produced in the source. Here we use  $\text{H}_2$  gas to form a plasma – and beam – comprising protons,  $\text{H}_2^+$ , and  $\text{H}_3^+$ .

A significant concern, which we will quantify in Sec. 2.1.5, is the production of ions other than  $\text{H}_2^+$ . Of particular concern are  $\text{H}_3^+$ , which can be produced via  $\text{H}_2^+ + \text{H}_2 \rightarrow \text{H}_3^+ + \text{H}$ , as well as the production of free protons arising from premature dissociation of the  $\text{H}_2^+$ . To mitigate this the length of the plasma chamber is shorter than typical proton sources at 6.5 cm. This corresponds to the lower end of the range for the mean free path of  $\text{H}_2^+$  ions within a neutral  $\text{H}_2$  gas which

---

<sup>1</sup>Other options exist, e.g., RF-driven.

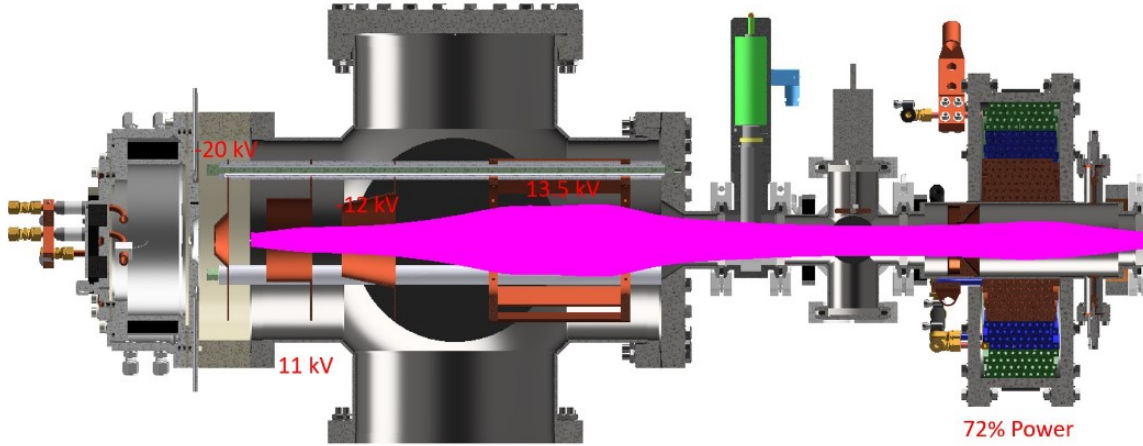


Figure 2.1: Cross section of MIST-1 (left) with extraction system and LEPT. Also shown is an example set of ion trajectories simulated with IBSimu and WARP. From Ref. [31].

we estimate to be between 5 - 20 cm depending on gas input flow rate. For more details on this computation, see Ref. [27].

Table 2.1: A summary of the parameters for the MIST-1 ion source.

Parameter	Nominal Value
Plasma chamber length	6.5 cm
Plasma chamber diameter	15 cm
Permanent magnet material	$\text{Sm}_2\text{Co}_{17}$
Permanent magnet strength	1.05 T on surface
Front plate magnets	12 bars (star shape)
Radial magnets	12 bars
Back plate magnets	Four bars in three rows
Front plate cooling	Embedded steel tube
Back plate cooling	Embedded copper pipe
Chamber cooling	Water jacket
Water flow (total)	$\approx 2$ L/min
Filament feedthrough cooling	Water cooled
Filament material	Water mixed with Cu and Ni
Filament diameter	$\approx 0.8$ mm
Discharge voltage	Max. 150 V
Discharge current	Max. 24 A
Filament heating	voltage Max. 8 V
Filament heating	current Max. 100 A

## 2.1.2 Mechanical Design

For visual reference as we discuss the details of the ion source, 3D CAD renderings of MIST-1 (with subsequent LEBT) and MIST-2 are provided in Figs. 2.1 and 2.2, respectively. The main ion source parameters are also summarized in Table 2.1.

The MIST-type ion sources comprise a plasma chamber surrounded by a “water-jacket,” a back plate, and a front plate. The water jacket lets us pump de-ionized (DI) water around the plasma chamber for cooling. The radial confinement magnets are mounted inside the water-jacket and are cooled directly. At 6.5 cm, the plasma chamber is short compared to other ion sources. This is a direct consequence of the short mean free path of  $H_2^+$  in the plasma/neutral gas of the ion source discussed above.

The nominal configuration for the confinement magnets is: Four rows of alternating magnets on the back plate, twelve alternating radial magnets, and a star formation of twelve smaller magnets on the front plate, also alternating in polarity. This leaves a small volume of low magnetic flux around the extraction aperture, allowing the ions to easily drift out of the source. All magnets are  $Sm_2Co_{17}$ . For MIST-2 we have begun studying different configurations (no magnets,  $Nd_2Fe_{14}B$  magnets). See below for more details.

The back plate holds four strips of confinement magnets, as well as the water-cooled filament feedthroughs, and the gas inlet (a KF NW-16 elbow). Temperature sensors (thermocouples) can be attached to the back plate to monitor the temperature of feedthroughs and magnets. The back plate itself is also water-cooled with cooling channels embedded in the plate. The filament is mounted to the high-current feedthroughs using molybdenum filament holders. The filament itself is made from tungsten and can have different thickness as well as shapes (this is a parameter currently being optimized).

The front plate holds the front confinement magnets as well as the plasma aperture, a 75%W-25%Cu (aka “Elkonite”) plate that is embedded in the front plate. We have several plasma apertures with different-size openings ranging from 4 mm to 8 mm to test beam quality and total extractable current for various aperture diameters.

As seen in Figs. 2.1 and 2.2, following the plasma aperture is the “extraction system” which shapes and guides the beam as it is initially formed. The MIST-1 extraction system comprises five electrodes which shape and accelerate the ion beam. These include a plasma electrode (+15 kV), a puller electrode (-3 to -20 kV), and three electrostatic lenses – Lens 1 (+10 kV to +15 kV), lens 2 (-3 kV to -15 kV), and lens 3 (+10 kV to +15 kV).

### 2.1.2.1 MIST-2 vs. MIST-1

The changes we made in the MIST-2 design are mainly to improve cooling, assembly and maintenance, and diagnostics. They are:

- Replace all stainless steel components with OFHC copper to improve heat transfer
- Increase the cross-section areas of all water cooling channels

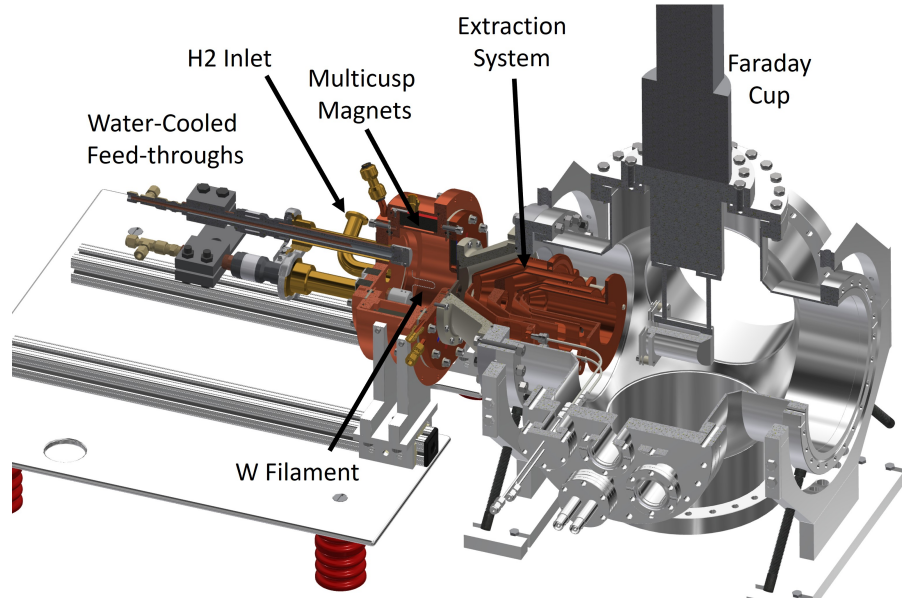


Figure 2.2: MIST-2 CAD rendering calling out the most important features.

- New high-power feedthroughs that are detachable from the back plate
- An additional port on the back plate for a Langmuir probe
- A redesigned extraction system. The new pentode extraction system comprises a water-cooled puller, an intermediate electrode, a negative electrode and a grounded final electrode. The more compact extraction system with negative potential followed by ground will help keep space charge compensation high in the LEBT and allows us to use a Faraday cup and emittance scanners for beam diagnostics directly after the source.

These changes will improve long-term running stability, reduce maintenance downtime, and allow for a better understanding of the plasma and beam conditions. Our high-fidelity simulations using IBSimu [32] and WARP [33] suggest that the beam dynamics downstream of the six-way cross will not change between the MIST-1 and MIST-2 configurations. All particle simulations and designs still hold for LEBT, RFQ, and Cyclotron.

### 2.1.3 Electrical Design

Hydrogen gas is introduced via an inlet in the backplate of the source as indicated in Fig. 2.2. The amount of hydrogen entering the ion source is controlled using a mass flow controller (MKS Instruments Model GV50A) which has a 5 SCCM full range. This system interfaces with the EPICS PC control system which is documented in detail in Ref. [29].

The filament is heated by an TDK Lambda (8.4 V, 300 A max) power supply. In addition to this power supply which is used to heat the filament, a second power supply (Matsusada REK) is connected to the filament and to the source chamber to maintain a potential difference of 80



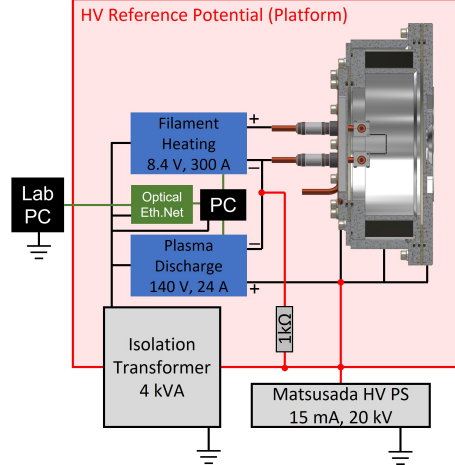


Figure 2.3: Wiring schematic for the ion source. The red square region corresponds to the HV reference potential. Green lines are data connections. Black lines are power cables.

- 140 V between them in order to facilitate electron discharge of up to 24 A max (typical during our tests was 5-10 A). The source body, back plate, and front plate are all mutually electrically insulated from each other for added flexibility in the electric field shape. Power is transferred to the platform via two isolation transformers of 2 kVA each. A schematic of the wiring of the ion source is illustrated in Fig. 2.3.

The ion source (platform) is lifted to high voltage using a Matsusada AU 15 mA, 20 kV power supply, all lens elements in the extraction system are powered by Matsusada AU 7.5 mA, 20 kV power supplies of either negative or positive polarity.

The devices on the HV platform (control computer, filament discharge, filament heating power supply, etc.) are inside a Faraday cage on platform potential to reduce electromagnetic interference (EMF). Surrounding the platform and ion source is another Faraday cage at ground potential for personnel protection and EMF reduction.

### 2.1.4 Beam Dynamics

We simulate beam formation and shaping in the extraction system with the IBSimu package [32], which performs cylindrically symmetric 2D (aka “RZ”) and 3D simulations including space charge through an iterative process. IBSimu also contains a 1D plasma sheath model which is a good approximation for the plasma-beam interface at the source aperture. Our extraction simulations of the MIST-1 ion source followed by a WARP [33] simulation of the LEBT yielded excellent agreement with measurements [26], [28]. Example trajectories of the new MIST-1 extraction system and RFQ matching LEBT are shown in Fig. 2.1.

An extraction system simulation of the MIST-2 system is shown in Fig. 2.4. The simulated normalized RMS emittance for the new MIST-2 extraction system using an 8 mm diameter plasma aperture is  $0.077 \pi$ -mm-mrad. Simulated normalized RMS emittances for the MIST-1 extraction system were between 0.05 and 0.1  $\pi$ -mm-mrad depending on source aperture and

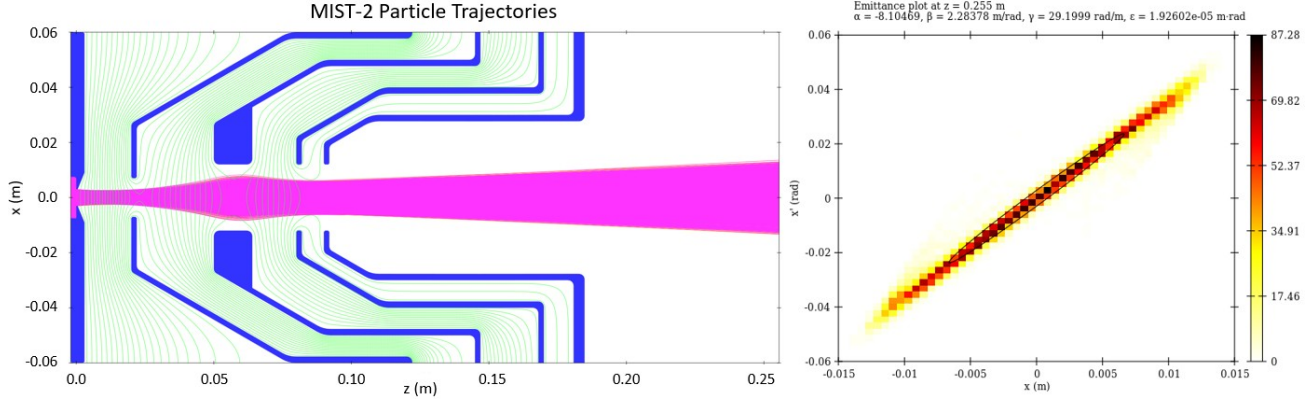


Figure 2.4: IBSimu Simulation of MIST-2 extraction. Left: trajectories, Right: x-x' phase space. Both MIST-1 and MIST-2 exhibit a very low emittance (see text).

extracted current and agreed well with measurements [26].

## 2.1.5 Performance

### 2.1.5.1 Goals & Measurement Methods

In this section we summarize the latest measured results as well as discussing the results of several optimizations that have been thus far performed as well as several that remain to be performed. The ion source target parameters that will be required for IsoDAR to achieve the planned decisive results for a sterile neutrino search include the following benchmarks:

- High current:  $\approx 10$  mA of  $H_2^+$
- High purity:  $H_2^+$  fraction  $> 80\%$
- Low emittance:  $< 0.1$   $\pi$ -mm-mrad (RMS, normalized)
- Ability to run continuously in DC mode

Characterization of the ion source is done using a short diagnostic beam line. This test beam line comprises two Faraday cups, a dipole magnet with separation slits, and a pair of Allison emittance scanners. The total beam current is measured using the first Faraday cup located posterior to the extraction system. The dipole magnet separates the ions by mass and passes them to the second Faraday cup for mass analysis. Allison-type electrostatic emittance scanners measure each species' horizontal and vertical emittances.

### 2.1.5.2 Optimization of Ion Source Parameters

The ion source is designed such that several parameters can be varied in order to optimize the magnitude, purity, and emittance tightness of the current from the ion source.

- H<sub>2</sub> input flow rate
- Filament discharge voltage
- Filament discharge current
- Filament size, shape, & position (*Optimization not yet fully studied*)
- Permanent magnet type

**H<sub>2</sub> input flow optimization.** Three series of optimizations on the input gas flow rate have been performed. The three series differ in how the filament discharge voltage is managed. In the first series, the PID loop which stabilizes discharge was disabled allowing the discharge current to rise to the source steady-state value and then stabilized at that value by reengaging the PID. In the second series, the discharge current was kept fixed at 4 A. In the third series, the discharge current was reduced to keep the total extracted current fixed at 1.25 mA. Under each of these three conditions, the gas input rate was varied from 0.25 - 1.25 SCCM. This study demonstrates a general trend of greater H<sub>2</sub><sup>+</sup> production at higher discharge currents and, as theoretically expected, a higher fraction of H<sub>3</sub><sup>+</sup> with higher flow rates.

**Discharge voltage optimization.** Two series of discharge voltage optimizations have been performed differing in how discharge current is managed. In the first, discharge current is permitted to freely find a steady state using the same method as used in the flow optimization described above. In the second, the discharge current was fixed at 4 A.

**Discharge current optimization.** One series of current optimizations was explored in which the flow rate and discharge were kept constant while discharge current was varied from 2 to 8 A. No strong dependence on current was observed.

### 2.1.5.3 Latest Optimized Results

To date, only an incomplete optimization of the ion source has been performed. As such, parameters which simultaneously meet all the target goals have not yet been fully identified. The ion source's peak performance to date varies, therefore, depending on which of the performance metrics is optimized. Optimization has been performed for maximum total current density, maximum H<sub>2</sub><sup>+</sup> purity, and a hybrid option optimizing for the maximum H<sub>2</sub><sup>+</sup> current density with the constraint that H<sub>2</sub><sup>+</sup> be dominant.

**Highest total current density:** 41 mA/cm<sup>2</sup> with 31% H<sub>2</sub><sup>+</sup> purity.

**Highest H<sub>2</sub><sup>+</sup> purity:** 76% purity with 11.4 mA/cm<sup>2</sup> total current density.

**Highest H<sub>2</sub><sup>+</sup> current density with H<sub>2</sub><sup>+</sup> dominant:** 10.4 mA/cm<sup>2</sup> with 62% purity<sup>2</sup>.

With current optimizations and a 4mm aperture, the ion source is capable of delivering approximately 1.1 mA of H<sub>2</sub><sup>+</sup> with 76% purity. With an 8 mm aperture this corresponds to 4.4 mA. This is a world-leading result and is only about a factor of 2 short of the target.

---

<sup>2</sup>Note that this is the current density of H<sub>2</sub><sup>+</sup> alone.

The main bottleneck for an increased beam current was the extraction system, which was designed for initial testing and commissioning. We have recently replaced it with the version presented in this chapter. Our high-fidelity simulations suggest that the new extraction system will be able to handle the nominal beam current. Measurements are planned for summer 2024.

#### 2.1.5.4 Magnet Study

The choice of permanent magnet material and strength is one of the optimization parameters of this type of ion source. Here, plasma density, confinement time, and magnet thermal properties are important parameters to consider. Originally, we selected  $\text{Sm}_2\text{Co}_{17}$  magnets for their higher Curie temperature. However, long-term running tests suggest that the magnet temperature is well controlled, which would allow the use of  $\text{Nd}_2\text{Fe}_{14}\text{B}$  magnets, if they yielded a better beam.

We aim to maximize the  $\text{H}_2^+$  fraction of the MIST-1 ion source. Within the plasma, atomic processes include ionization, dissociation, and recombination, leading to protons,  $\text{H}_2^+$ , and  $\text{H}_3^+$  in the beam. Magnets with a higher field strength yield higher plasma density and longer confinement of the ions in the plasma, which can alter the rates of these processes. Thus, we are interested in how different magnet types alter the ion fraction and total current. We investigated the current and ion fraction of the beam with no magnets,  $\text{Sm}_2\text{Co}_{17}$  magnets (grade 28), and  $\text{Nd}_2\text{Fe}_{14}\text{B}$  (grade N50H). The configuration without magnets provides no confinement, and the  $\text{Nd}_2\text{Fe}_{14}\text{B}$  magnets provide the strongest confinement. We performed our measurements using the diagnostic beam line presented in Ref. [26], containing a dipole magnet and a Faraday cup with 8 mm entrance slit for mass analysis. We investigated each magnet type at a range of  $\text{H}_2$  mass flows (0.25 SCCM to 1.5 SCCM) and discharge voltages (60 V to 140 V).

In our preliminary analysis, we observed a trade-off between the total beam current and the  $\text{H}_2^+$  fraction: with lower confinement, the  $\text{H}_2^+$  fraction was high, but the current was low. This result was expected; lower confinement and lower plasma density leads to less time and fewer reactants for the ions to undergo processes that result in  $\text{H}_2^+$  dissociation or the pick-up of another proton (producing  $\text{H}_3^+$ ). However, the lower plasma density also leads to a lower total beam current.

For MIST-2, the baseline design is now to use  $\text{Nd}_2\text{Fe}_{14}\text{B}$  magnets because of the higher current they provide. A paper on the detailed analysis of the magnet study is forthcoming.

#### 2.1.5.5 Results with the MIST-2 back plate

We already performed the first test of the MIST-2 components described in Section 2.1.2.1 by installing the new back plate (which is backward compatible) on MIST-1. We were able to run the source up to a stable beam current of 3.43 mA. We did this with the source set to 7.5 kV (the nominal source voltage of 15 kV requires a full beam current of 10 mA to form the appropriate plasma meniscus), puller set to -5 kV, lens 1 at 1.5 kV, lens 2 at -3 kV, lens 3 at 0.5 kV and the filament heating set to 150 A.

Due to the improved cooling and filament feedthroughs and holders, the source ran very stably; as we expected. A sample spectrum from this series of studies is shown in Fig. 2.5. Here, a

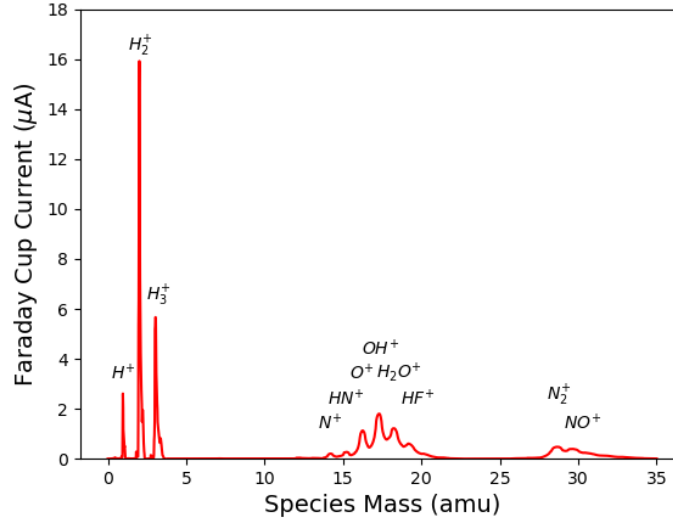


Figure 2.5: A typical spectrum with the new MIST-2 back plate. The total beam current was 3.43 mA, the  $H_2^+$  fraction  $\approx 60\%$ . For a discussion about the small contaminant peak, cf. text.

small cluster of beam contaminants can still be seen, which we attribute to insufficient baking and out-gassing of source components, including Viton O-rings. Past experience has shown that vacuum baking the O-rings before installation (done here), overall good vacuum conditions, and baking the source and beam line before operation (not done in this instance), decreases the contaminants to a negligible level after a few hours of operation [26].

## 2.1.6 Risks and Mitigation

**Risk: Ion Source Long-Time Stability.** As IsoDAR is designed to run continuously for 5 years, the long-time stability is a major concern for the ion source. Hands-on maintenance of the ion source is going to be limited, because of the close proximity of the cyclotron.

**Mitigation:** *Before the final technical design, we will develop alternative heating methods (external antenna and 2.45 GHz microwaves). MIST-1 and MIST-2 were being designed with an exchangeable backplate for quick filament replacement and easy further development of alternative heating methods. Another option is a dual-source operation using a switching magnet.*

**Risk: Ion source maximum  $H_2^+$  current is too low.** The current densities seen from the MIST-1 ion source are still a factor 2 below the requirements for IsoDAR.

**Mitigation:** *Our current upgrade path should lead us comfortably to a total extracted current of 12 mA, particularly considering that MIST-1 has demonstrated an exceptionally low emittance, which opens up the possibility of going to even larger extraction apertures (10 mm or 12 mm). However, we also have tested a 2.45 GHz flat-field ECR ion source (the VIS [34]) in the past, from which we measured 15 mA of  $H_2^+$ . The low ratio of 50%  $H_2^+$  (30 mA total current) deterred us, but as a mitigation, a VIS-type ion source paired with a dipole magnet is a viable alternative.*

## 2.2 The Low Energy Beam Transport

The low energy beam transport line (LEBT) serves the purpose of connecting the ion source to the RFQ. The LEBT steers and shapes the beam, guiding it into the RFQ. The LEBT also provides a location at which to take beam diagnostics. The requirements for the LEBT are:

1. Transport beam with minimal losses,
2. Provide space for diagnostics,
3. Match the beam to the RFQ,
4. Provide safety mechanisms for personnel and machine protection.

Details of the LEBT design and performance were given in Refs. [31], [35], [36] here we summarize and update these.

### 2.2.1 Design Overview

At this stage, ions emerge from the ion source. The beam now passes through a gap surrounded by a series of six electrodes arranged axially within a six-way cross (see Fig. 2.1). These six electrodes can have their voltage optimized in order to best match the parameters for acceptance into the rest of the LEBT. A conical flange is connected to the end of the six-way cross. The conical shape minimizes beam loss on exit.

Following the six-way cross lies a diagnostic segment. A gate valve separates the six-way cross from this segment. The diagnostic section comprises a second cross, which can be used for additional vacuum attachments, diagnostic readouts, and a chopping electrode. The diagnostic

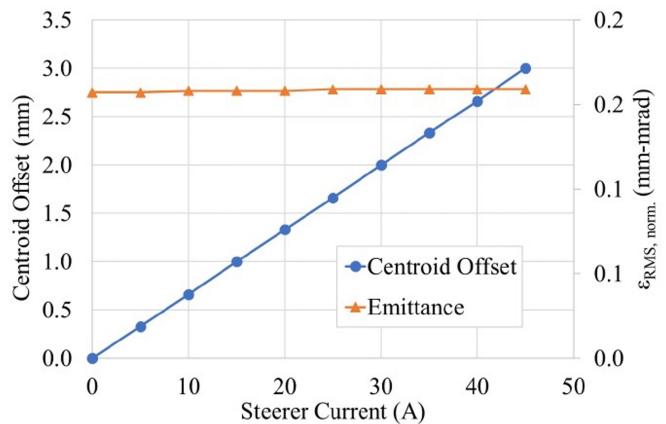


Figure 2.6: Left: Photo of Alpha Magnetics, Inc. steerers [37]. Right: Result of LEBT steering simulations. It can be seen that several millimeters offset can be achieved without significant change in emittance. From Ref. [31].

section also includes a solenoid and two magnetic steerers which can be used for additional beam tuning. A flange in place toward the end allows space for an AC Current Transformer (ACCT) [38] which characterizes the beam immediately prior to entering the RFQ. The diagnostic segment is illustrated in Fig. 2.1.

### 2.2.2 Beam Steering & Chopping

The diagnostic segment also serves to steer the beam into the RFQ or terminate the beam as needed. Even small, sub-millimeter misalignment can prevent efficient injection of the beam into the RFQ. In order to ensure that the beam enters the RFQ at both the correct position and angle, two magnetic steerers and a solenoid magnet are placed around the beamline. These are controlled independently by an external power source to produce tunable dipole fields which optimize beam entry into the RFQ. The optimal fields were calculated using COMSOL and beam dynamics simulated in WARP. The effect of the steerers is demonstrated in Fig. 2.6.

In order to control the amount of power delivered from the ion source, a beam chopper is built into the cross of the diagnostic segment to allow for a duty factor in an otherwise DC beam. The beam chopper is built into the cross in the diagnostic section. The chopper comprises a deflection plate, followed by a copper ring for particle dumping press-fitted into a steel beam pipe which in turn is surrounded by a copper water cooling jacket. The deflection plate can be put at a high potential relative to the cross, which is grounded, diverting the beam such that it terminates on the copper ring. See Fig. 2.7. This method permits controlling the average beam power, without changing the charge per bunch resulting from the RFQ. This is required to maintain vortex motion in the cyclotron.

A 12 mA beam of 15 keV particles fully terminating on the beam stop corresponds to  $\sim 180$  W power delivered. We need to ensure that the dump is capable of dissipating this amount of power. The system was modeled by assuming a water cooling line at room temperature. To be conservative, the simulation was run using four times the actual anticipated beam power, i.e. 720 W. The beam dump never rose above 360 K in our simulation, significantly below the melting point of copper. The COMSOL simulation is shown in Fig. 2.8

### 2.2.3 Beam Dynamics

Beam simulations are performed in order to characterize the performance of the LEBT with the ultimate goal of ensuring that beam's Twiss parameters matches the desired input parameters for the RFQ.

Beam simulations for the LEBT have been performed using IBSimu and Warp. IBSimu provides a more accurate plasma model, but is computationally intensive and so was used only for the region by the ion source where the plasma is extracted and the density is thus high, requiring this accuracy. IBSimu is used for the first several millimeters after the extraction aperture, where density remains high. After this, and for the remainder of the downstream region of the LEBT, the distributions from IBSimu are handed off to Warp which provides accurate results

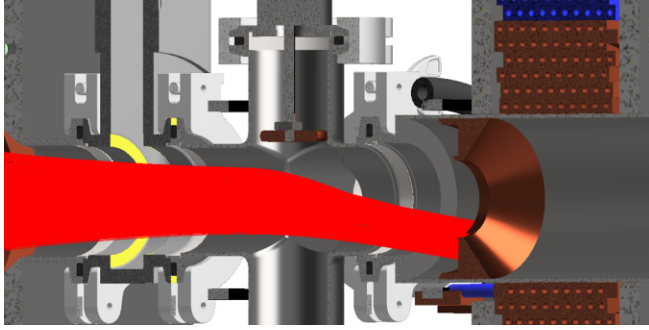


Figure 2.7: CAD model of the LEBT diagnostic segment with beam simulation (red) overlaid. If the copper electrode (top) is held at adequate potential the beam is pushed off its center course and terminates on the copper ring. From Ref. [31].

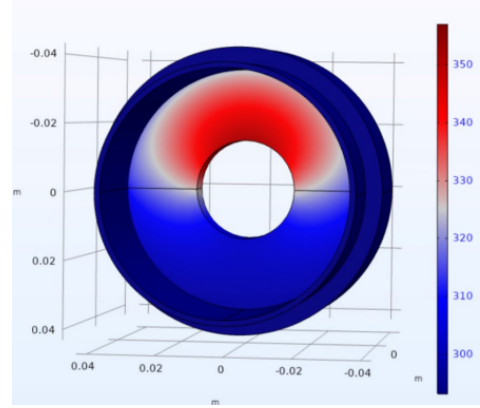


Figure 2.8: COMSOL simulation of the beam terminating on the copper aperture surrounded by the steel beampipe, with copper water cooling channel on the exterior. From Ref. [31].

for the lower density regions of the beam with less computational burden.

Space charge is included in all calculations. However, as is well-known, in the absence of external electrical fields, slow secondary charged particles from the interaction of the beam with the residual gas can be accumulated inside the beam envelope, effectively neutralizing the beam charge. This process is called “space charge compensation” [39]. In all LEBT simulations, we estimate space charge compensation according to the model presented in Ref. [39]. It is usually above 80%, alleviating the detrimental effect of space charge in some parts of the LEBT. However, we also test our designs with no compensation and find that, while beam losses are slightly higher, we can still obtain the required beam inside the cyclotron, albeit requiring about 20% higher beam from the source.

For the IBSimu simulations a 12 mA beam composed of 80%  $H_2^+$ , 10%  $H^+$ , and 10%  $H_3^+$  was used. This provides ample current for IsoDAR assuming 50% global transmission efficiency while using current from the ion source that has already been empirically demonstrated. As illustrated in Fig. 2.9 and in Table 2.2 the LEBT can match the required input parameters for the RFQ. Moreover, as illustrated in Fig. 2.10 this match is achieved with emittance that surpasses that used for baseline RFQ simulations.

Table 2.2: A comparison of LEBT Twiss parameters and baseline RFQ parameters.

Parameter	LEBT Output	Baseline
Norm. RMS Emitt.	$0.175\pi$ mm-mrad	$0.3\pi$ mm-mrad
$\alpha$	1.3	1.0
$\beta$	0.13 mm/mrad	0.17 mm/mrad



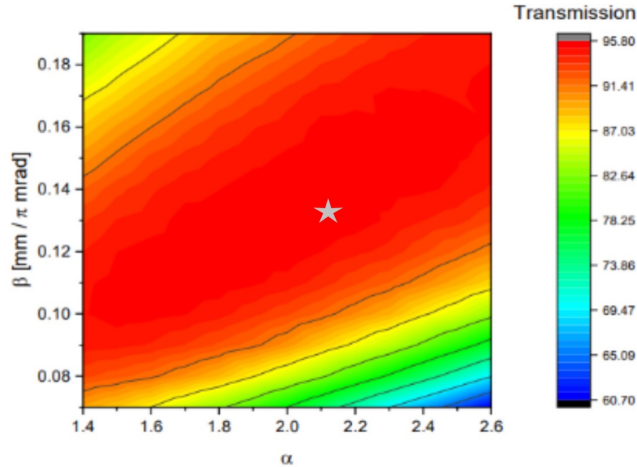


Figure 2.9: A temperature plot showing the Twiss parameters required for optimal transmission through the RFQ. The indicated point shows the parameters at the end of the LEBT. [31]

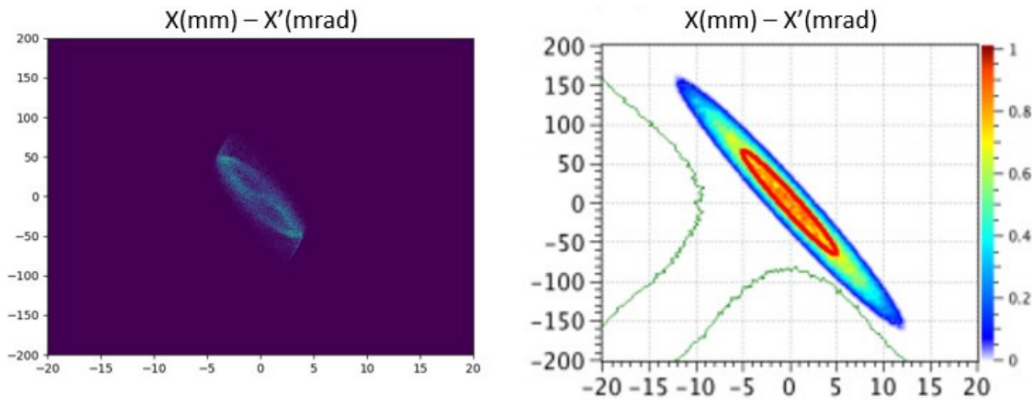


Figure 2.10: Phase space from the LEBT simulation (left) vs phase space for ideal beam input to the RFQ (right). From Ref. [31].

## 2.2.4 Risks and Mitigations

**Risk: Unexpected Power Loss.** In the case of an unexpected loss of power to one of the power supplies, the beam dynamics could be very different from nominal and lead to damage downstream (e.g., the RFQ).

**Mitigation:** Careful simulation of various failure modes showed that the LEBT is robust under such changes. The time constant involved with heating up of materials are such that the beam can be switched off before damage occurs. However, for the MIST-2 design, we are envisioning the addition of a Faraday cup directly downstream of the extraction system. Operating spring-loaded, it can be inserted quickly to intercept the beam early on.

**Risk: Lower than anticipated space charge compensation.** Optimal beam transport was calculated for a high compensation factor. If this is not the case, transport efficiency and beam dynamics may deteriorate.

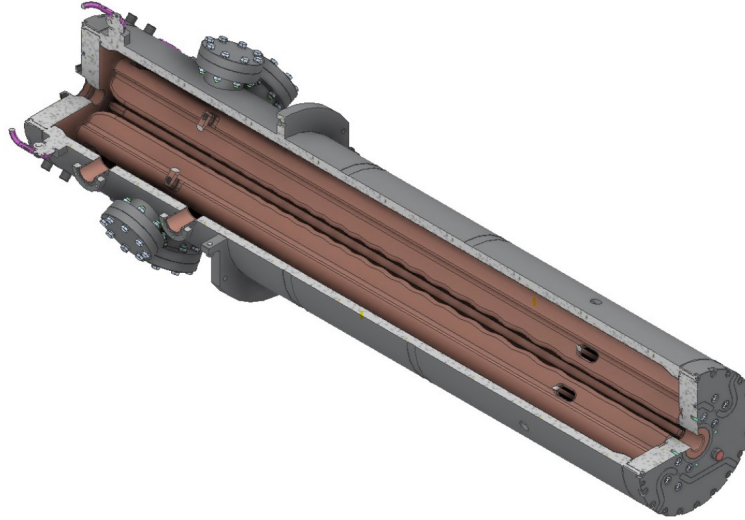


Figure 2.11: Cut view of the IsoDAR RFQ. In the split-coaxial design, vanes are attached to the front and end plates rather than radially to the mantle. From Ref. [31].

**Mitigation:** *The LEBT design was double-checked with no space charge compensation and care was taken that injection into the RFQ is nevertheless possible. Typically, higher losses, which are still manageable, are seen. The ion source must provide about 20% more beam current in this case.*

## 2.3 The Radiofrequency Quadrupole

The  $\text{H}_2^+$  beam coming from the LEBT is injected into a Radio Frequency Quadrupole (RFQ) that is partially embedded in the cyclotron yoke. A schematic of the RFQ and cyclotron can be seen in Fig. 3.1 where only about a third of the RFQ is visible above the top surface of the cyclotron. We show a cut view of the RFQ in Fig. 2.11. Of note are the small diameter of the RFQ (27.6 cm) while operating at a low resonant frequency of 32.8 MHz. This is achieved by utilizing the so-called “split-coaxial” mode where the vanes are attached longitudinally at the entrance and exit flanges instead of radially at the mantle. The main operating parameters of the RFQ are listed in Tab. 2.3. The RFQ accelerates only moderately from 7.5 keV/amu to 35 keV/amu and acts mainly as a very efficient buncher. This leads to a conservatively estimated power consumption of  $< 6$  kW.

### 2.3.1 Technical Design

The technical design was presented in Refs. [40]–[42] and the optimization of the RF loop coupler in Ref. [43]. The thermal properties and cooling considerations were presented in Ref. [44]. An optimization scheme using machine learning was presented in Ref. [45].



Figure 2.12: Modes of the mechanical deformation of the RFQ vanes. The frequencies are 18 Hz and 25 Hz. From Ref. [42].

In terms of mechanical stability, our analyses show two quarter wave modes which are associated with the choice of a split-coaxial resonator. The addition of bridges between opposite vanes (see Fig. 2.12) significantly reduces detuning due to the Lorentz force with mechanical frequencies around 18 Hz and 25 Hz.

### 2.3.2 Beam Dynamics

Beam dynamics studies were performed of the full 3D particle distribution resulting from the LEBT simulations going through the RFQ, including the effects of the entrance gap and asymmetry (due to the split coaxial design) and the exit gap and asymmetry. This was performed by the subcontracted company Bevatech GmbH in Germany, who is currently also manufacturing the RFQ. The well-established tracking code TraceWin was used [46]. Fine tuning of the phase of the exit gap (i.e. tuning the length of a drift preceding the exit gap), leads to final output beam parameters listed in Tab. 2.4.

Table 2.3: A summary of the design parameters for the RFQ.

Parameter	Nominal Value
Diameter	27.6 cm
Frequency	32.8 MHz
Tuning range	$\pm 270$ kHz
Q simulated	2800
Shunt impedance $R_p$	4.9 k $\Omega$ /m
Input Energy	7.5 keV/amu
Output Energy	35 keV/amu
Duty factor	100% (cw)
Power	< 6 kW
Cooling	DI Water channels in tank and vanes

Table 2.4: RFQ output beam parameters.

Parameter	Nominal Value
$\varepsilon_x$ (1-RMS, norm.)	0.54 mm-mrad
$\varepsilon_y$ (1-RMS, norm.)	0.52 mm-mrad
$\varepsilon_z$ (1-RMS, norm.)	0.114 MeV-deg
Phase width (1-RMS)	40°

### 2.3.3 Risks and Mitigation

**Risk: New RFQ Technology.** Direct axial injection into a compact cyclotron has never been demonstrated. It is possible that there are limitations that have not been thought of, that will prove to be show-stoppers.

***Mitigation:** A prototype machine is currently being built and will be thoroughly tested in the coming year. As a fallback, conventional LEBTs using a multi-harmonic buncher are well understood and reliable. However, they are much less efficient than RFQs. The focus in this case will shift to increasing ion source performance further to allow for higher beam losses during injection.*

**Risk: RFQ Power Estimate** The RFQ costs depend strongly on the RF power necessary to drive the rods/vanes, the length of the RFQ, the engineering complexity involved in machining the vanes/rods and designing the vacuum vessel.

***Mitigation:** We have worked with RF engineers with intimate knowledge of RFQ design. The upcoming prototype will demonstrate the power requirements.*

**Risk: Beam spread between RFQ exit and spiral inflector.** The simulations showed that the beam spreads transversally and longitudinally after exiting the RFQ. Reality might prove more unforgiving than computer simulations and we may incur higher beam losses than anticipated.

***Mitigation:** Our high-fidelity simulations suggest that the beam spread is manageable. The prototype will allow measuring this precisely. Additional focusing elements can be inserted between RFQ and spiral inflector if necessary. More aggressive collimation is possible as well, at the expense of requiring higher current from the source.*

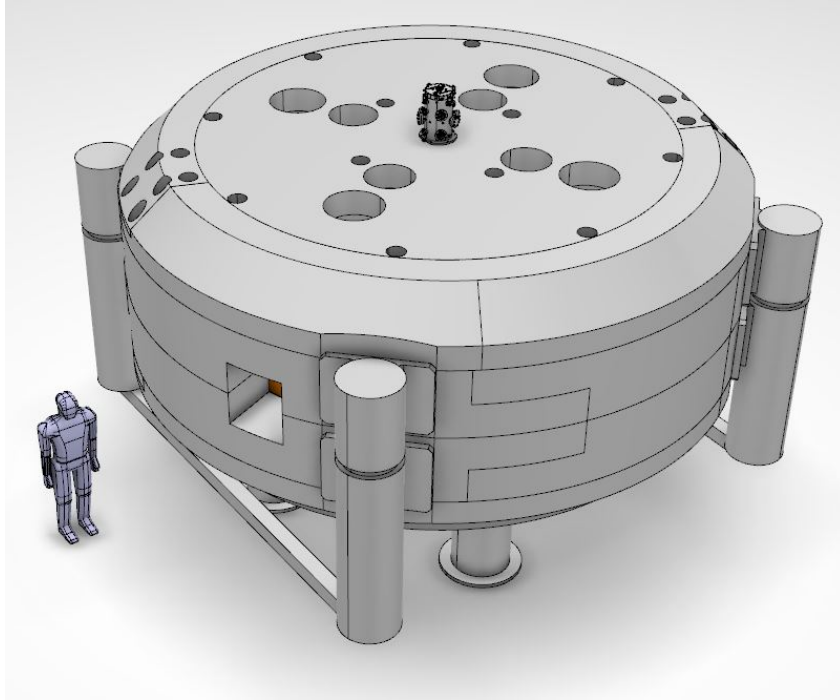


Figure 3.1: Isometric view of the cyclotron.

## Chapter 3

# Design of the Cyclotron

In this section, we describe the details of the cyclotron at the level of a preliminary design report. This section includes details of the design of the cyclotron, the spiral inflector that transmits ions from the RFQ into the cyclotron, and the extraction system.

This section also characterizes the latest in simulo performance of these systems.

### 3.1 Magnet Yoke

The magnet design presented here is physically realistic, but is necessarily preliminary. We do not anticipate the broad design of the magnet to change in future. As we finalize the details of beam extraction small modifications to the magnets, especially at the fringes, may accordingly be modified.



Figure 3.2: C400 on the milling machine, C230 in front of it. Courtesy of IBA.

The engineering design of the IsoDAR magnet benefits from the experience gained by IBA in the fabrication of its C400 cyclotron (seen in Fig 3.2), which is slightly larger, at 7 meters outer diameter.

### 3.1.1 Design and Fabrication of the Cyclotron Magnet

As with the C400, the IsoDAR cyclotron is divided into smaller parts to facilitate transport to the site. The magnet is split radially and will be assembled on site. The vacuum chamber is split into 3 self-centering parts along its height. The vacuum tightness is ensured by 2 axial O-rings at each interface except for the interface between the upper and lower chambers where 2 radial O-rings are used. An exploded visualization of the upper and lower parts is shown in Figs. 3.3 and 3.4. The material used for the magnet parts is cyclotron steel (the exact composition shall be determined after a detailed physics study), the vacuum chambers will be made of stainless steel.

An cut-section view of the cyclotron is shown in Fig. 3.5. The external and vacuum disks are connected to each other as well as to the flux return using specific bolts (such as the Superbolt from Nord-Lock). The poles are split into several parts and an easily removable part should be added in the next iteration to ease the mapping and possibly improve the magnetic performance. A detailed view of the cyclotron components is shown in Fig. 3.6 and additional details about the yoke parts can be found in Table 3.1

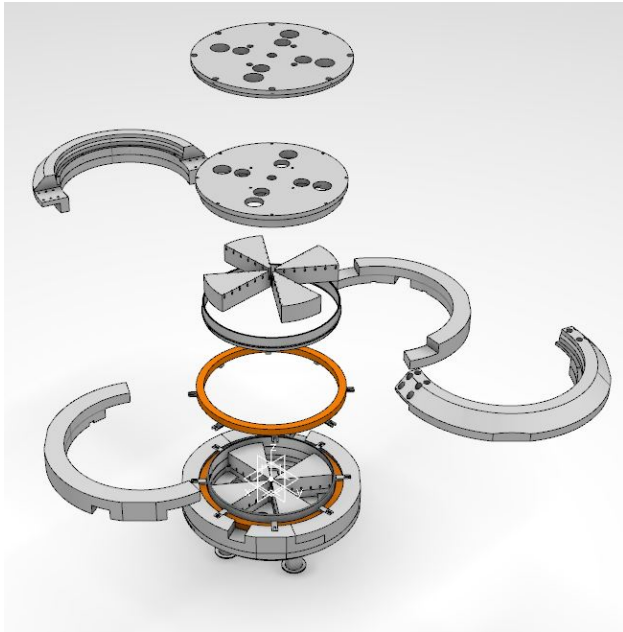


Figure 3.3: Cyclotron upper steel exploded.

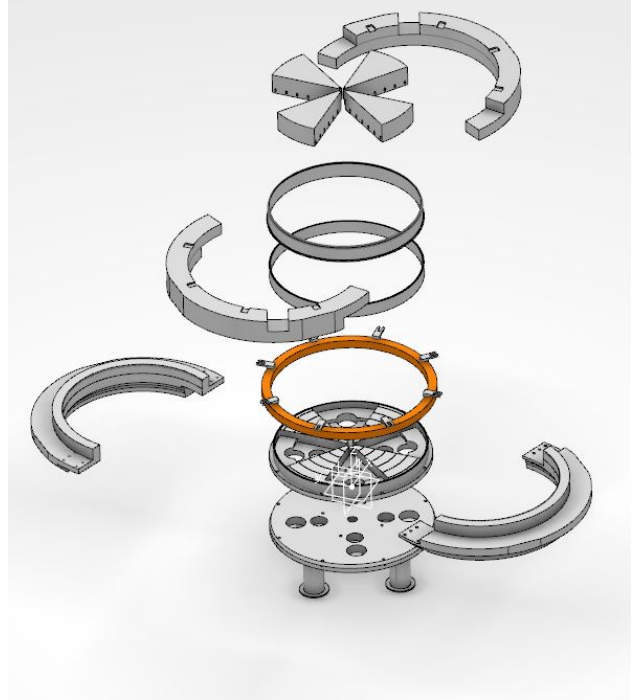


Figure 3.4: Cyclotron lower steel exploded.

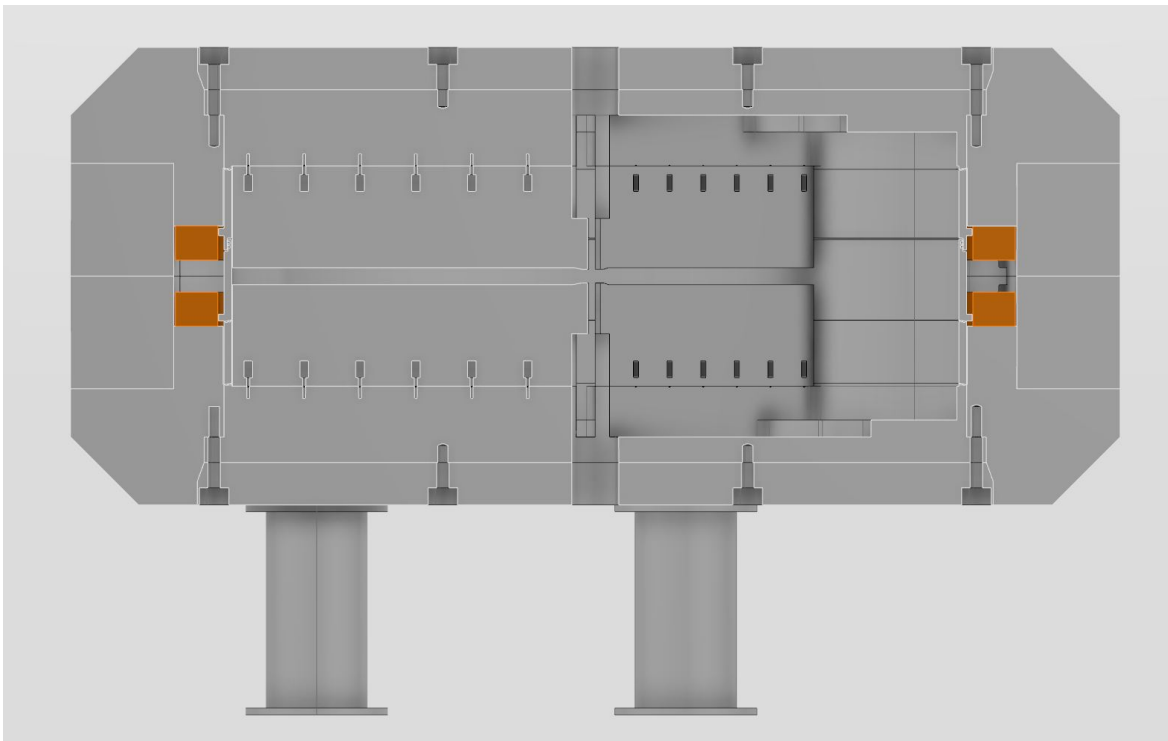


Figure 3.5: Cyclotron cut view

Name	Mass (Metric Ton)	Dimensions (mm)
Upper and lower external disk	30	Ø4700*250
Upper and lower internal disk	36	Ø4620*463
Upper and lower flux return (1 and 2)	36	3100*1950*1015
Upper and lower median plane flux return (1 and 2)	29	3100*1950*705
Upper and lower pole	7	2013*1290*600

Table 3.1: Yoke part properties

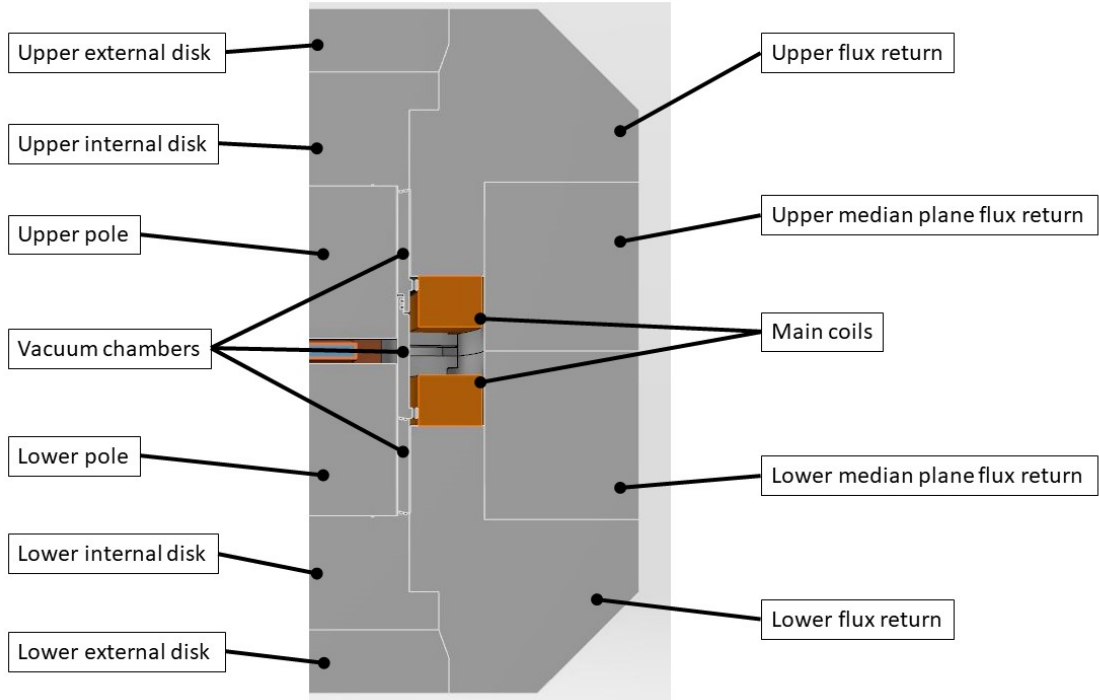


Figure 3.6: Cyclotron detailed cut view

## 3.2 Cyclotron magnetic performance

In this section we describe the latest modifications applied to the cyclotron regarding its magnetic properties. We will compare the results with the model from the Conceptual Design Report (CDR) from [6] to ensure its magnetic performance remains within specifications.

With the latest design of the vacuum chamber, see section 3.5, the pole radius was slightly reduced. To keep the magnetic field isochronous up to extraction at 120 MeV, the outer radius required small modifications, see left image in Fig. 3.7. First, the curvature was modified to follow the curvature of the last orbit. This enhances the total flux in the region where needed. Second, the top layer of the pole at its outer radius will be made of permendur. This alloy has better magnetic properties at high field strengths. Using permendur will enhance the magnetic



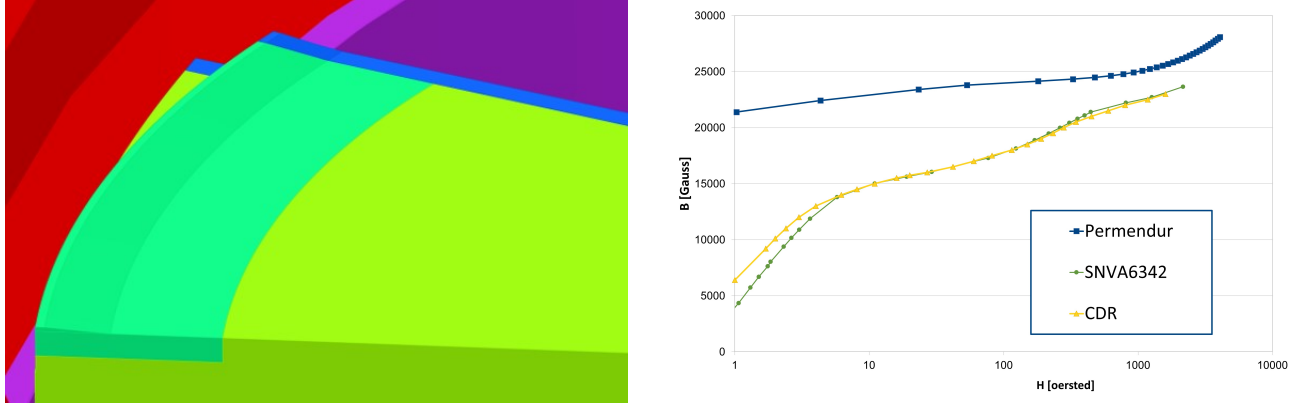


Figure 3.7: Left: Detailed view of the outer radius of the pole; only half of one pole is shown. In red is the coil, in light green is the pole made of SNVA6342 steel. The turquoise part is a piece 30 mm in height and 200 mm in width made of permendur. In blue we see the pole edge made of SNVA6342 steel, which can be shimmed to isochronize the magnetic field. Right: BH curves for the two steel types used: Permendur and SNVA6342. As reference, the BH curve used for the cyclotron in the CDR is also shown.

flux. Finally, the pole height is increased by a slanted ridge at its extremity. This reduction of the pole gap should have no effect on the transmission and can be tuned to improve the dB/dr for the last orbits.

The steel used for the cyclotron yoke and poles is the SNVA6342, also used, for example, in the C400 cyclotron (see Ref. [47]). Its BH-curve is shown in Fig.3.7. Here, we also see the better performance of the permendur alloy.

### 3.2.1 Isochronization

The edge of the pole can be shimmed to isochronize the magnetic field map. In Fig. 3.8 the latest results are given. The left image shows the shimming applied, the right image shows the offset in magnetic field, as required for a given RF-frequency. For comparison, the offset (expressed as dB in Gauss) for the model of the CDR is also shown.

The plot shows that the magnetic field is stable and strong enough up to a radius of 2 meters, which is the equivalent of 121 MeV. In Fig 3.9 the phase slip can be seen to stay within the  $\pm 10^\circ$ . The horizontal and vertical tunes are also given in the same figure. Here we see that there is a crossing of the tunes at high radius, invoking resonances which could impact the extraction.

As a conclusion, we can state that a configuration is possible with an isochronous magnetic field for up to 121 MeV. The transition to permendur at high radius, together with an abrupt slanted pole face, requires shimming of the pole edge. In a further study, these last modifications can be made more smooth, as not to have too much of a fluctuation in the dB for the last orbits and thus tunes that do not cross anymore, avoiding possible resonances.

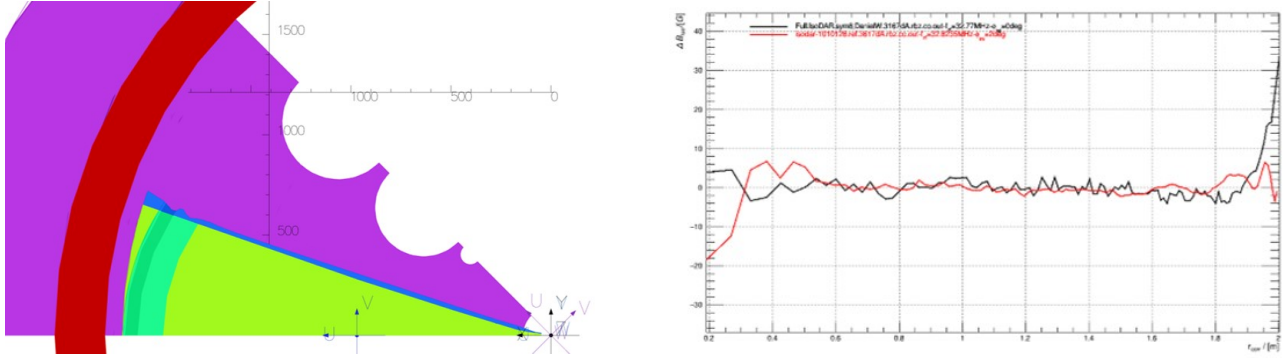


Figure 3.8: Left: Pole edge of isochronized model. Right: The dB [Gauss] as a function of radius [meters], for the CDR model (in black) and the newest model (in red). Note that a positive dB means there is too little field at specific radius, a negative dB implies there is too much field. The RF-frequency for the CDR model is at 32.77 MHz, for the newest model it is 32.82 MHz.

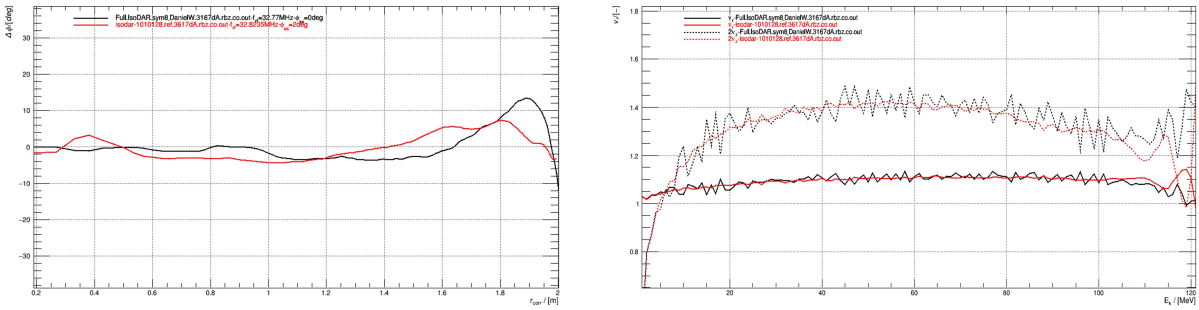


Figure 3.9: Left: phase slip as a function of radius. Right: vertical and horizontal tunes as a function of energy (dashed and solid lines respectively). Shown are the results for the CDR model (in black) and the newest model (in red).

### 3.2.2 Risks and Mitigation

**Risk: Manufacturing Imperfections.** Because no manufacturing process is perfect, we must measure the local magnetic field developed by the accelerator magnet in an iterative process. During the mapping iterations, physicists compare measurements results with expected calculated (theoretical) magnetic field map values and propose local magnet iron shape adjustments, typically on pole tips. Difficulty of the process is a risk.

**Mitigation:** *For that reason, pole tips, or at least the edges of the pole tips (boundary valley/hill) must be dismountable to allow re-machining and multiple tuning iterations. This mapping process is repeated until the final expected map is obtained, allowing, theoretically, the appropriate beam acceleration and extraction. In the case of IsoDAR, we can either perform the entire process underground, or the machine must be dismantled after surface tests and re-installed underground. This will require re-measuring the magnetic field after assembly on site, during a second (shorter) mapping campaign.*

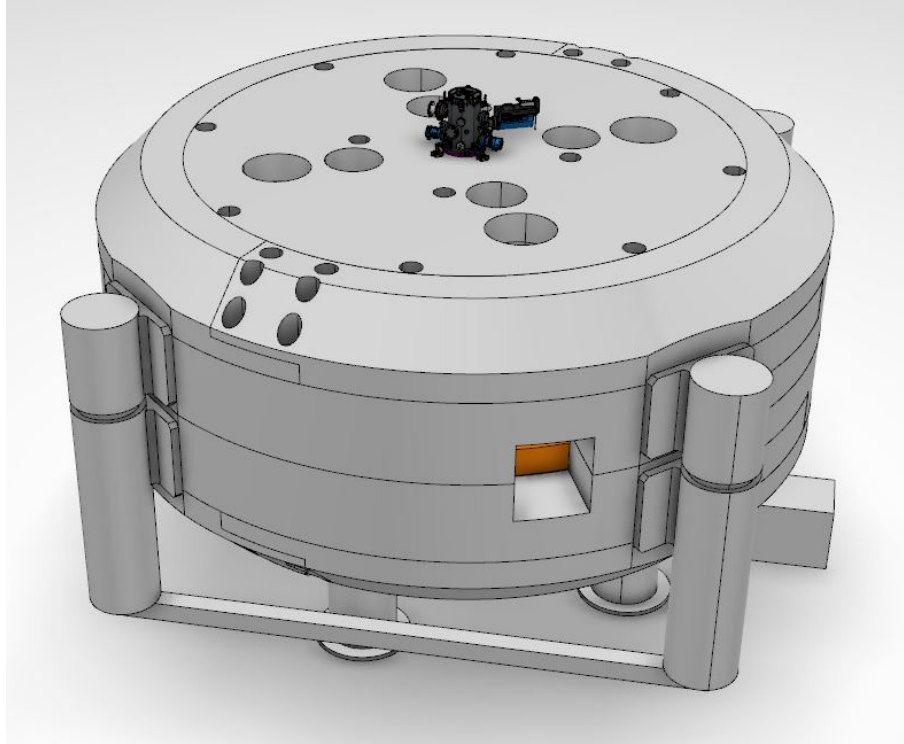


Figure 3.10: RFQ overview.

**Risk:** Mapping Tool. Developing a mapping tool requires care as this tool accuracy will define performance accuracy of the measured magnet itself.

**Mitigation:** *Many precautions are mandatory concerning calibrations, mechanical stiffness, thermal stability and tracking as well as the use of perfect "non-magnetic" materials (to avoid measures perturbations and unexpected distortions).*

### 3.3 Interface with the RFQ

The RFQ will sit on top of the cyclotron along its central axis, as shown in Fig 3.10. This places the RFQ outside of the cyclotron's vacuum. Therefore, a vacuum sleeve will be used to ensure the integrity of the cyclotron's vacuum. This sleeve will be fixed on top of the upper external disk and the vacuum sealing will be done radially on the upper internal disk (as seen in figure number 3.12 ). The O-rings will have a cross sectional diameter of 8mm and an inner diameter of 305mm.

In order to allow for adjustment, the RFQ sleeve allows a rotation of 5mrad around the lower O-ring contact patch (discussed with the manufacturer of the RFQ). The RFQ sleeve is as thin as possible to avoid any loss in magnetic field in the central region (hence the O-rings in the Yoke parts).

As shown in Fig. 3.13, vacuum sealing will occur at the base of the RFQ using a thick O-ring

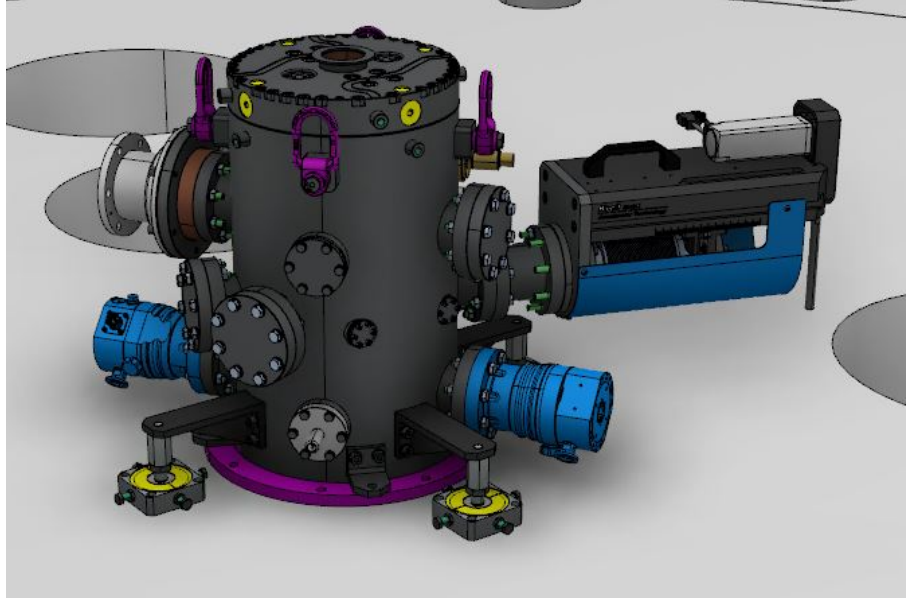


Figure 3.11: RFQ zoom.

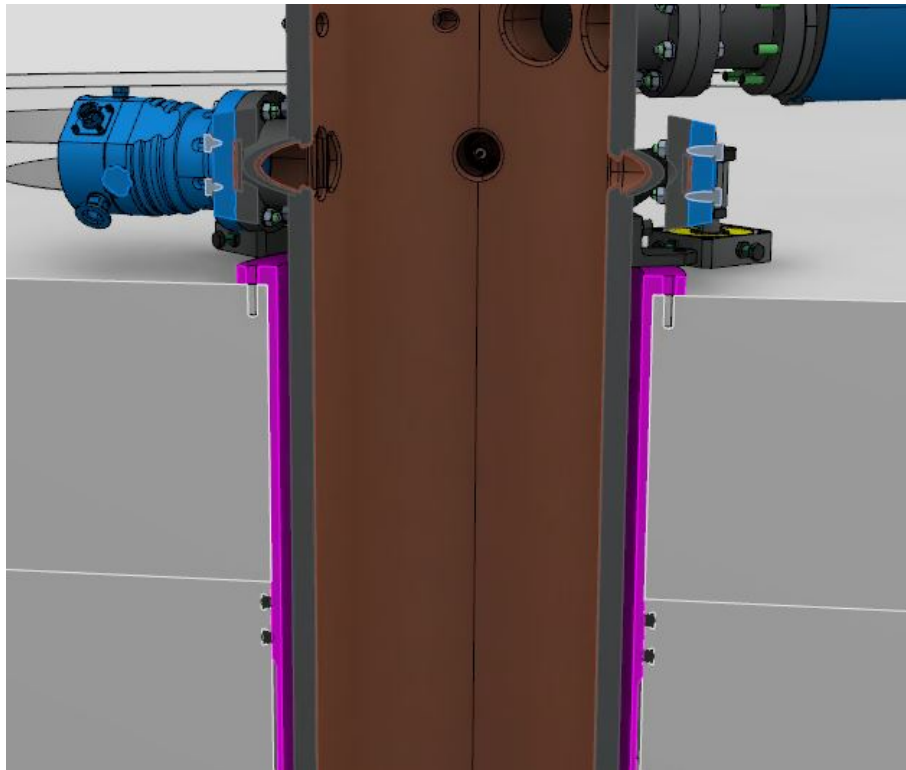


Figure 3.12: RFQ cut section 1.

(diameter 10 mm) which will self-seal under the RFQ's weight ( $\approx 3000$  N). The dimensions of the vacuum sleeve are listed in Table 3.2.

In order to allow fine-tuning the cyclotron alignment, a set of adjustment feet, shown in Fig. 3.11,

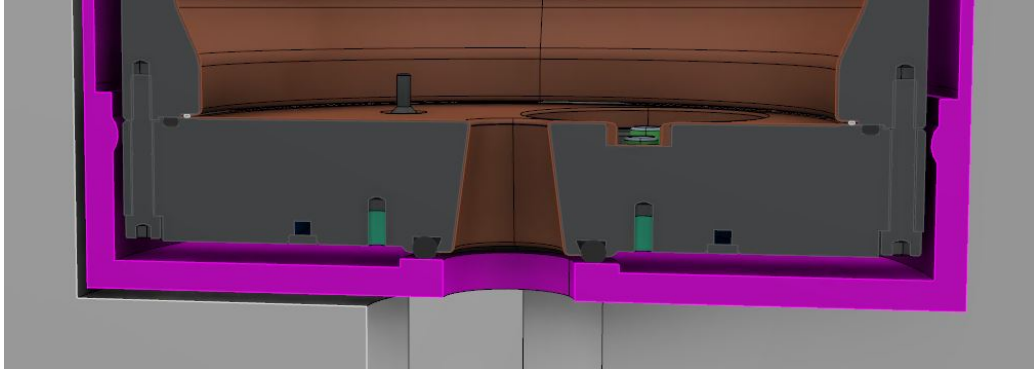


Figure 3.13: RFQ cut section 2.

are fixed to the cyclotron yoke. By using four groups of set screws and one vertical adjustment nut, the following alignment modifications can be made.

- Rotation:  $\pm 5^\circ$
- Tilt:  $\pm 5$  mrad
- Lateral movement:  $\pm 1$  mm

In addition to this fine-tuned alignment, a coarse alignment step is envisioned during the initial assembly and commissioning procedure.

### 3.4 Central Region

The injection system design is a crucial component that allows us to achieve a high beam current. Our design balances injecting the  $H_2^+$  molecule at high energy against avoiding the use of complex high-voltage platforms. Higher energy injection mitigates space charge and reduces geometrical (non-normalized) emittance. An energy of 35 keV/amu was selected. This in turn determines the target output energy of the RFQ. As in commercial cyclotrons, an axial injection system based on a Spiral Inflector (SI) will be used to bend the beam from the axial direction to the median plane. We have investigated several refinements to a traditional spiral inflector which will be discussed subsequently, but the concept, as implemented successfully in a previous

Table 3.2: Vacuum Sleeve Dimensions.

Name	Value
Height	1030.5mm
Outer diameter	304.55mm
Inner diameter	296.55mm
Weight	18kg

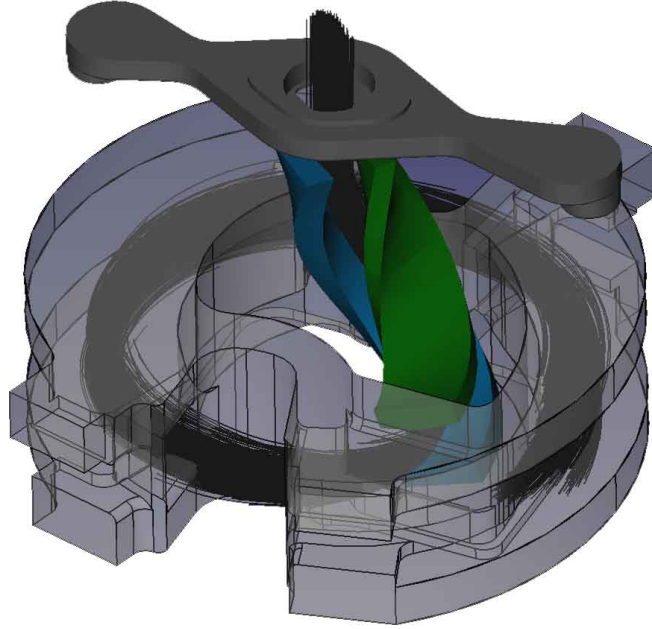


Figure 3.14: CAD rendering of the spiral inflector and particle trajectories as implemented previously for early tests at Best Cyclotron Systems, Inc. [34]. The positive and negative electrostatic deflectors are shown in blue and green respectively. The cyclotron magnetic field in this image is directed vertically upwards. Particles enter the spiral inflector via the rectangular grounded collimator (solid gray) and are guided into the cyclotron mid-plane by means of the cyclotron magnetic field and the electrostatic potential between the electrodes. The copper housing (transparent gray) isolates the spiral inflector from the RF fields driving the cyclotron. From Ref. [48].

iteration of this work and tested at Best Cyclotron Systems, Inc., is visualized in Figure 3.14 using trajectories calculated with OPAL [49].

The exit point of the spiral inflector is also the starting point of acceleration in the Central Region (CR) of the cyclotron. First turn acceleration is then achieved by the dee tips extending into recesses in the spiral inflector housing. The shapes of the dee tips and the spiral inflector housing have been designed to guide the particles from the spiral inflector exit to the acceleration region while providing the necessary energy gain and beam focusing.

The central region and the spiral inflector must be designed carefully and together because they have strong interplay. This procedure has already undergone one past iteration in the summers of 2013 and 2014 at Best Cyclotron Systems Inc. In the following sections, we will discuss improvements to this design which will be incorporated into the preliminary design for the full IsoDAR machine.

### 3.4.1 Spiral Inflector Overview & Design Considerations

The axial injection of the ionized beam into a cyclotron is realized using an electrostatic device called a spiral inflector, which consists of two curved electrode deflectors (see Figure 3.14). The electrostatic potential between these electrodes is able to bend the beam  $90^\circ$  from the axial line to the median plane of the cyclotron. The helical trajectory of the beam is determined both by the shape of the electrodes, the electrode potentials, and by the magnetic field of the cyclotron as the beam is bent into the median plane. In order to isolate the inflector region from external fields as much as possible, grounded entrance and exit apertures and a grounded copper housing are also included.

An ideal spiral inflector would do nothing more than rotate the beam by  $90^\circ$ , introducing no additional beam divergence or losses and seamlessly merging with initial accelerating in the central region. Further, in order to achieve this degree of bending in the small space of the central region,  $\mathcal{O}(kV)$  potentials are required, so it is important to minimize or even eliminate any  $H_2^+$  impact on the electrodes to prevent sparking.

It is also important to consider the impact of a realistic magnetic field when designing our spiral inflector. This is particularly important for the IsoDAR inflector because of its relatively large size. Unlike other spiral deflectors that have been constructed, we will require a larger gap and plate size due to the non-negligible space charge and higher rigidity of  $H_2^+$ . This larger volume means that variations in the magnetic field along the trajectory are non-negligible. Accordingly, all following work uses a full 3D magnetic field map generated using OPERA.

### 3.4.2 Designing the Inflector

Ultimately, an additional iteration of production and empirical testing of the final IsoDAR inflector will be performed. To optimize the inflector beforehand, we use a numerical optimization procedure to inform the best theoretical parameters.

For an inflector in a uniform magnetic field, analytic solutions to particle tracking exist for the central trajectory. However when 3D magnetic variations and/or off center trajectories are considered a numerical approach is required.

An initial estimate based on an analytical solution for a central track serves as a numerical starting point, after which the mesh generating software gmsh [50] is used to produce surface representations which inform subsequent electrostatic analysis. Python’s BEMPP API [51] is then used to perform boundary analysis.

In short, this procedure enables a geometric model of our inflector to yield a full 3D electrostatic. Particles can then be tracked with high precision using the Boris method [52].

A major strength of this procedure and choice of software is speed, with a full simulation iteration taking only  $\mathcal{O}(\text{hours})$ . Prior work [53] comparing this process to commercial software such as COMSOL demonstrates that the differences in field calculations are negligible.

### 3.4.3 Geometric Refinements

In most spiral inflectors, the two electrodes would be rectangular prisms if flattened out. They remain parallel to each other with locally flat surfaces while spiraling. Hereafter we will call this a “Traditional” spiral inflector. A traditional inflector can effectively transfer particles, but for off center paths these inflectors can introduce beam divergences in energy and position which were not present in the initial beam.

We address this by adding several refinements to prior inflector iterations.

- Beam focusing between the RFQ and spiral inflector
- Introducing V-shape
- Introducing plate angling
- Modifying the terminal end to a wedge

The addition of intermittent beam focusing ensures that the  $H_2^+$  entering the spiral inflector are as near to the central trajectory as possible. This is accomplished by the addition of electrostatic quadrupoles in the gap between the RFQ and inflector entrance (see also Fig. 1.7). Using the output of the RFQ simulation [54] as input to the quadrupoles, geometry and potentials were optimized such that the tightest possible input beam is produced.

The remaining three modifications: V-shape, plate angling, and the terminal wedge were motivated by work done by Barnard et al. [55]. These all have the effect of introducing quadrupole moments to the field of the inflector itself, which can provide mid-track focusing to minimize beam dispersion in flight.

The V-shape introduces a concave v-shape to the anode and a convex v-shape to the cathode when viewed along the long axis of the electrode (Fig.3.15a). Plate angling reorients the plate angle relative to each other along the course of the inflector. In other words the plates are parallel only in the center with a positive angle between the plates initially linearly transitioning to an equal and opposite negative angle by the end (Fig.3.15b). The terminal gamma wedge cut modifies the end of the anode into a triangular rather than flat profile at the end and shortens the cathode. This assists with the fringe fields at the end which can produce vertical spreading. (Fig.3.15c).

These modifications and their associated focusing fields interplay, but can be independently varied alongside other parameters like electrode potential, electrode separation, etc. We are actively exploring different techniques to handle this high-dimensional optimization problem. Monte Carlo sampling is typically well suited to this sort of optimization, but studies in which only one parameter is varied at a time have illustrated that optimization extrema can be relatively narrow, necessitating a significant, if not intractable, amount of computation time.

As we are at the edge of practical optimization using Monte Carlo, this leads us to consider other potential alternatives. Surrogate models using a fully connected neural network capable of learning and interpolating underlying features have been previously explored[56] [57] [58].



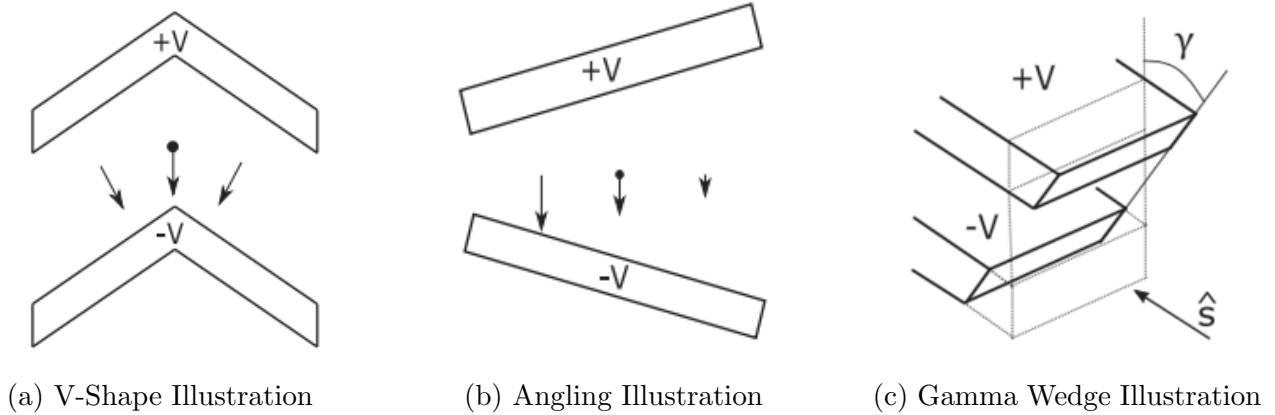


Figure 3.15: Illustrations of different focusing concepts. From Ref. [55].

Initial iterations have proved promising and have informed the parameters for our current best inflector performance. As this work matures, it will be detailed in upcoming publications.

### 3.4.4 Characterization of Spiral Inflector

The result of adding optimized focusing quadrupoles on the beam distribution entering the spiral inflector is illustrated in Fig. 3.16.

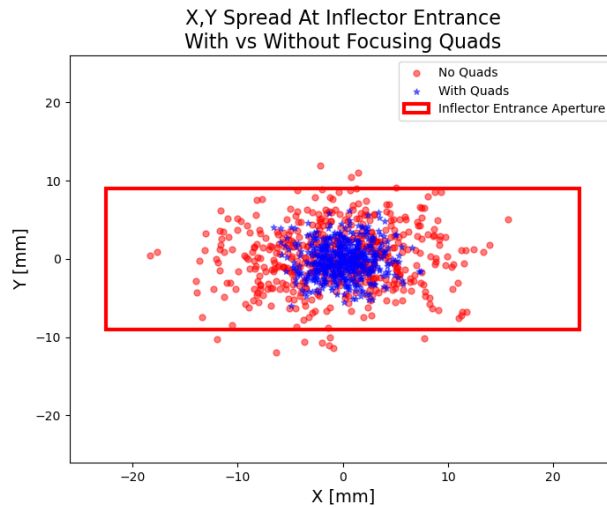


Figure 3.16: Illustration of beam tightness at the entrance of the spiral inflector before and after the addition of focusing quadrupoles between the RFQ and inflector

The optimized spiral inflector, with  $H_2^+$  tagged through, is illustrated in Fig.3.17.

The efficiency of this modified inflector is significantly improved. Efficiency must be thought

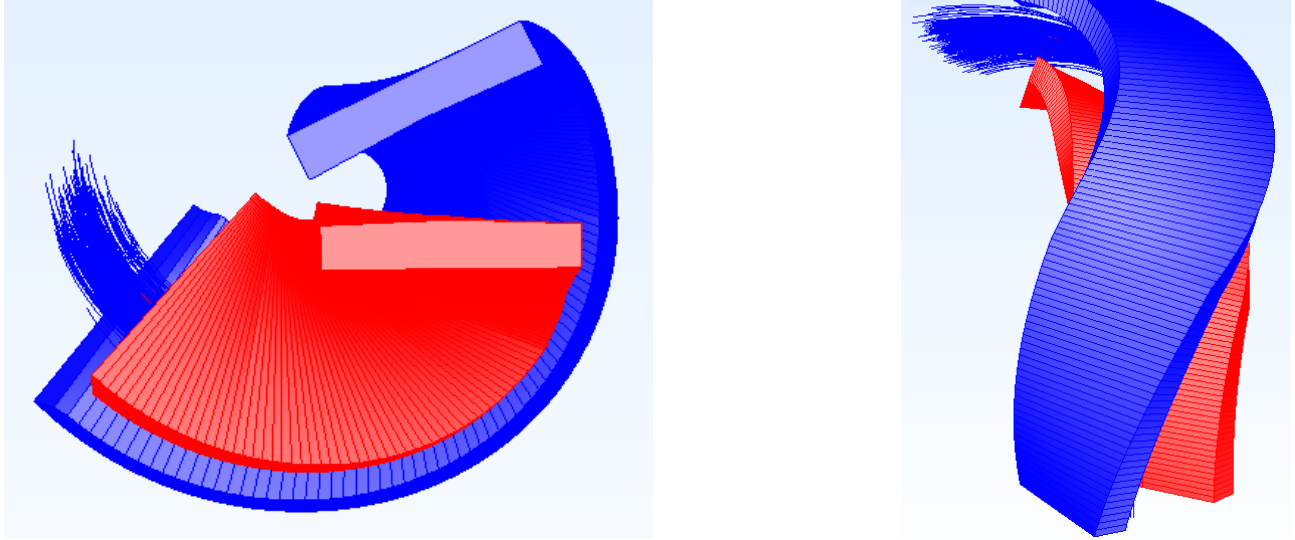


Figure 3.17: Illustrations of the optimized spiral inflector. Note the v-shape to the electrodes as well as the non-parallel angle seen in the bottom view, and the angled wedge visible in the top view.

of from two fronts. On the one hand we wish to transmit as much current from the RFQ into the cyclotron as possible. Particles which are not successfully transmitted must terminate somewhere. Termination on grounded apertures is acceptable while termination on the HV electrodes will result in sparking and can have significantly impact on running. It is therefore also vital to specifically consider the fraction of ions that terminate on an electrode.

We thus consider two similar cases. Both have identical optimized spiral inflectors. The difference is whether or not a grounded collimator is placed at the entrance to further narrow the entering beam beyond what the quadrupoles have provided. This collimator is a circular aperture which, for this study, was chosen to be as large as possible while guaranteeing that less than one percent of  $H_2^+$  impact the electrodes. The resulting efficiencies and  $H_2^+$ -electrode collisions are given in Table 3.3.

Table 3.3: Comparison of efficiency and ion-electrode impact for the optimized vs traditional spiral inflector.

	Efficiency	Electrode Impact %
<b>Traditional Inflector</b>	74%	17%
<b>Optimized Inflector</b>	97%	1%
<b>Traditional Inflector (Coll.)</b>	39%	< 1%
<b>Optimized Inflector (Coll.)</b>	93%	< 1%

We also need to consider the impact of the new inflector on the quality of the beam which is successfully transmitted. These changes are characterized in Table 3.4. Detailed histograms

showing the kinetic energy distribution of the  $H_2^+$  at the entrance and exit of the inflector are shown in Fig. 3.18.

Table 3.4: Comparison of transmitted beam parameters at the inflector exit.

	$\sigma_x$ [mm]	$\sigma_y$ [mm]	$\sigma_z$ [mm]	$\sigma_r$ [mm]	$\sigma_{KE}$ [keV]
<b>Traditional Inflector</b>	3.0	3.9	10.1	2.3	4.0
<b>Optimized Inflector</b>	4.9	2.7	6.4	2.4	3.1

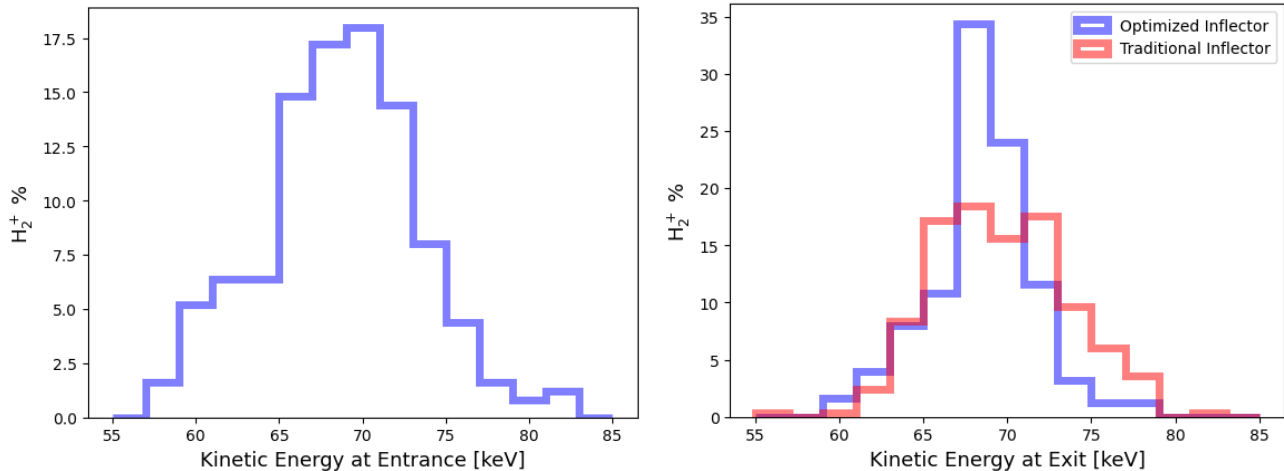


Figure 3.18: Illustration of the kinetic energy distribution of the  $H_2^+$  prior to the inflector entrance vs at the inflector exit.

### 3.4.5 Orbit Matching and Beam Centering

Once the beam emerges from the spiral inflector, it must be properly matched in terms of orbit radius, radial momentum, and phase. A specially designed shape of the inner ends of the RF cavities performs this duty. The angles and widths of the accelerating gaps of each cavity are modified in an optimization procedure during the first two turns to place the beam onto a static equilibrium orbit appropriate for the respective energy. The center of a full integrated orbit after these two turns should then align well with the cyclotron center.

The spiral inflector end can be tilted (often this parameter is called  $k'$ ) to aid in the matching and thus becomes part of the optimization procedure.

A preliminary design study of the IsoDAR central region was performed by the company AIMA in France [59]. The AIMA central region model is shown in Fig. 3.19. This central region was designed with a slightly different magnetic pole shape and with its own matched spiral inflector, using the output beam from an early RFQ beam tracking and single electrostatic quadrupole transverse refocusing element. It demonstrated that the RFQ-generated beam could be injected and vertically focused. By using a single collimator (removing  $\approx 42\%$  of the beam), an edge-to-edge turn separation of 1 cm was achieved in the fourth turn (approximately 1 MeV/amu).

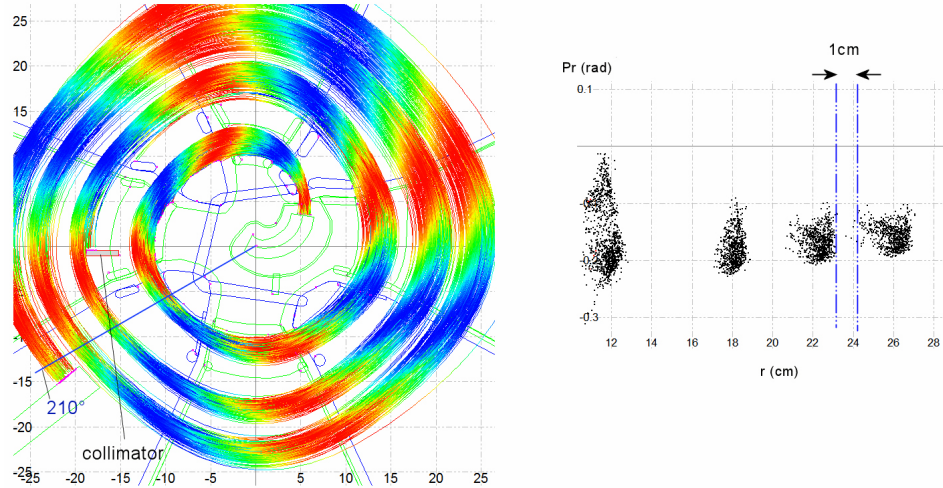


Figure 3.19: Beam tracking result from the AIMA central region study. Left beam centering and acceleration on top of a view of the electrodes. Colors correspond to particle phase. Right: 1 cm turn separation in the fourth turn with a single collimator. From [59].

The RMS beam size and energy spread was significantly worse than what we see in our optimized inflector. Furthermore, the AIMA study did not consider space charge, which is fundamental to establishing vortex motion (see below). Somewhat counterintuitively, including space-charge will improve the results further; as will our new optimized spiral inflector.

In the next step, we will modify the central region and optimized spiral inflector to match well and track particles through the finalized geometry with OPAL using the PIC method to demonstrate a stable vortex.

For this preliminary design, we use a Gaussian beam with size and emittance informed by the AIMA study for further simulations of acceleration to 60 MeV/amu.

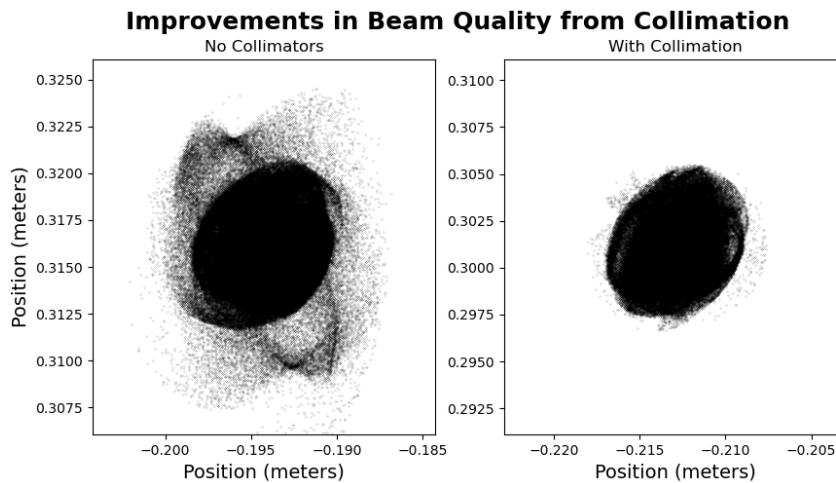


Figure 3.20: Reduction of beam halo by collimators

### 3.4.6 Low Energy Collimation

Following injection, there is significant beam spread in the first few turns of the cyclotron that we need to manage. We do this by placing a series of collimators around the beam core in the early turns. We must do all of our collimation in the first 7 turns of the primary acceleration, corresponding approximately to a 2 MeV/amu limit, to avoid activating our collimators. The placement of the collimators is shown in Figure 3.21. The reduction in RMS spread is shown in Fig 3.41. In total, we have 15 collimators that remove 36.1% of the beam. The improvement in beam shape is shown in 3.20. With time, the halo slowly redevelops but to a lesser extent than it would without collimation.

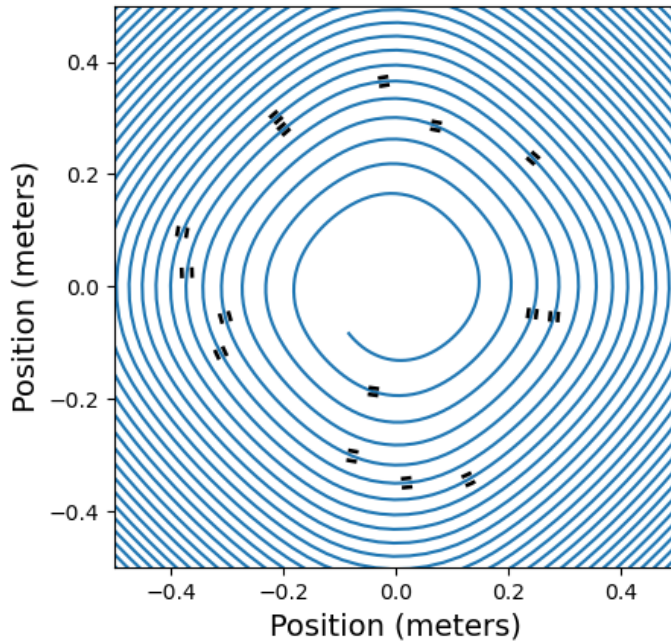


Figure 3.21: Placement of 15 collimators in first 7 turns

It is necessary to make the beam as circular as possible following the low energy collimators so that the beam is well-matched to “vortex motion.” Vortex motion stabilizes the beam and significantly reduces beam growth over time. It arises from the interaction between the self-field of the beam and the external magnetic field of the cyclotron. Vortex motion is discussed in depth in Ref [60].

### 3.4.7 Risks and Mitigation

**Risk: High voltage on the spiral inflector electrodes.** The high voltage on the spiral inflector electrodes can lead to arcing from one electrode to the other or to ground, creating unstable injection conditions.

*Mitigation:* During the BCS tests we were able to run the spiral inflector electrodes as high as  $\pm 13.5$  kV without beam using conventional polishing and cleaning methods for the electrodes. Electro-polishing and conditioning in an inert gas environment will improve this even more. Beam striking the electrodes could potentially induce arcs through electron emission. This can be avoided by presenting a well-defined beam to the spiral inflector to assure close to 100% transmission. We have and will continue to emphasize minimizing or completely eliminating ion impacts in simulo with these tools. Finally, we will set up machine protection algorithms that can break a spark and restart acceleration in a controlled manner to minimize downtimes due to sparking.

### 3.5 Vacuum Chamber

The vacuum enclosure comprises five parts: the upper and lower internal disk and 3 vacuum chambers. Fig 3.22 shows the vacuum enclosure in detail and the dimensions are in Table 3.5. The vacuum sealing is done using 2 metallic O-rings per interface (e.g., from Omniseal [61]) except for the radial interface where Polymer O-rings could be used. The interface for the accessories will be done using a sleeve design and radial O-ring, described in Fig. 3.22.

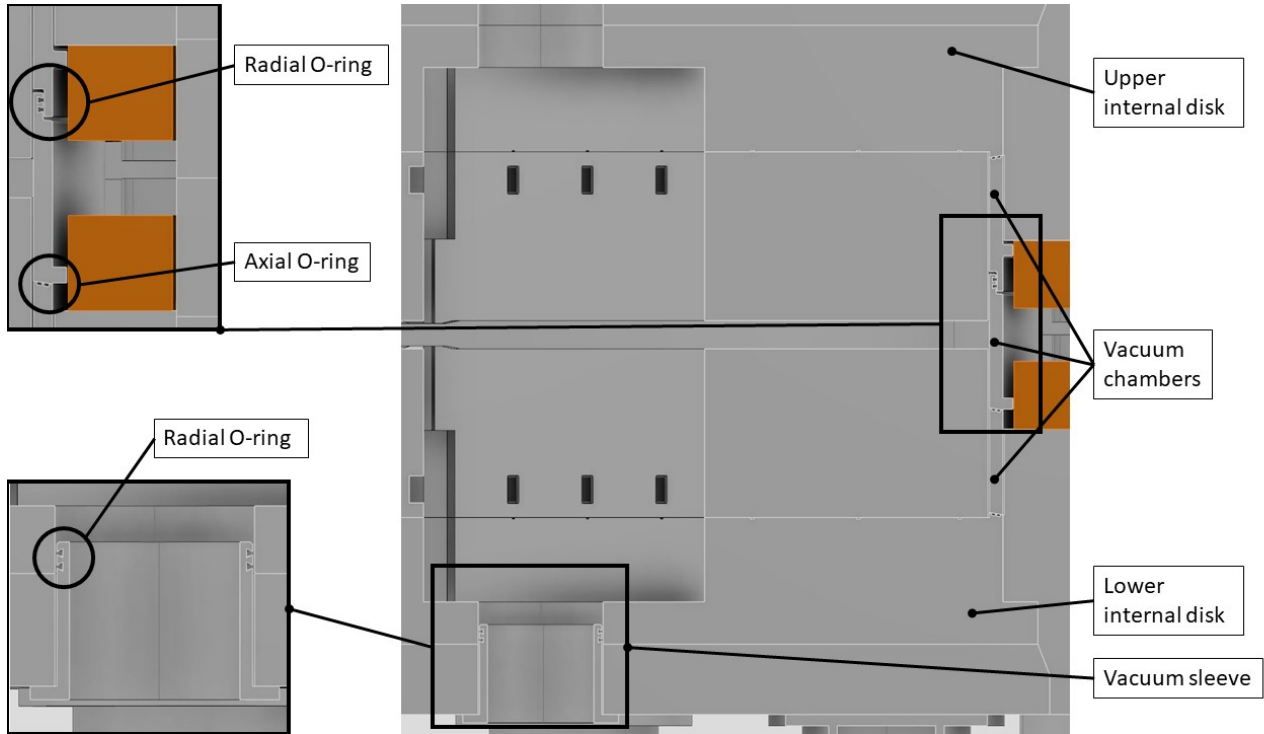


Figure 3.22: Cyclotron vacuum chamber details

Name	Mass (Metric Ton)	Dimensions (mm)
Upper and lower internal disk	36	Ø4620*463
Upper vacuum chamber	2.3	Ø4452*483
Lower vacuum chamber - median plane	2.3	Ø4452*483
Lower vacuum chamber - internal disk	1.8	Ø4386*380

Table 3.5: Vacuum part properties

### 3.5.1 Risks and Mitigation

**Risk: Achieving the required vacuum level in the presence of the beam.** The calculated required vacuum is  $5 \cdot 10^{-8}$  mbar. Before the beam is turned on, the pumping plan provided will reach this with little difficulty, assuming there are no vacuum leaks. However, introduction of beam, with gas-desorption from surfaces hit by stray beam particles, could raise the pressure above the acceptable level.

***Mitigation:** Beam losses from other sources will be minimized. In addition, options for further surface cleaning and treatment, as well as the possible addition of more pumping capacity, should be developed.*

## 3.6 Coil configuration

The CDR anticipated a slightly shorter coil than we now anticipate using. Specifically, the coil height has been increased from 200 to 240 mm. Its radial width remains at 250 mm. The total current used in the calculations is 180,850 amp-turns in each of the half coils. The apparent current density is thus 3.01 A/mm<sup>2</sup>, i.e. 5% lower than the 3.17 A/mm<sup>2</sup> foreseen in the CDR. For now, no extraction channels are anticipated in the return yoke. If they are added, an increase in main coil current will be required

In Fig. 3.23 a schematic view of the coil is given. Also, a possible configuration of winding and cooling is calculated. Although this configuration does not exactly sum to a cross-section of 240 by 250 mm<sup>2</sup>, it shows that a cooling configuration is feasible.

Working in pancakes gives the possibility of manufacturing the pancakes outside the cave and stacking them inside. The increase in height from 200 to 240 mm is the equivalent of adding an extra pancake.

## 3.7 Cyclotron RF System

The RF system for the IsoDAR cyclotron produces the primary acceleration of the ion beam and can be divided into the following subsystems:

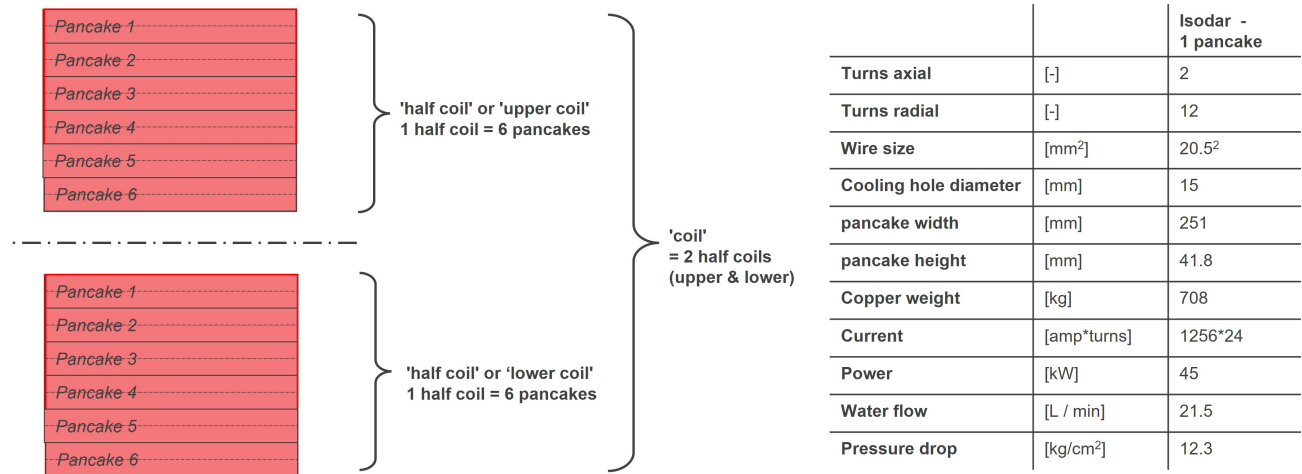


Figure 3.23: Left: Schematic view of a cross-section of the main coil, with six pancakes per half coil. Right: Possible configuration of the winding, using a square conductor with a round cooling channel in its center.

- The RF cavities which accelerate the beam and provide large inter-turn separation. The cavities are wedge-shaped and are located in the magnet valleys. There are 4 such cavities. The inner part is often called a *dee* whereas the outer part is called a *dummy-dee*.
- The RF tuning system that will compensate for the thermal drift of the cavities and maintain a stable resonating frequency.
- The RF amplifiers that provide the necessary power to create the required RF electric field inside the cavity.
- The RF couplers that inject the RF power from the amplifiers into the cavities
- The Low Level RF system (LLRF) that controls and regulates the RF amplitude on the Dee and drives the tuning system.

We consider these in the Sections below. The numerical parameters of the RF system are listed in Table 3.6.

### 3.8 RF Cavities (Dees, Stems and Liners)

The RF cavities of the cyclotron have been designed using CST microwave studio [62] in order to define the shape of the Dee and the Dee stems. We optimized our designs to reach the right resonance frequency, satisfy the Dee voltage Law, and minimize power dissipation. Ultimately, this improves the quality factor (Q-factor).

The Dees and cavity walls are all made of oxygen-free high-conductivity (OFHC) copper, which has good electrical conductivity and good solderability. The Dees are fabricated out of a 20 mm



thick copper plate and are made rigid by a supporting arm. The four round stems support the Dee and provide the right inductance in order to produce the required resonance frequency. Their size and location produce the desired Dee voltage vs. radius profile. Each Dee will be equipped with vacuum pumping panels to efficiently pump the median plane. One Dee is equipped with one electrostatic deflector for extraction. This fact has not been taken into account in detail in the RF simulations to date, but some room for housing the deflector has been provisioned at the back of the Dee. Figures 3.24 and 3.25 present the main elements composing the RF cavities.

### 3.8.1 Integration of preliminary central region in RF Cavities

In order to compute a more accurate voltage radial dependency law, we have integrated the central region design proposed by AIMA [59] into the RF cavity modelling, several technical choices were made to ensure the effective implementation of this innovative configuration:

- The central region design was trimmed at 150 mm from centre.
- Both the Dee and counter dee original central region was removed by trimming the cavities at 250 mm from centre.
- Sections were cut straight, and a linear transition (loft) technique was used to achieve the connections between the trimmed components.

The figure 3.26 shows the final integration of the central region. The lofted transitions can be better seen from top at figure 3.27. They leads to an acceptable linear vertical gap opening from 26 mm at a radius of 150 mm, to 50 mm at a radius of 250 mm. The section view of the model, presented at figure 3.28, shows the radial evolution of the vertical gap. In addition, adequate

Table 3.6: Details of the RF design.

<b>RF System Component</b>	<b>Design Value</b>
Resonance Frequency	32.8 MHz
Dee voltage in the central region	65 kV
Dee voltage at extraction radius	230 kV
Dee radial extension	2 m
Acceleration gap angle	42°
Cavity height	1812 mm
Number of Dee stems	4 per Dee (2 up, 2 down)
Number of Dee's	4
Acceleration harmonic	4th
Power dissipated per cavity	113 kW
Cavity Q-factor	9620

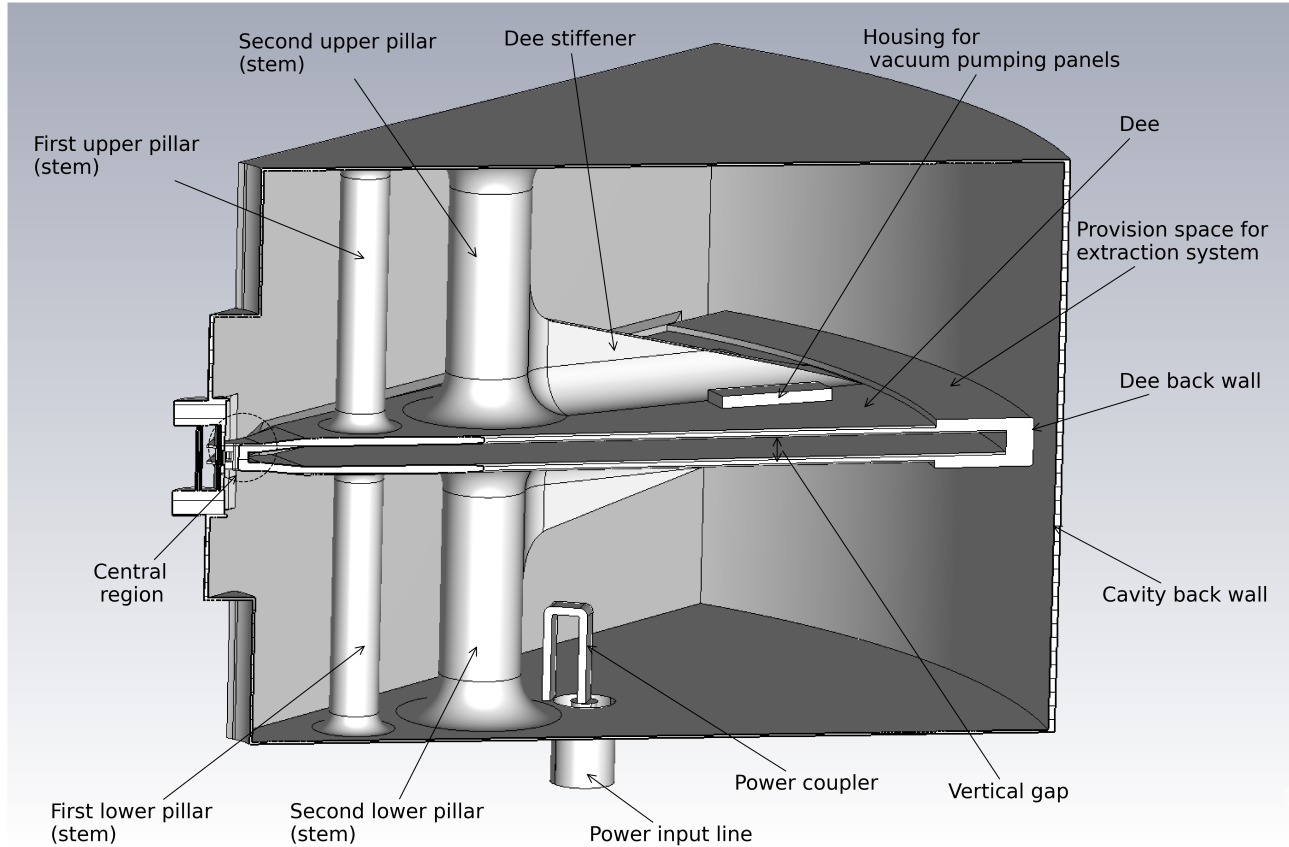


Figure 3.24: Section view of the RF cavity.

clearance provisions were incorporated, specifically to fit the inflector and optics coil. Symmetry with regard to the median plane symmetry was maintained. Power bridges between dees in the central regions were removed since we recommend to power the 4 cavities independently.

### 3.8.2 RFQ Integration in RF Cavities

Some clearance provision has been set for the integration of the RFQ, as seen in figure 3.29

- Diameter 280 mm
- Down to 35 cm of median plane

While the RFQ will only be in the upper location, we have decided to keep median plane symmetry, for computation, manufacturing, and performances purposes. We have observed that the RFQ clearance has a low impact on cavity frequency and performances, and the output of the RFQ could be lowered more without impacting the cavity behavior.

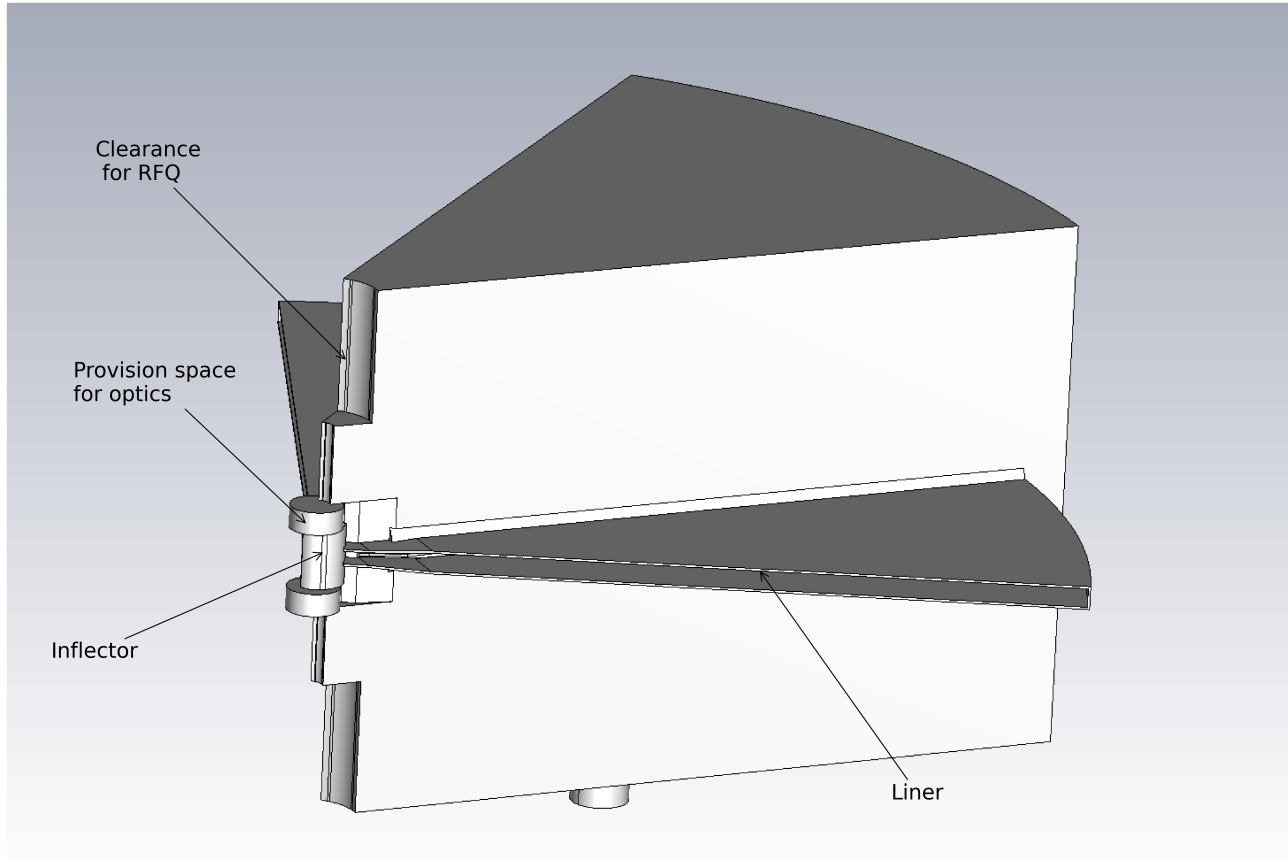


Figure 3.25: Outer view of the RF cavity.

### 3.8.3 RFQ getter pumps in RF Cavities

Incorporating getter pumps into the Dees allows us to improve our vacuum quality. By integrating three housing for SAES UHV1400 getter pumps [63] per dee, we aim to ensure highly efficient and reliable vacuum performance within the Cyclotron system. The use of six of those getter pumps per cavity facilitates the effective removal of residual gases, since achieving and maintaining ultra-high vacuum conditions essential for optimal particle acceleration. The figure 3.30 shows acceptable locations for three getter pump housings. Furthermore, our preliminary assessments suggest that it may be feasible to scale up the configuration to include up to two sets of five getter pumps per cavity. The very low electrical field of the locations of the housings will allow the getter pumps to function safely.

This early integration of the housings of the getters in the dees is mandatory to assess their impact on the cavity frequency, and on surfaces currents. However, to finalize this integration, comprehensive vacuum computations will be needed. These computations will enable us to determine the ideal amount of getter pumps, ensuring a properly engineered vacuum system that underpins the overall success and efficiency of the Cyclotron.

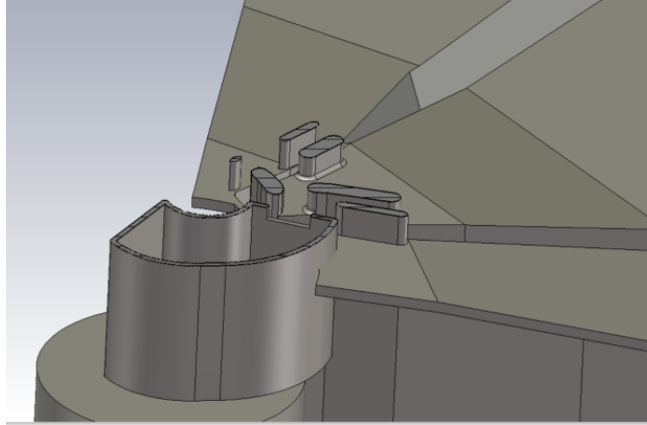


Figure 3.26: dees at central region close view

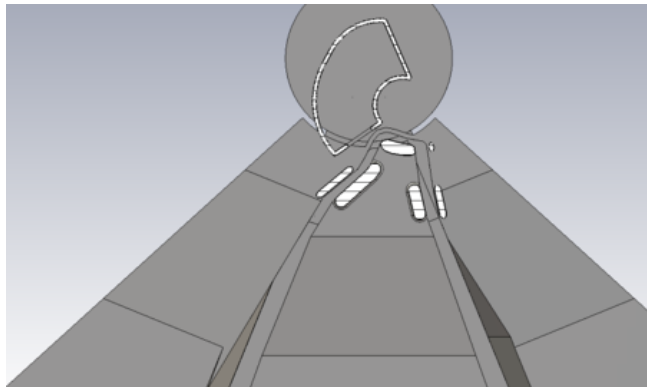


Figure 3.27: dees lofted transition top view

### 3.8.4 RF Cavities design optimization

#### 3.8.4.1 Performance requirement target

We have optimized the cavity geometry to ensure the following requirements:

- RF frequency of accelerating mode: 32.8 MHz
- Reference accelerating voltages: 65 kV at 80 mm (capture), 230 kV at 2000 mm (extraction)

The initial target value for the outer radius voltage was initially set at 250 kV, but according to our expertise, such high voltage will be very difficult to stand in cyclotron accelerator gaps of this size. It has been decided to reduce the target to 230 kV which remains a challenging value.

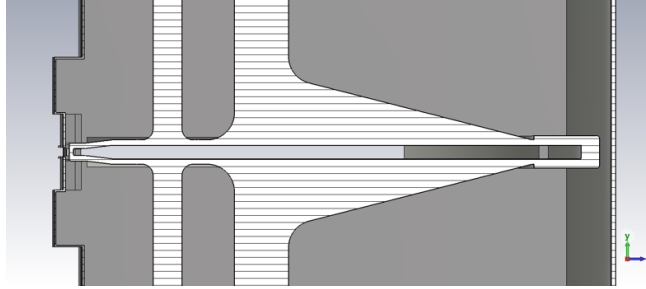


Figure 3.28: vertical gap evolution close view

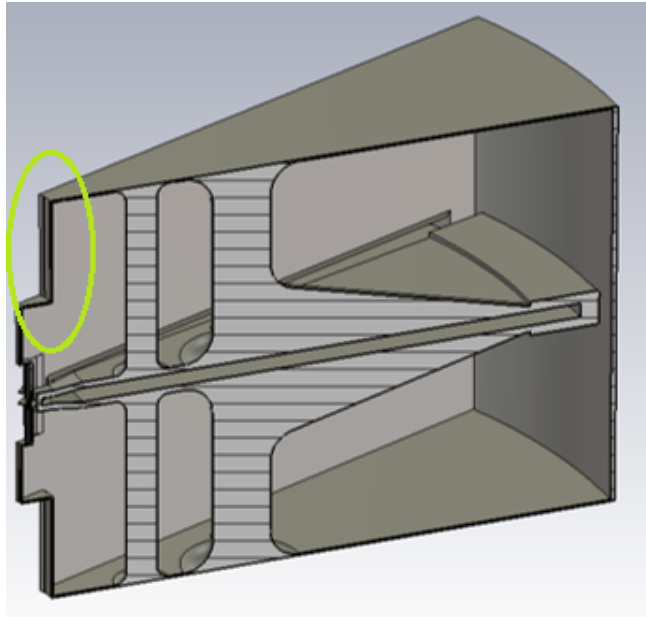


Figure 3.29: Clearance for RFQ

### 3.8.4.2 Parametric optimization of the design

We have intensively used parameters while building the CST model, to allow fast design exploration. We have retained four parameters to play with, for optimizing the cavity behavior. The parameters, shown at figure 3.31, are defined as a deviation from the early cavity design values.

- A: 1st pillar radial position
- B: 1st pillar diameter
- C: Deflector wall distance
- D: Deflector height

We did some initial exploration of the parameter space, but we did the final optimization using the built-in CST optimizer.

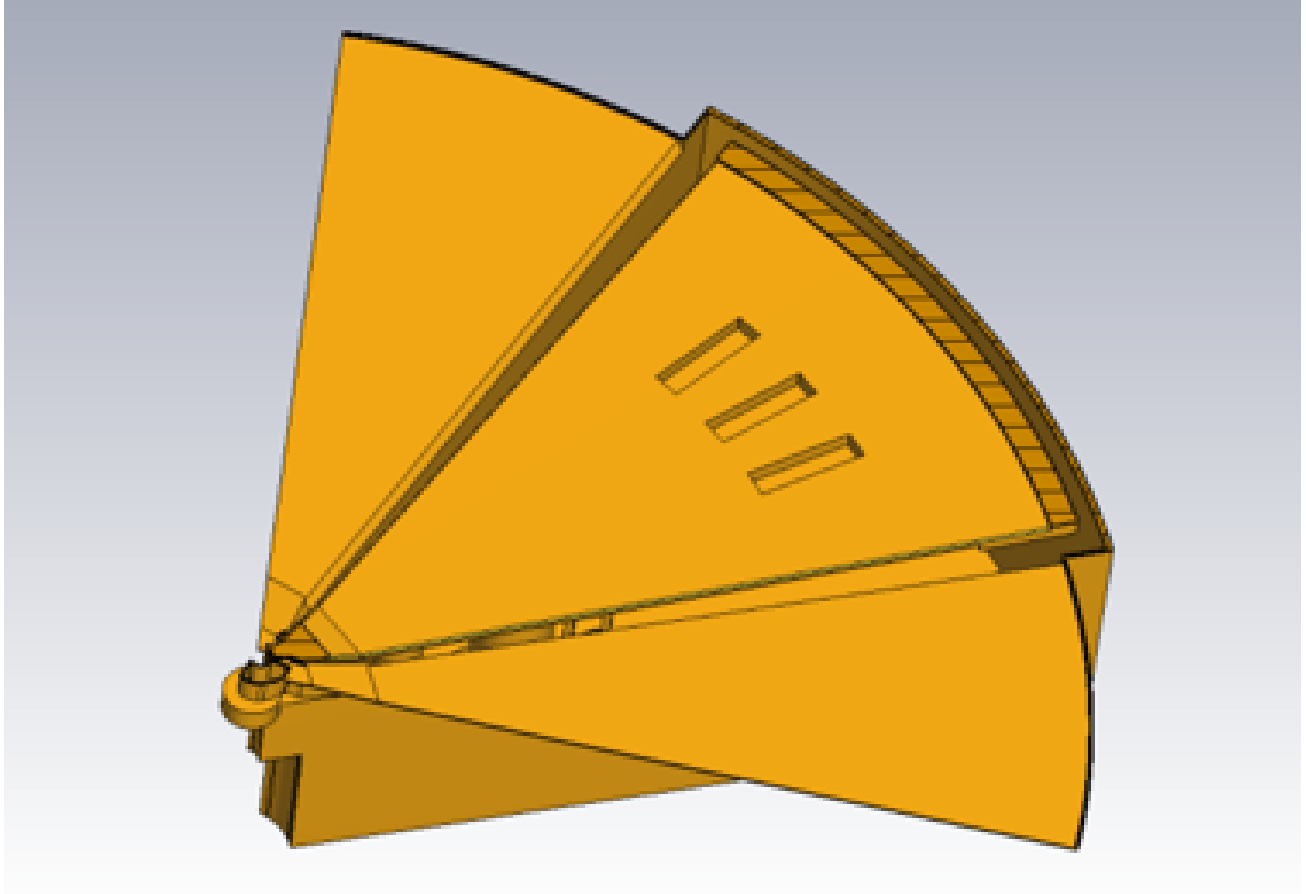


Figure 3.30: Provisional getter housings

We selected the trust region algorithm and have defined scaled goals that would ensure convergence toward the required frequency and voltages. The trust region algorithm converged in a few tens of iterations. The definition of the optimization goals, and their target and reached values are contained in table 3.7. The table 3.8 shows the optimal values reached by the optimizer.

### 3.8.5 RF cavity computation results

The RF cavity computation employing the eigen mode solver on the optimized geometry yielded the following performance and characteristics of the cyclotron system:

Table 3.7: RF cavities optimization goals definition and achieved values.

Goal description	Target	Final Value
Ratio between voltage at 80 mm and 2000mm	0.28	0.283
Model frequency [MHz]	32.8	32.805

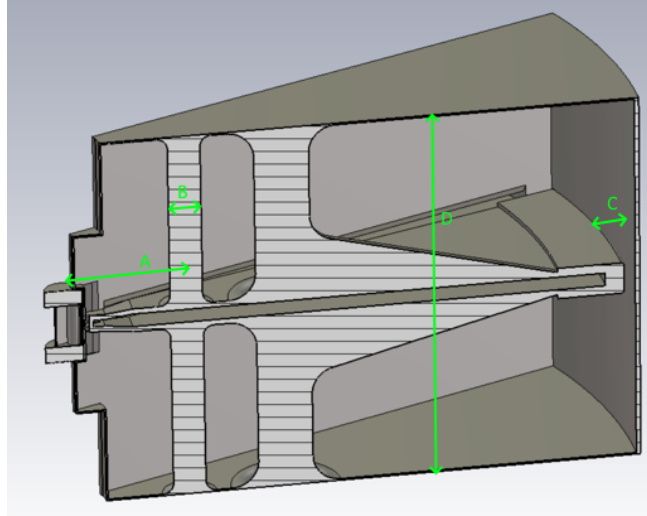


Figure 3.31: design optimization parameters

- **Frequency:** The RF cavity operates at a frequency of 32.805 MHz, ensuring compatibility with the designed acceleration, and the RFQ integration,
- **Voltage Ratio (center to outer radius):** The reached voltage ratio is 0.283, indicating that computed voltages at center would be 65.2 kV for a chosen voltage of 230 kV at the outer radius (2m),
- **CST computed quality factor (Q):** 10586,
- **Estimated quality factor (Q):** 7281,
- **Stored Energy (for max RF of 230 kV at 2 m):** 4.06 Joules
- **CST Computed Losses:** The computed losses per cavity using CST simulations are 79 kW,
- **Estimated Power Dissipation:** By experience, senior RF designers at IBA state that the CST eigenmode simulations underestimate the actual losses by up to 30%. If we increase the CST computed losses (79 kW) by this percentage, the actual estimated power dissipation per cavity becomes 113 kW.

Table 3.8: RF cavities optimized design parameters.

Design parameter	Value [mm]
First pillar radialposition (A)	444.6
First pillar diameter (B)	117.7
Distance between dee and cavity back wall (C)	42
Total cavity height (D)	1412

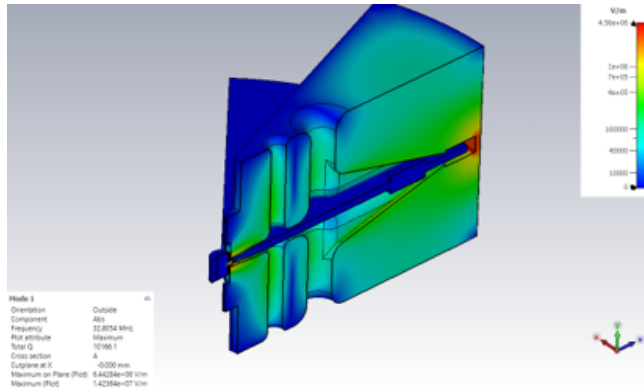


Figure 3.32: E field Vertical cross section

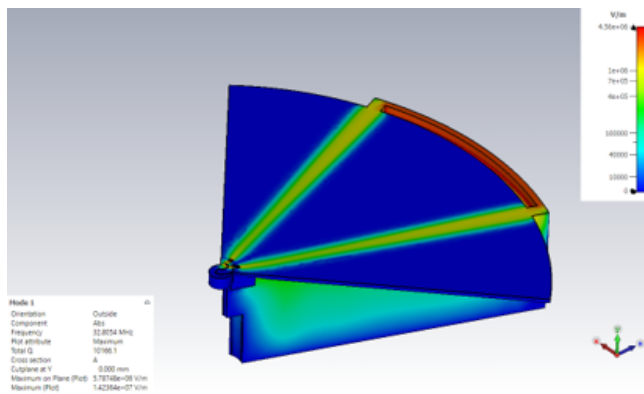


Figure 3.33: E-field Horizontal cross section

- **Estimated Power Requirement:** To effectively drive the cyclotron, each cavity will require an estimated power input of at least 263 kW, which include power dissipation and beam loading.
- **Maximal Surface Current:** The rms surface current reaches a maximum of 17052.6 A/m in some reduced locations. Which leads to a maximum surface power of 43.5 W/cm<sup>2</sup>. This maximal surface power is localized on the dee edges. Careful attention will be required for thermal management in these regions. For the rest of the surfaces, the thermal dissipation is well below 10 W/cm<sup>2</sup>. See figure 3.36 and 3.37 While matching the requirement, these computation results provide valuable information for next steps of the Cyclotron's RF cavity design including consideration in managing thermal effects.

Some illustrations of the electrical and magnetic fields computed by CST are given for reference at figures 3.32, 3.33, 3.34 and 3.35.

### 3.8.5.1 Detailed power analysis

We will now detail the post treatment of the CST results that lead to the results presented in Sec. 3.8.5. The CST eigenmode solver results are computed for a given reference energy in the



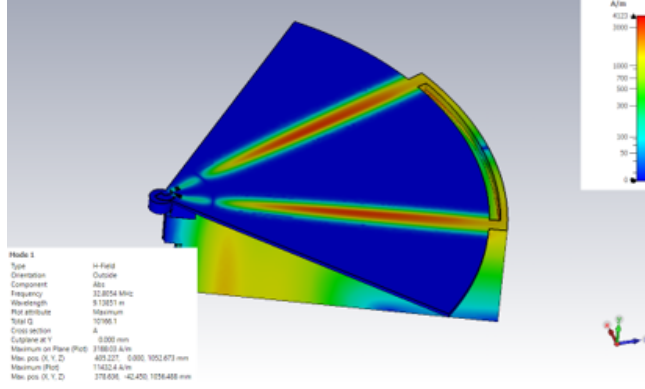


Figure 3.34: H-field horizontal cross section

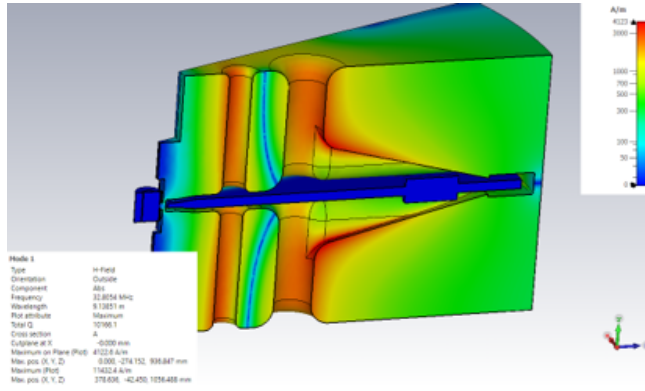


Figure 3.35: H-field vertical cross section

system (about 1J). They must then be scaled accordingly, to reach the expected voltage at a reference location. In our case, the reference location, is the orbit at 2m, and the desired voltage is 230 kV.

The ratio of the desired voltage to the reference voltage at 2m is 2.013. We can scale the currents and voltages using this factor. We can also scale the energies, power and losses using this factor squared (formulae 3.1, 3.2 and 3.3). We thus have:

$$E_{stored} = E_{stored,ref} \frac{V_{target}^2}{V_{ref}^2} \quad (3.1)$$

$$P_{loss} = P_{loss,ref} \frac{V_{target}^2}{V_{ref}^2} \quad (3.2)$$

$$I_s = I_{s,ref} \frac{V_{target}}{V_{ref}} \quad (3.3)$$

CST provides the maximal surface current  $I_s$  in the cavity which isn't a directly useful value, but we can compute from it the maximal surface power dissipation  $P_s$ , which will be useful

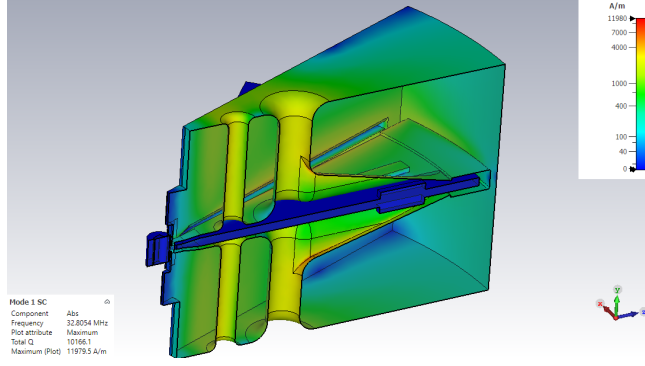


Figure 3.36: Surface currents

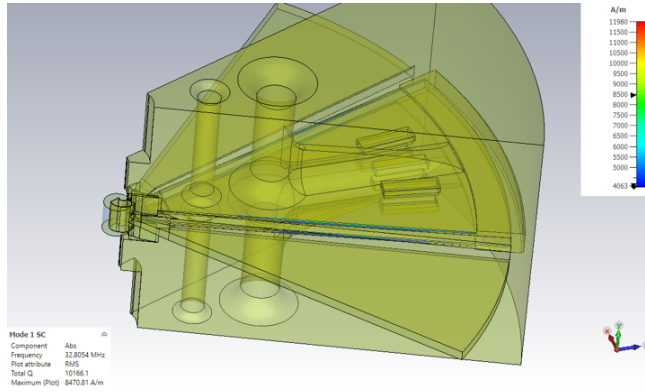


Figure 3.37: Surface current generating more than 10 W/cm<sup>2</sup>

for designing the cooling system sizing and layout. The physical properties needed for this determination are included in. We first need to compute the surface resistance  $R_s$  whose formula, given above uses the conductivity  $\sigma$  and the RF skin depth  $\delta$  (see formulae 3.4, 3.5 and 3.6). We end up with a maximal surface dissipation Power 43.5 W/cm<sup>2</sup>. This value, despite being high, only concerns the very small surface of the dee edges, and should not be considered as an issue for the design of the cooling system.

$$R_s = \frac{1}{\sigma \cdot \delta} \quad (3.4)$$

$$\delta = \sqrt{\frac{2}{\sigma \cdot \mu \cdot \omega}} \quad (3.5)$$

$$P_s = R_s I_s^2 \quad (3.6)$$

Table 3.9: Optimized cavities, functional characteristics.

	CST reference	Scaled value
Stored energy [J]	1	4.06
Voltage at on the 2m orbit [kV]	114.2	230
Voltage at center [kV]	32.4	65.2
Maximal voltage at outer edge of the dee [kV]	124.6	250.9
Computed losses [kW]	19.48	78.9
Maximal surface current [A/m]	8470	17052.6

Table 3.10: Cavity properties for computing surface dissipation

Property	Value
Copper magnetic permeability $\mu$	$0.99991 \times 4\pi \times 10^{-7}$ H/m
Copper conductivity $\sigma$	$5.8 \times 10^7$ S/m
Angular Frequency $\omega$	$2\pi \times 32.805 \times 10^6$ rad/s
Skin Depth $\delta$	11.5 $\mu$ m

### 3.8.5.2 Radial voltage dependency

The voltages at different radii have been calculated by integrating the electrical field along circular arcs crossing the acceleration gaps, and reference curves crossing central gap and the dee outer edge gap. The transit time factor has not been considered. The computed voltages have then been scaled to match a target voltage of 230 kV at 2 m. The resulting absolute and normalized voltage radial dependency are given in figure 3.38 and table 3.11

## 3.8.6 RF Tuning System

The tuning system is a movable plate that corrects the resonance frequency drift mainly caused by RF heating. The system here is based on four separated tuning plates (one per cavity) and located in the median plane. These plates are located at the back of the Dee and are controlled via a ball screw that is driven by a motor. This system is similar to that of many commercial cyclotrons.

## 3.8.7 RF Amplifiers

Traditionally a large part of the cyclotron RF budget is dedicated to the RF power source. This is especially true for this cyclotron, as it requires a high Dee voltage and accelerates 600 kW of beam power. This means that the total RF power exceeds 1 MW. Here we assume 1200 kW of RF power, which corresponds to a 50% efficiency of RF power to beam power. Since the four cavities are driven separately we are speaking about 4 distinct amplifier chains of 300 kW each.

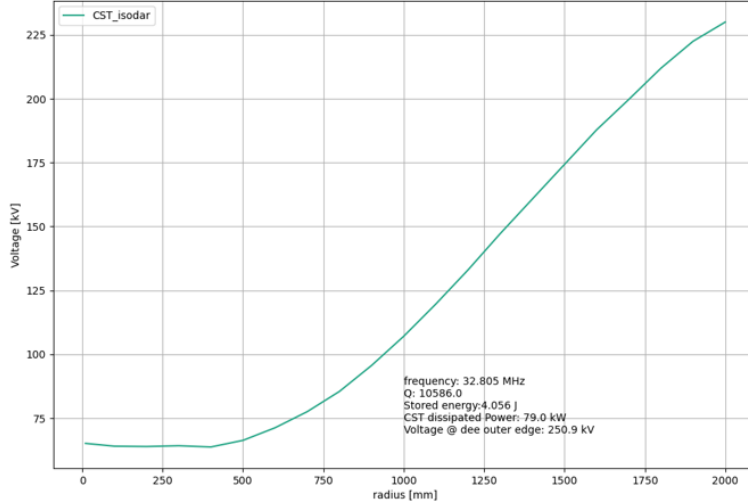


Figure 3.38: Dee voltage radial dependency

We plan to use vacuum tubes (triodes or tetrodes) to produce the RF power. We have considered using LDMOS amplifiers given the recent improvements in power density, reliability, and cost. However, we believe that vacuum tubes will perform better in the harsh environment and will be able to better accommodate the rapid variations in load due to the beam temporal patterns.

### 3.8.8 RF Lines and Couplers

The RF power is fed to the cavities through EIA 6 1/8" solid copper coax line. There are basically two ways to couple RF to the cavities:

- Capacitively in the median plane
- Inductively in the bottom (or top) of the cavity liner.

Both of these systems are capable of providing the necessary 300 kW power to each cavity. Capacitive coupling is less prone to multipacting because the coupling antenna could be easily DC biased. But, our expertise in high power coupler design advocates for an inductive solution. The design of inductive coupler is easier to water-cool, and there is a wide area where H-field is high enough for efficient coupling behind the second pillar of the cavity.

We have initiated a preliminary design computation of such an inductance coupler, feeding the RF power from a EIA 6" 1/8 port. The suggested design is a loop made out of a 20x60 mm rectangular section bar, offering room for water-cooling. See figure 3.39. The adaptation tuning will be performed by rotation of the loop around the vertical axis. The design has been optimized with a default angle of 45° to the cavity axis, in order to allow a maximal tuning range.

Table 3.11: RF voltage radial dependency.

Radius [mm]	Voltage [kV]
Capture (80)	65.17
100	64.07
200	63.95
300	64.60
400	63.76
500	66.37
600	71.30
700	77.60
800	85.50
900	95.67
1000	107.09
1100	119.72
1200	133.04
1300	147.22
1400	160.77
1500	174.31
1600	187.84
1700	199.73
1800	211.94
1900	222.49
Extraction (2000)	230.00
back of dee	250.91

The optimization of the coupler loop, for a cavity loaded with 150 kW of beam leads to an height of 235 mm, which provides a good matching (figure 3.40) and a  $S_{1,1}$  computed scattering parameter inferior to -60 dB.

### 3.8.9 LLRF Electronics

The LLRF (Low Level RF) controls the RF amplitude and phase of the signal sent to the amplifiers. It also controls the tuning mechanism in order to maintain the resonant frequencies in the cavities. The amplitude and phase control is based on feed-back signals coming from the cavities and amplifiers. In order to avoid multipactoring, the LLRF manages also a pulsing mode that provides for an easy start-up and reduces the power dissipated in the amplifiers. One LLRF system per cavity is planned.

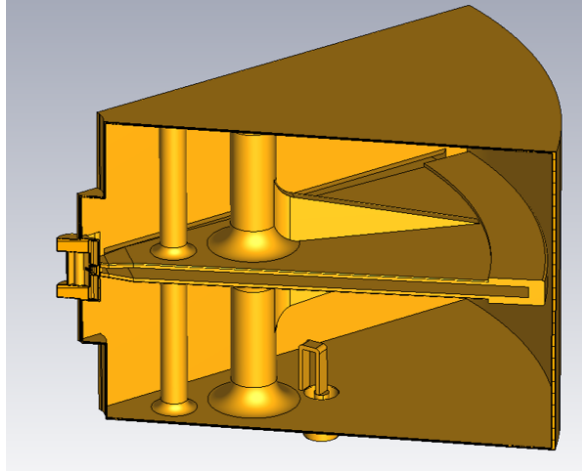


Figure 3.39: RF loop coupler design

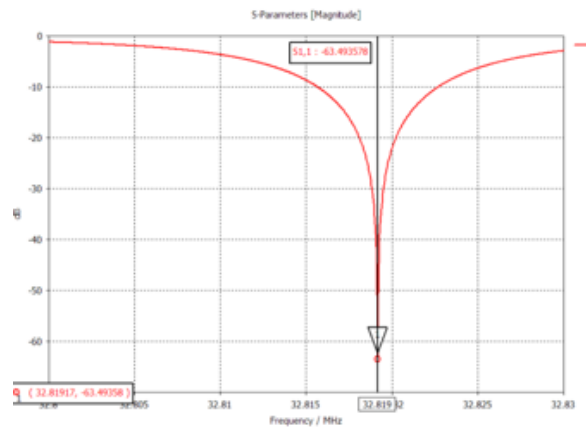


Figure 3.40: Coupler port impedance

An additional electronic element is needed to keep a stable phase difference between the different cavities.

### 3.8.10 Risks and Mitigation

**Risk: Design and Manufacturing Process.** The Q factor and eigenfrequency depend on the manufacturing process of the RF Cavity, e.g., surface quality and material purity. Furthermore, there is a risk of multipactoring during run-time as electrons can be accelerated back and forth in the RF field.

**Mitigation:** A 30% margin was built into the RF power estimates, based on operational experience by IBA. An appropriate tuning range is built into the cavity design. A full scale RF cavity will be built and tested before the start of the construction of the other three cavities. Options of cavity coating exist in case of multipactoring, e.g., Aquadag.

## 3.9 Cyclotron Particle Simulations

It is necessary to perform an in-depth particle simulation of the primary acceleration of the beam to ensure that the beam reaches energy, maintains quality, and is possible to extract. We do this using OPAL [49] which is a particle accelerator simulation suite developed at the Paul Scherrer Institute that accounts for space-charge effects. It is based on particle-in-cell (PIC) calculations that track a 'bunch' of particles through time-varying magnetic and electric fields. The temporal integration within OPAL is carried out using a fourth-order Runge-Kutta method. There is a mode within OPAL, OPAL-cycl, which is designed to simulate cyclotrons. This makes it well-suited for the primary acceleration phase of the IsoDAR cyclotron. Conveniently, OPAL-cycl has built-in objects called PROBES, that can provide beam diagnostics, and COLLIMATORS, which can provide halo reduction.

### 3.9.1 Fieldmaps

A critical aspect of these simulations is that they accurately simulate the electric and magnetic fields within the cyclotron. We performed these simulations using a 1D RF model derived from the voltages provided in Table 3.11. The radially increasing voltage leads to a roughly constant turn separation, which is important for ease of extraction. We conducted these simulations using a 2D median plane magnetic field that is derived from a physically realistic cyclotron model produced by IBA. Of note, this magnetic field map does not include a  $\nu_r = 1$  resonance, which would increase the inter-turn separation in the last few turns at the price of reduced beam quality. This magnetic field is significantly more realistic than our previous work because the cyclotron model allots space for the injection components.

### 3.9.2 Probes

Probes are a built-in OPAL object that records whenever a particle passes through the region defined by the probe. These particles are simply recorded, and the trajectories of the particles are not affected by their intersection with the probe. This is helpful for determining the “extractability” of the beam. The probe collects information about the position and the momenta of the passing particles. By placing a probe at an azimuth of 25 degrees, the angle at which our electrostatic channel starts, we are able to determine the overlap between sequential turns of the beam path. This is necessary because we want to minimize this overlap for ease of extraction. The overlap between beams provides a lower bound for the power that will be deposited on the electrostatic septum, so we aim to minimize this value. The data from the probe is displayed in Fig 3.42.

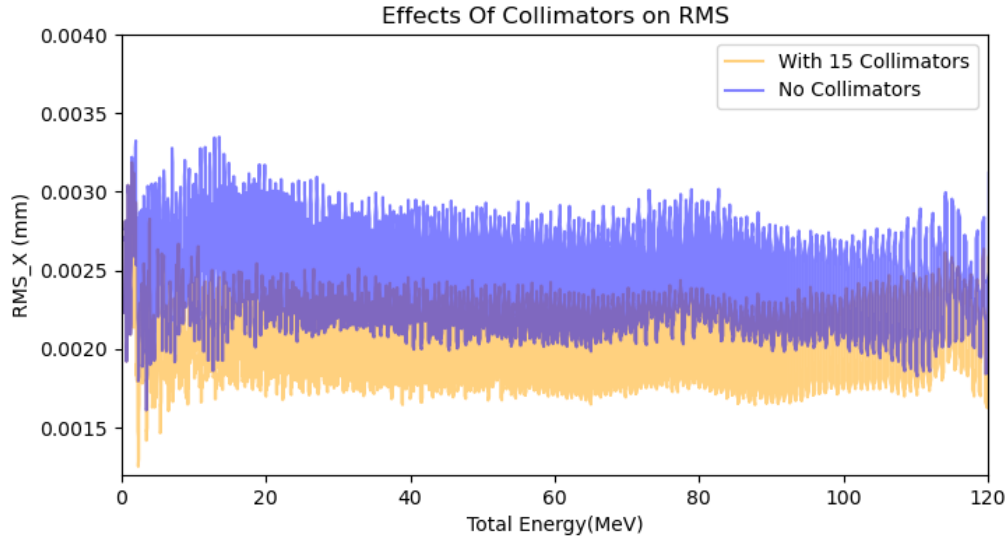


Figure 3.41: The collimated beam had a much reduced radial RMS spread.

### 3.9.3 Simulation Results

Using the field maps as discussed earlier and the set of 15 collimators as described in the previous sections. We are able to smoothly accelerate the beam up to 60 MeV/amu as shown in Fig 3.43. Additionally, there is minimal growth in beam size in the collimated beam as shown in Fig 3.41. Additionally, a probe at an azimuth of 25 degrees sets a lower limit for extraction at 120W as seen in Fig 3.42.

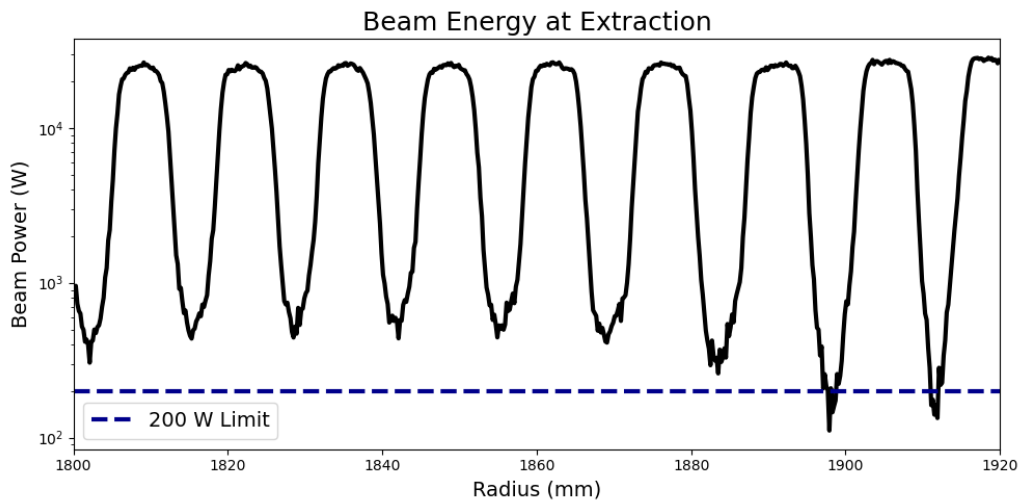


Figure 3.42: There are two potential extraction points



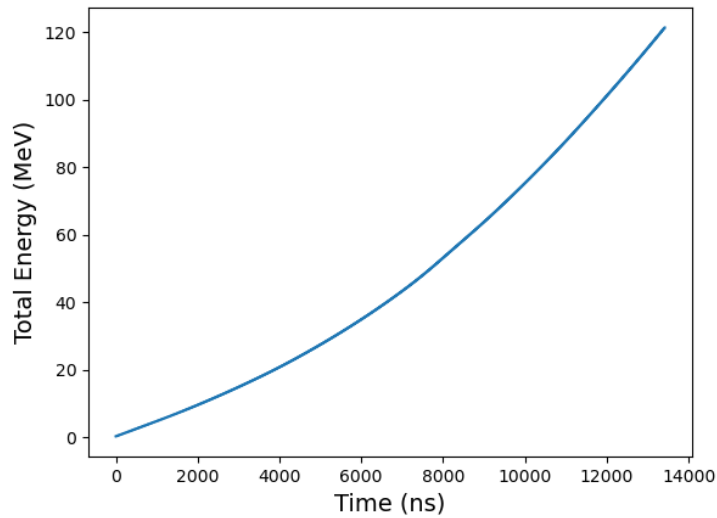


Figure 3.43: There is a smooth acceleration of the beam

### 3.9.4 Electrostatic Extraction Channels

The first step in our extraction is the construction of a radially directed electric field that peels the last turn away from the second to last turn. This is done by placing a series of thin (0.2 mm) grounded electrodes between the last two turns and a larger puller electrode that is at high negative potential outside of the last turn. This generates a well-shielded electric field in the region between the puller and septum. A rendering of the electrostatic septum is shown in Fig 3.44. There are two such electrostatic channels that increase separation between the last two turns.

We determine the exact location of each element of the extraction channel iteratively. The first

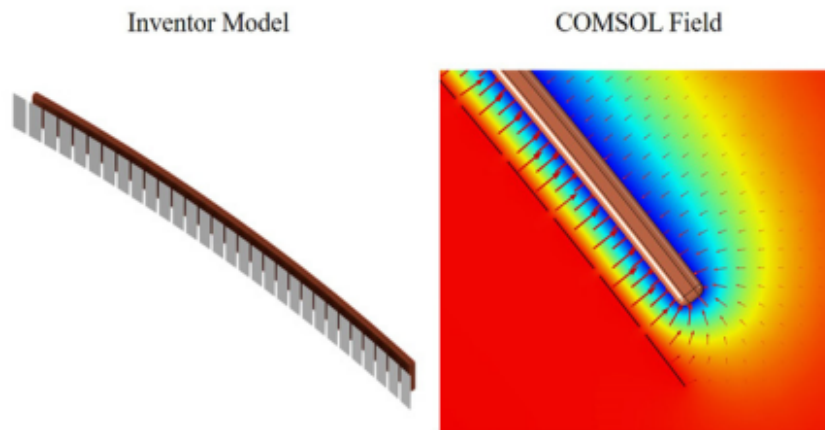


Figure 3.44: CAD rendering of electrostatic septum. From Ref. [28]

step is to run a Python script on a pre-existing OPAL simulation of the last three turns that determines the initial positions of the septum and the puller. We choose to place the septum evenly between the last two turns. A .txt file is generated that allows for a model of the septum to be built in Autodesk Inventor. With this geometry, we use COMSOL to determine the electric field and add it to the pre-existing RF field of the cyclotron in OPAL. We model the physical dimensions of the septum as COLLIMATOR objects in OPAL. This process is repeated twice at which point further iteration does not result in any improvements in ESC performance. Following this we were able to reduce our losses on the first septum to 205 W which is 2.5% greater than our 200 W goal and we lose 21 W on the second septum. In the future we plan to reintroduce a resonance into the magnetic field which will increase the inter-turn separation at extraction which will greatly reduce this number. The end result of the septum optimization process is shown in Fig 3.45.

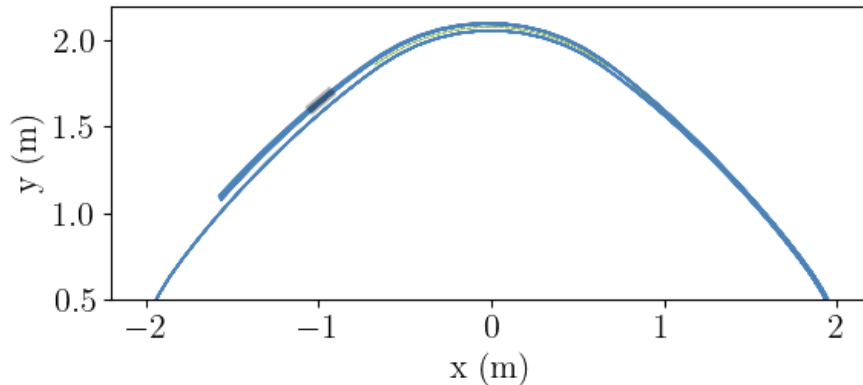


Figure 3.45: This is the tracking of 100 particles as they pass through the electrostatic channels (shown in green). It also shows the location of our magnetic extraction channel in grey.

### 3.9.5 Magnetic Extraction Channels

After the electrostatic extraction channels, the beam will rapidly de-focus as it passes through the radially decreasing magnetic field. In order to avoid this issue, we must include focusing elements that can counteract the effects of the fringe fields of the cyclotron. Due to space constraints, it is not possible to have an active element such as a quadrupole within the cyclotron. Instead, we will use the standard strategy of machining and placing iron bars along the extracted beam path. These bars allow us to locally reshape the magnetic field and are very compact. We model our magnetic extraction off of the MSU cyclotron [64] which generates a strong radially increasing magnetic field that serves to refocus the beam after the ESC. By using the gradients that are produced at MSU as a reference point, we conservatively set a gradient of 1.5 kG/cm which is much less than the 5 kG/cm that they were able to achieve. We directly modified our magnetic field to contain these elements. It is visible in Fig 3.46 that a fairly weak magnetic channel is sufficient to maintain beam quality. We do not anticipate difficulties with these channels because the electrostatic channels generate the majority of the turn separation.

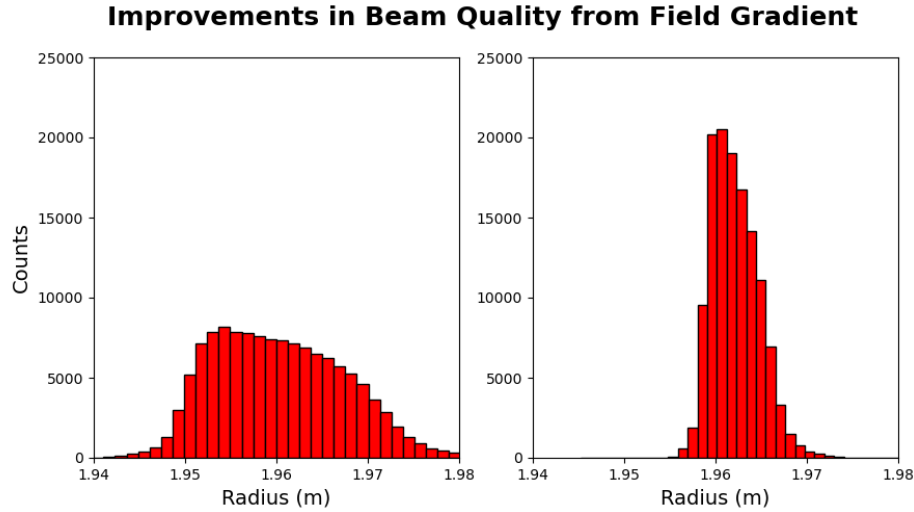


Figure 3.46: A 1.5 kG/cm gradient after the electrostatic channel dramatically reduces radial beam spread

### 3.9.6 Risks and Mitigation

**Risk: Inadequate turn separation.** If beam bunches are not radially separated by a sufficient amount, unacceptable beam loss will occur on the thin septum rendering its lifetime to be inadequately short.

*Mitigation:* Understanding beam dynamics sufficiently well that this does not happen, and having adequate beam diagnostics to be able to tune the beam for maximum turn separation. Further, we could place a narrow carbon foil in front of the septum, dissociating the few  $H_2^+$  ions that would otherwise hit the septum. The resulting protons have lower magnetic rigidity and bend away from the septum before hitting it. They follow a specific trajectory that can guide them outside the cyclotron to be dumped in a controlled way.

**Risk: Placement of the narrow stripping foil.** It is not obvious where the optimum location is for the thin stripper. It must be such that stripped protons do not strike the septum, but also that halo particles do not miss the stripper and strike the septum.

*Mitigation:* Adequate beam dynamics simulations, including tracing of particle orbits.

# Chapter 4

## Installation in the Yemilab Setting

The most likely deployment location for IsoDAR is at the Yemilab underground laboratory, 1 km below the surface adjacent to the Handuk iron mine in the Republic of Korea. Fig. 4.1 schematically shows Yemilab, accessed either by a 6 km meter ramp descending 750 meters at a 15% slope from a surface access point into the mine, or by an elevator which descends down a 600 meter vertical shaft. Unfortunately, the elevator is suitable only for personnel access. All heavy and bulky equipment must be brought down via the ramp. Fig. 4.2 details the area where the IsoDAR experiment would be installed, with the target only a few meters from the planned 3 kiloton LSC (Liquid Scintillator Counter). The following section provides a general description of deployment strategies in an underground setting, pertaining only to the cyclotron. In this document we use Yemilab as the example, noting that most of the issues discussed will arise in an equivalent manner at any alternative installation sites. A similar approach will be taken for the target system in Volume II of this PDR.

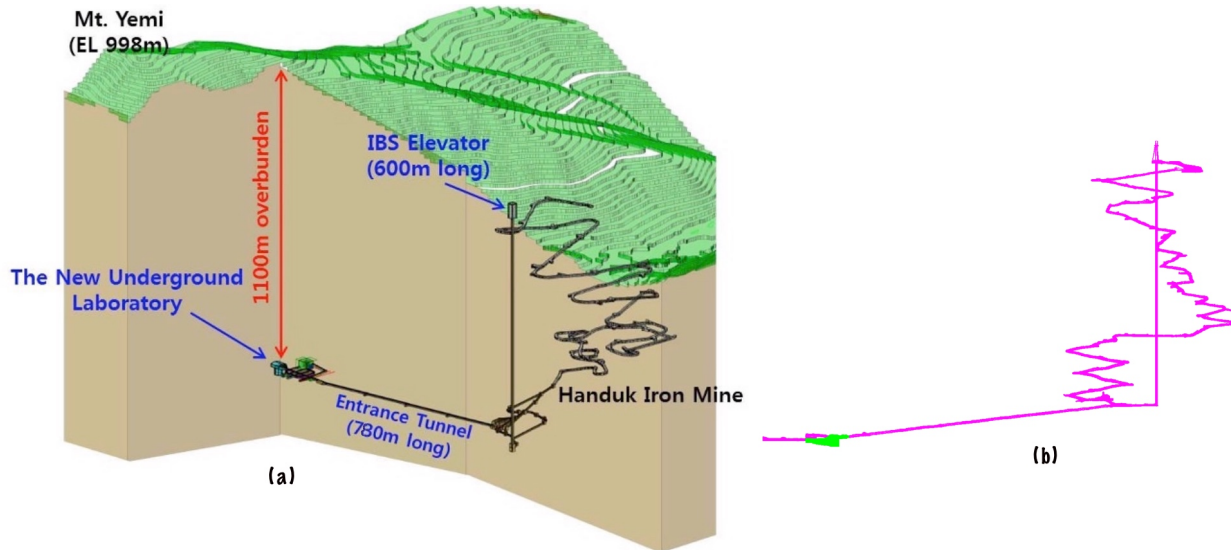


Figure 4.1: (a) Schematic of Handuk/Yemilab area, (b) Low resolution laser scan of Handuk mine and Yemilab access ramps, green area denotes high resolution scans of IsoDAR deployment area, shown in more detail in the next figure. From Ref. [65].

## ❖ Yemilab Layout (Top view)

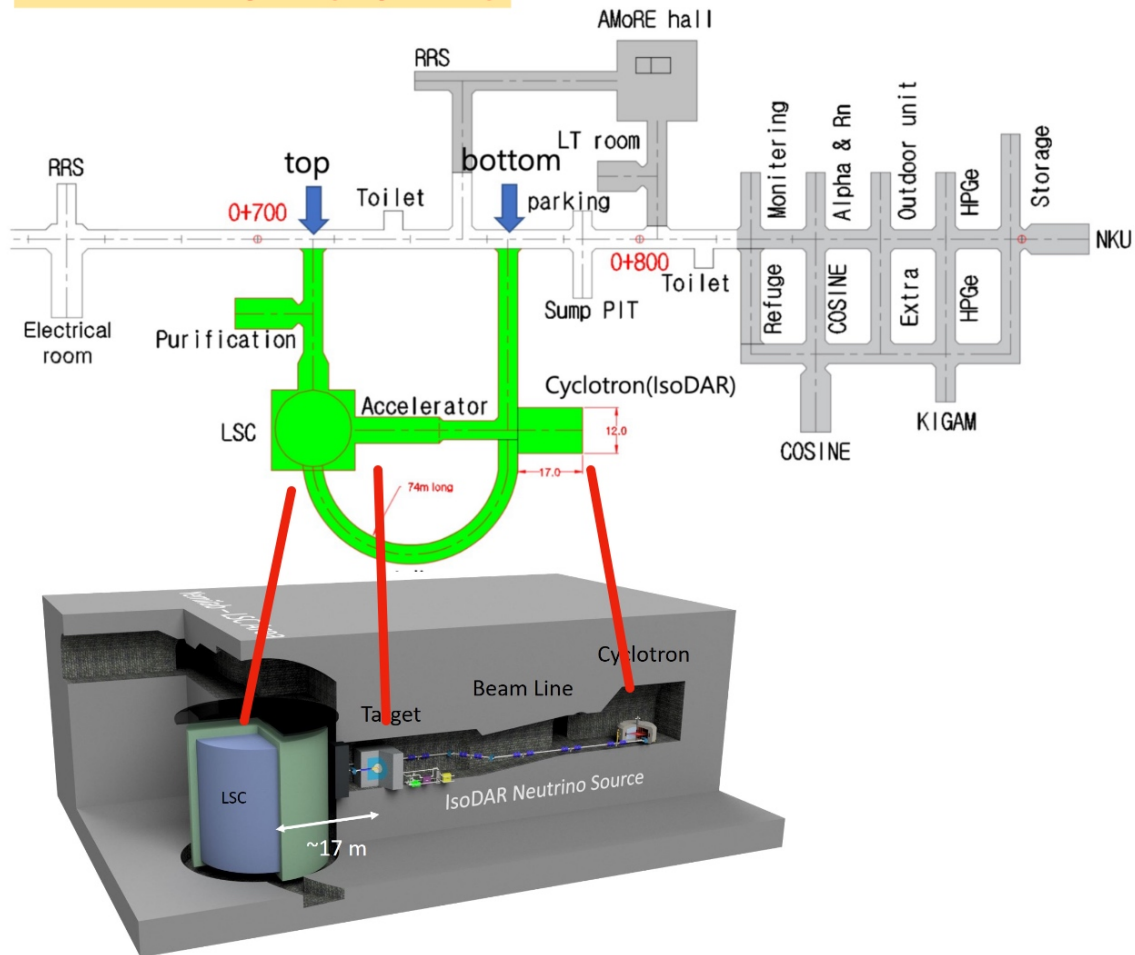


Figure 4.2: Layout of Yemilab, showing (in green) the area where IsoDAR will be installed. The cyclotron will be assembled in the dedicated cyclotron vault as shown.

## 4.1 Transport of Components

All of the components of the experiment must be brought to the site from the port-of-entry into the Republic of Korea. The preferred method is to use trucks along the highways. Prior experience of IBA with rail transport has been that it is difficult to provide adequate shock protection, and heavy pieces can be damaged in transit. As stated above, transport from the surface to the experimental site must be accomplished by way of the mine ramp depicted in Fig. 4.1. Nominally, its cross section is 5 x 5 meters, however we are told that pinch points and sharp bends may occur and might provide challenging areas to transport large, heavy loads through. We have received assurance that large mining trucks, 3.5 meters wide, can traverse the entire ramp, as this is the way ore was transported to the surface for many years.

While high-resolution laser scans of the IsoDAR and LSC areas have been performed, (cf. Figures 4.8 and 4.9), the resolution of the laser scans of the access ramp areas are not of sufficient

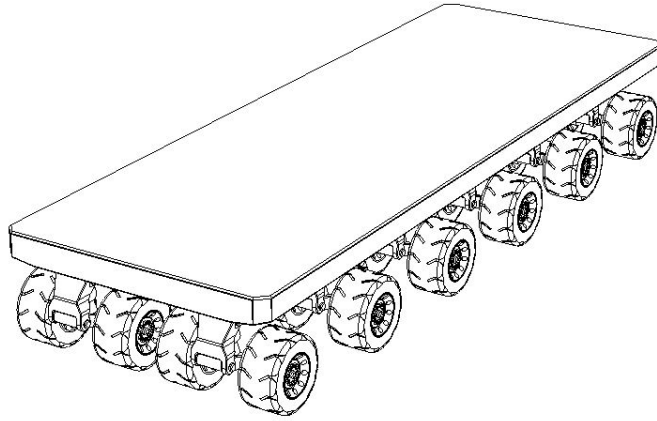


Figure 4.3: A typical SPMT vehicle, a versatile way to transport heavy loads over irregular terrain.

resolution to provide enough detailed information about the location or size of the possible constrictions. Improved scans must be performed as part of final installation planning in the Technical Design Report phase (TDR).

As seen in the previous chapter, the iron pieces that make up the cyclotron magnet, although heavy, are not in themselves large, so the pinch points are not likely to be a problem for bringing the magnet steel to the installation site. The plan is to use an SPMT vehicle (Self-Propelled Modular Transporter) shown in Fig. 4.3 for bringing the magnet and vacuum liner pieces from the surface. These electrically-powered vehicles are flexible in their size, the sets of 4 tires are independently steerable, so the vehicle is extremely maneuverable, and can easily accommodate the heaviest piece of magnet steel [66].

The only challenge will be the magnet coils. Each of the two coil packages measures 5 meters across and 0.3 meters high, the individual coils inside measure 4.960 x 0.252 meters. Figs. 4.4 and 4.5 gives an approximate view of a coil package and the clearances in the access ramp to the Laboratory (marked as the "Entrance Tunnel" in Fig. 4.1 (a)). This particular ramp is well-constructed and engineered, and has a measured width of 5 meters. A special mounting fixture capable of holding the coil packages at an angle should be able to bring these coils through this particular passageway. There are constrictions even in this ramp: cable trays and service boxes, however these can be moved if necessary. Uncertainty remains as to whether this type of conveyance device for the coils can navigate the winding ramp from the surface.

In the unlikely case the individual pancakes do not fit through the constriction points, the alternative is to wind and pot the coils underground, or make them in sections. This has already been studied in Chapter 3 of the CDR document [2], [67]. The heavy winding machine and fixtures would need to be transported, but could be broken down into parts that will fit through the ramps, then assembled on site. The biggest challenge would be the ventilation scheme for the potting process. There is precedence for sectioned coils. For the large TRIUMF cyclotron [68], coils are separated into six different segments as the outer diameter of the coils

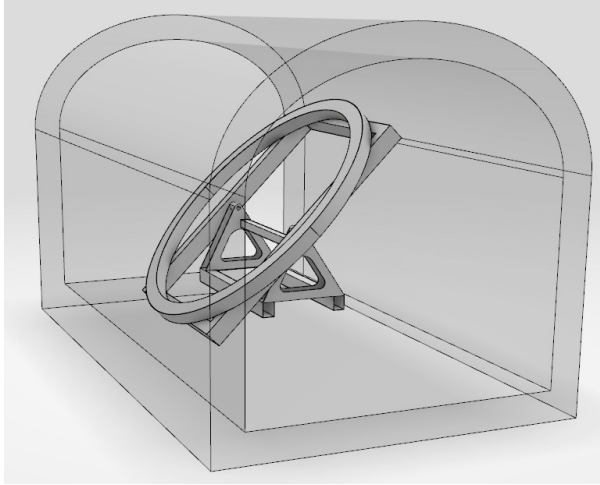


Figure 4.4: Isometric view of the coil package, on a specially-designed cart, transporting the coil through the access ramp to the Yemilab campus.

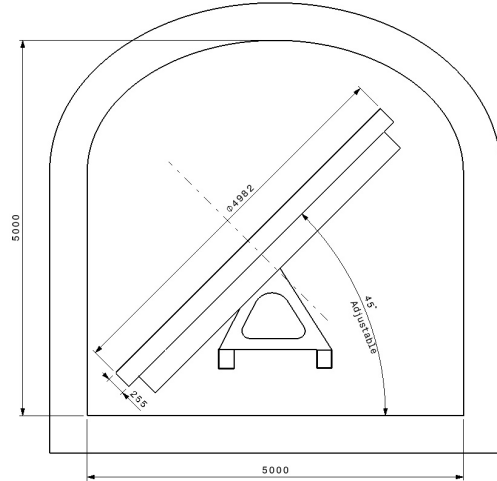


Figure 4.5: This ramp is engineered to a 5-meter width, and maximum height of 5 meters. Unfortunately we do not have sufficient information about the winding access ramp from the surface to the base of the shaft to assess at this time whether transport of the coils will be possible with this conveyance device.

is almost 20 meters, making the transport of fully assembled coils essentially impossible over conventional roadways. The inconvenience for a segmented coil, is that the ends of every turn of every section must be spliced, substantially increasing the cost and decreasing the efficiency of operation, as the coil must have as few turns as possible with very high current flowing through each turn.

## 4.2 Assembly underground

The cyclotron will be assembled in a hall measuring 12 meters wide, 17 meters deep and 10 meters high. This hall was excavated to our specifications at the 90 degree bend in the access ramp to the LSC, as seen in Fig. 4.2. A flat area, roughly 10 m x 5 m at the corner will be the staging area for components transported from the surface. A bridge crane riding on tracks will be used to rig parts to the cyclotron assembly point. Conversations with a crane manufacturer, Industrias Electromecánicas GH, S.A. [69] gave us assurances that a 40-ton capacity crane, riding on rails installed on the cavern floor would be quite practical (see Fig. 4.6. It could be configured to fit the dimensions of the cavern, and broken into modular parts that could be transported to the site.

An overview of the cyclotron inside the cavern with the rigging equipment is shown in Figures 4.7 - 4.9. It should be noted that the gantry crane will be dismantled once the heavy parts



Figure 4.6: Examples of GH gantry cranes, capacities: foreground 20 tons, background 260 tons. From Ref. [69].

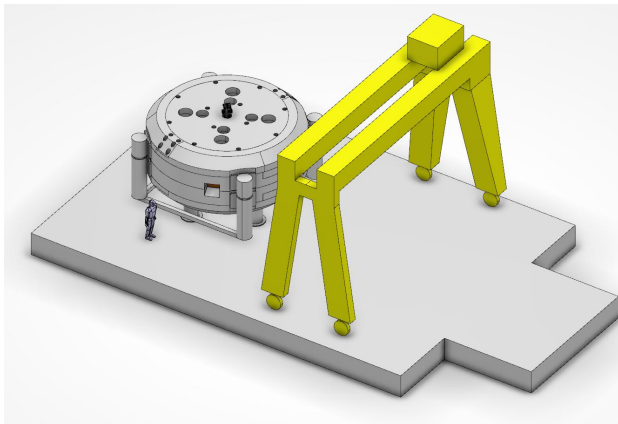


Figure 4.7: Cyclotron and crane on cavern floor.

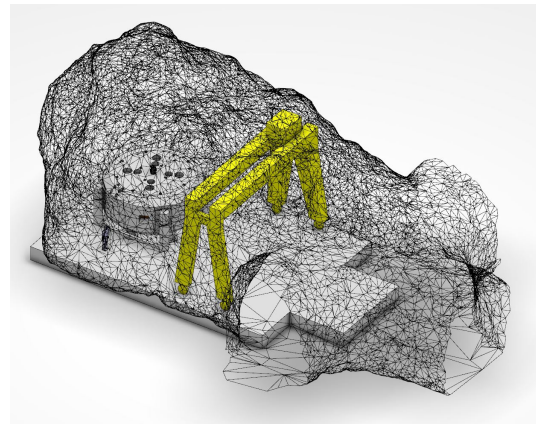


Figure 4.8: Cyclotron and crane inside the cavern.

are rigged. This would increase the clearance above the cyclotron for the additional equipment. In addition, the large crane can be reconfigured and reassembled in the target hall, and used for assembly of the MEBT, target and shielding, and for subsequent maintenance of the target systems.



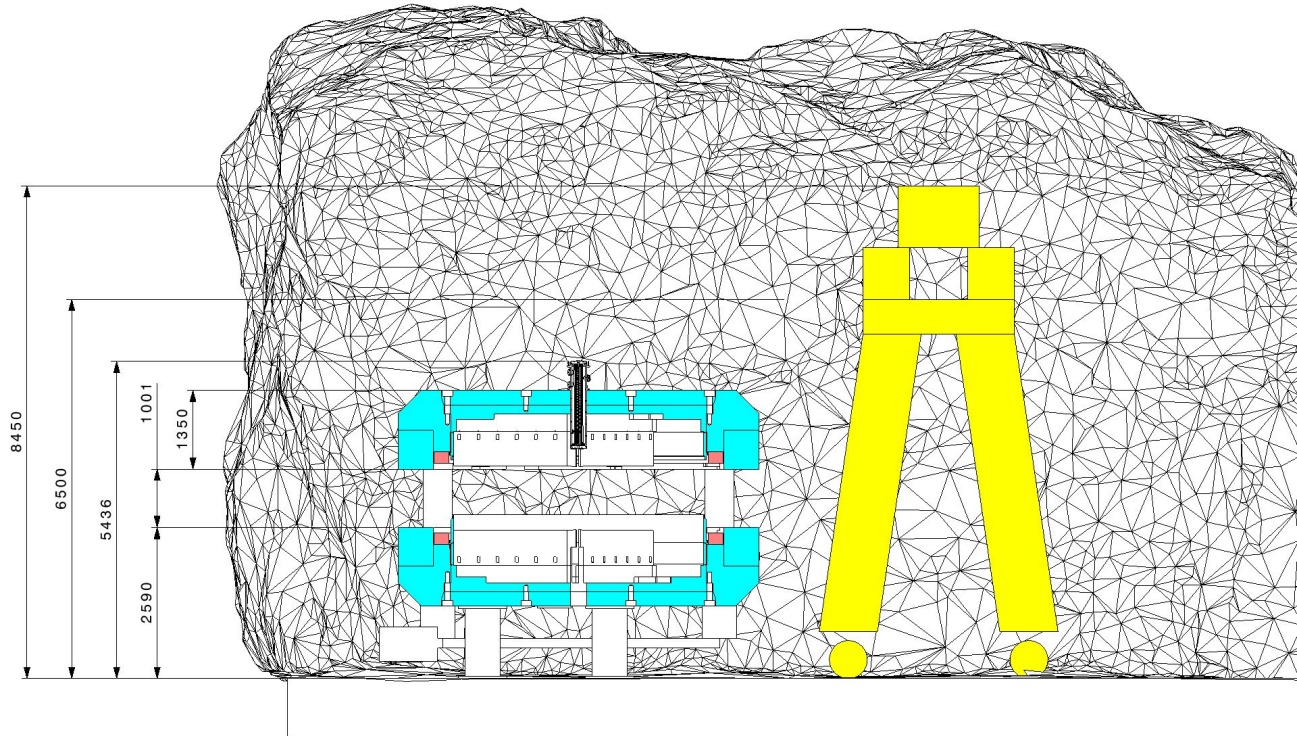


Figure 4.9: Cyclotron open and crane with cavern mesh - cut-view.

## 4.2.1 Risks and Mitigations

**Risk: Coil Size.** The cyclotron coil will likely not fit through all of the sections of the main access ramp at Yemilab in horizontal orientation. A special mounting fixture capable of holding the coil packages at an angle should be able to bring these coils through diagonally. However, there is some uncertainty about possible choke points in the main access ramp to the Yemilab facility.

**Mitigation:** *In the unlikely case the individual pancakes do not fit through the constriction points, the alternative is to wind and pot the coils underground, or make them in sections, as discussed above. Both come with drawbacks or additional cost, but are manageable.*

# Chapter 5

## Conclusion

### 5.1 Summary

In this version 2.0 of the document, we presented the preliminary design of the IsoDAR compact cyclotron with RFQ direct injection, including ion source, low energy beam transport, electrostatic extraction channels and some thoughts on typical magnetic extraction channels. This version presents significant updates over the previously published CDR and also version 0.9 of this PDR. Most notably, we included first information about the upgraded MIST-2 ion source, a much optimized spiral inflector, a realistic cyclotron magnet and RF cavity design and particle-in-cell simulations thereof. Over version 0.9 of this document, we added detailed subsections on the simulations and subsections on risks associated with the different components as well as mitigation strategies.

The presented design study shows the feasibility of producing a high CW  $H_2^+$  beam current (10 mA of protons through stripping of a 5 mA  $H_2^+$  beam) in a compact cyclotron. It further shows a convincing strategy to segment the cyclotron yoke for transportation into the underground environment to be assembled in situ at the final location. Below, we summarize our designs and findings for the different subsystems (ion source and LEPT, RFQ, cyclotron, underground installation).

#### 5.1.1 Ion Source and LEPT Summary

Based on literature and in-depth simulations using well-established codes, we have determined that a filament-driven multicusp ion source presents an attractive solution to producing 10-12 mA of DC  $H_2^+$  beam current with high purity and low emittance. The filament lifetime is the main drawback. We presented our design and measurements with such an ion source using our own MIST-1 prototype and first tests of the upgraded MIST-2 components. Our measurements agree extremely well with simulations and, although we have only reached about half of the design current with the MIST-1 prototype, we are confident that we have addressed all the “lessons learned” from it in our MIST-2 design and foresee no showstoppers in achieving the needed beam current with it. We estimate the filament lifetime to be about a week of continuous running, which would let us achieve the required 90% up-time. As a fallback, flat-field ECR ion sources are a tried-and-tested alternative, albeit with the (manageable) caveats of co-producing significant amounts of protons and having a higher emittance.

The LEBT is a straightforward, highly compact design that includes safety mechanisms, beam positioning, and beam diagnostics. Our simulations include robustness tests and failure-mode simulations showing its capability to handle these. The beam is well matched into the RFQ. Parts of the LEBT have been manufactured with the remainder to be delivered at the same time as the RFQ. Experimental verification is thus forthcoming.

### 5.1.2 RFQ Summary

Here and through references to published papers, we presented the technical design of a split-coaxial RFQ of 28 cm diameter, operating at a frequency of 32.8 MHz (matched to the cyclotron frequency). The design includes thermal and mechanical vibration studies and full 3D PIC beam dynamics calculations including all fringe fields, using the LEBT output as input beam.

The RFQ is currently being manufactured by Bevatech, GmbH in Germany. An experimental campaign has been started to put together ion source, LEBT and RFQ, and ultimately a 1.5 MeV/amu test cyclotron (the HCHC-1.5) for the ultimate demonstration of  $H_2^+$  acceleration, RFQ direct injection, and establishment of vortex motion.

### 5.1.3 Cyclotron Design Summary

We presented a realistic cyclotron mechanical and electrical design consisting of the main magnet, the RF Cavities, and vacuum chamber. The magnetic and electric fields calculated from these models by FEM and BEM were used to perform highly realistic PIC simulations using the OPAL code.

Simulations merging the RFQ output with the spiral inflector in the central region have now also been performed; completing a simulation chain running seamlessly from initial plasma generation in the ion source into the central region of the cyclotron where acceleration will begin. Simulations of the acceleration beginning with the end of the central region and concluding with extraction at the target energy of 60 MeV/amu have been performed using an input beam that was informed by a standalone central region design. Connecting the latest spiral inflector simulations with a modified version of this central region inside the new magnet model will yield a full start-to-end simulation of the IsoDAR experiment.

This section also discussed several improvements that have been explored to increase the efficiency, safety, and beam quality that emerges from the inflector into the cyclotron.

Calculations performed with the full 3D model of the RF cavity showed manageable power and cooling. The required radial voltage distribution in the accelerating gaps, and adequate room for vacuum getter pumps.

### 5.1.4 Installation Summary

We described the layout of the Yemilab facility and how to transport the cyclotron steel components using SPMTs. In the cyclotron cavern, assembly will be aided by a gantry crane that can be disassembled after cyclotron installation to make room for the peripheral devices.

We identified the main risk as the cyclotron coil size being on the edge of what can be transported through the main access ramp at Yemilab. A careful investigation of possible choke points is needed for the TDR. Possible mitigation is to wind the coil in place or to adopt a split coil design as we described in the CDR.

For the next level of detail, we are working hand in hand with colleagues from Yemilab to identify further issues, devise an installation and removal plan, as well as overall integration plans with the facility (power, HVAC, controls, etc.).

## 5.2 Outlook

A future Technical Design Report will have to include a number of additional details, among them a full start-to-end simulation using as few beam dynamics codes as possible, benchmarked against a second set of codes; robustness analysis; a vacuum calculation (most likely using the CERN-developed code MolFlow); specifics of assembly and removal as well as shielding of the cyclotron cavern; RF system details; a commissioning strategy; data acquisition for beam diagnostics; and the cyclotron control system.

We have investigated a number of these topics and published results thereon, but including them here would have gone beyond the level of a PDR. Others are current and ongoing studies and publications are forthcoming (well before the final TDR, much like we did here).

Most notably, we are in the process of putting together the RFQ-Direct Injection Project (RFQ-DIP), combining the MIST-2 ion source (currently commissioning), the RFQ (currently being machined), and the HCHC-1.5 cyclotron (parts being ordered), as demonstrator of all novel concepts in the HCHC-60 cyclotron design.

## 5.3 Acknowledgements

This work was primarily supported by NSF grant PHY-2012897. Preliminary work leading up to this was supported by NSF grants PHY-1912764 and PHY-1626069. Work for V1.0 was supported by DOE grants DE-SC0024138 and DE-SC0024914 and NSF grant PHY-2411745. Winklehner was also supported by the Heising-Simons Foundation. Winkler thankfully acknowledges the support from the MIT UROP office.

# Bibliography

- [1] P. Calvo, D. Winklehner, and C. Oliver, “Analyzing beam-gas interactions in an H<sub>2</sub> + cyclotron beam,” en, *Journal of Physics G: Nuclear and Particle Physics*, 2023, ISSN: 0954-3899. DOI: 10.1088/1361-6471/acfe8f. [Online]. Available: <http://iopscience.iop.org/article/10.1088/1361-6471/acfe8f> (visited on 10/11/2023).
- [2] J. R. Alonso, J. M. Conrad, D. Winklehner, *et al.*, “IsoDAR@Yemilab: A report on the technology, capabilities, and deployment,” en, *Journal of Instrumentation*, vol. 17, no. 09, P09042, Sep. 2022, Publisher: IOP Publishing, ISSN: 1748-0221. DOI: 10.1088/1748-0221/17/09/P09042. [Online]. Available: <https://doi.org/10.1088/1748-0221/17/09/p09042> (visited on 09/30/2022).
- [3] S.-H. Seo, J. Alonso, P. Bakhti, *et al.*, *Physics Potential of a Few Kiloton Scale Neutrino Detector at a Deep Underground Lab in Korea*, arXiv:2309.13435 [hep-ex, physics:hep-ph], Sep. 2023. DOI: 10.48550/arXiv.2309.13435. [Online]. Available: <http://arxiv.org/abs/2309.13435> (visited on 10/11/2023).
- [4] J. Alonso, C. A. Argüelles, A. Bungau, *et al.*, “Neutrino physics opportunities with the IsoDAR source at Yemilab,” *Physical Review D*, vol. 105, no. 5, p. 052009, Mar. 2022, Publisher: American Physical Society. DOI: 10.1103/PhysRevD.105.052009. [Online]. Available: <https://link.aps.org/doi/10.1103/PhysRevD.105.052009> (visited on 05/31/2022).
- [5] L. Waites, A. Thompson, A. Bungau, *et al.*, “Axionlike particle production at beam dump experiments with distinct nuclear excitation lines,” *Physical Review D*, vol. 107, no. 9, p. 095010, May 2023, Publisher: American Physical Society. DOI: 10.1103/PhysRevD.107.095010. [Online]. Available: <https://link.aps.org/doi/10.1103/PhysRevD.107.095010> (visited on 05/11/2023).
- [6] M. Abs, A. Adelman, J. R. Alonso, *et al.*, *IsoDAR@KamLAND: A Conceptual Design Report for the Technical Facility*, arXiv: 1511.05130, Nov. 2015. [Online]. Available: <http://arxiv.org/abs/1511.05130> (visited on 05/06/2020).
- [7] J. Stetson, S. Adam, M. Humbel, *et al.*, “The commissioning of PSI injector 2 for high intensity, high quality beams,” in *13th International Conference on Cyclotrons and their Applications*, 1992, p. 4.
- [8] C. Baumgarten, “Transverse-longitudinal coupling by space charge in cyclotrons,” *Physical Review Special Topics-Accelerators and Beams*, vol. 14, no. 11, p. 114201, 2011.
- [9] D. Winklehner, J. M. Conrad, D. Schoen, *et al.*, “Order-of-magnitude beam current improvement in compact cyclotrons,” en, *New Journal of Physics*, vol. 24, no. 2, p. 023038, Feb. 2022, Publisher: IOP Publishing, ISSN: 1367-2630. DOI: 10.1088/1367-2630/ac5001. [Online]. Available: <https://doi.org/10.1088/1367-2630/ac5001> (visited on 03/07/2022).

- [10] D. Winklehner, J. Bahng, L. Calabretta, *et al.*, “High intensity cyclotrons for neutrino physics,” *Nuclear Instruments and Methods in Physics Research Section A: Accelerators, Spectrometers, Detectors and Associated Equipment*, Advances in Instrumentation and Experimental Methods (Special Issue in Honour of Cai Siegbahn), vol. 907, pp. 231–243, Nov. 2018, ISSN: 0168-9002. DOI: 10.1016/j.nima.2018.07.036. [Online]. Available: <http://www.sciencedirect.com/science/article/pii/S0168900218308714> (visited on 10/04/2018).
- [11] M. Hostert, D. McKeen, M. Pospelov, *et al.*, “Dark sectors in neutron-shining-through-a-wall and nuclear absorption signals,” Jan. 2022. arXiv: 2201.02603 [hep-ph].
- [12] A. Bungau, J. Alonso, L. Bartoszek, *et al.*, “Optimizing the  $^8\text{Li}$  yield for the IsoDAR Neutrino Experiment,” en, *Journal of Instrumentation*, vol. 14, no. 03, P03001–P03001, Mar. 2019, Publisher: IOP Publishing, ISSN: 1748-0221. DOI: 10.1088/1748-0221/14/03/P03001. [Online]. Available: <https://iopscience.iop.org/article/10.1088/1748-0221/14/03/P03001> (visited on 08/18/2020).
- [13] A. Bungau, J. Alonso, L. Bartoszek, *et al.*, “The shielding design concept for the ISODAR neutrino target,” en, *Journal of Instrumentation*, vol. 15, no. 07, T07002–T07002, Jul. 2020, Publisher: IOP Publishing, ISSN: 1748-0221. DOI: 10.1088/1748-0221/15/07/T07002. [Online]. Available: <https://iopscience.iop.org/article/10.1088/1748-0221/15/07/T07002> (visited on 08/18/2020).
- [14] J. M. Hardin, I. Martinez-Soler, A. Diaz, *et al.*, “New Clues about light sterile neutrinos: preference for models with damping effects in global fits,” *JHEP*, vol. 09, p. 058, 2023. DOI: 10.1007/JHEP09(2023)058. arXiv: 2211.02610 [hep-ph].
- [15] G. Karagiorgi, B. R. Littlejohn, P. Machado, *et al.*, “Snowmass Neutrino Frontier: NF02 Topical Group Report on Understanding Experimental Neutrino Anomalies,” in *2022 Snowmass Summer Study*, Sep. 2022. arXiv: 2209.05352 [hep-ex].
- [16] A. Diaz, C. A. Argüelles, G. H. Collin, *et al.*, “Where Are We With Light Sterile Neutrinos?” *Phys. Rept.*, vol. 884, pp. 1–59, 2020. DOI: 10.1016/j.physrep.2020.08.005. arXiv: 1906.00045 [hep-ex].
- [17] M. D. J.S. Nico, D. Gilliam, F. E. Wietfeldt, *et al.*, “Measurement of the neutron lifetime by counting trapped protons in a cold neutron beam,” *Phys. Rev. C*, vol. 71, p. 055 502, 2005. DOI: 10.1103/PhysRevC.71.055502. arXiv: nucl-ex/0411041.
- [18] A. T. Yue, M. S. Dewey, D. M. Gilliam, *et al.*, “Improved Determination of the Neutron Lifetime,” *Phys. Rev. Lett.*, vol. 111, no. 22, p. 222 501, 2013. DOI: 10.1103/PhysRevLett.111.222501. arXiv: 1309.2623 [nucl-ex].
- [19] A. P. Serebrov, E. . Kolomensky, A. K. Fomin, *et al.*, “Neutron lifetime measurements with a large gravitational trap for ultracold neutrons,” *Phys. Rev. C*, vol. 97, no. 5, p. 055 503, 2018. DOI: 10.1103/PhysRevC.97.055503. arXiv: 1712.05663 [nucl-ex].
- [20] F. M. Gonzalez *et al.*, “Improved Neutron Lifetime Measurement with UCN $\tau$ ,” *Phys. Rev. Lett.*, vol. 127, no. 16, p. 162 501, 2021. DOI: 10.1103/PhysRevLett.127.162501. arXiv: 2106.10375 [nucl-ex].

- [21] Z. Berezhiani, “A possible shortcut for neutron–antineutron oscillation through mirror world,” *Eur. Phys. J. C*, vol. 81, no. 1, p. 33, 2021. DOI: 10.1140/epjc/s10052-020-08824-9. arXiv: 2002.05609 [hep-ph].
- [22] P. A. Zyla *et al.*, “Review of Particle Physics,” *PTEP*, vol. 2020, no. 8, p. 083C01, 2020. DOI: 10.1093/ptep/ptaa104.
- [23] D. V. Forero and M. M. Guzzo, “Constraining nonstandard neutrino interactions with electrons,” *Phys. Rev. D*, vol. 84, p. 013002, 1 Jul. 2011. DOI: 10.1103/PhysRevD.84.013002. [Online]. Available: <https://link.aps.org/doi/10.1103/PhysRevD.84.013002>.
- [24] T. Stambach, S. Adam, T. Blumer, *et al.*, “The PSI 2mA beam and future applications,” *AIP Conference Proceedings*, vol. 600, no. 1, pp. 423–427, Dec. 2001, ISSN: 0094-243X. DOI: 10.1063/1.1435294. eprint: [https://pubs.aip.org/aip/acp/article-pdf/600/1/423/12144003/423\\_1\\_online.pdf](https://pubs.aip.org/aip/acp/article-pdf/600/1/423/12144003/423_1_online.pdf). [Online]. Available: <https://doi.org/10.1063/1.1435294>.
- [25] S. Axani, D. Winklehner, J. Alonso, *et al.*, “A high intensity H<sub>2</sub><sup>+</sup> multicusp ion source for the isotope decay-at-rest experiment, IsoDAR,” *Review of Scientific Instruments*, vol. 87, no. 2, 02B704, Oct. 2015, Publisher: American Institute of Physics, ISSN: 0034-6748. DOI: 10.1063/1.4932395. [Online]. Available: <https://aip.scitation.org/doi/10.1063/1.4932395> (visited on 03/04/2021).
- [26] D. Winklehner, S. Axani, P. Bedard, *et al.*, “First commissioning results of the multicusp ion source at MIT (MIST-1) for H<sub>2</sub><sup>+</sup>,” in *AIP Conference Proceedings*, vol. 2011, American Institute of Physics, Sep. 2018, p. 030002. DOI: 10.1063/1.5053263. [Online]. Available: <https://aip.scitation.org/doi/abs/10.1063/1.5053263> (visited on 10/11/2022).
- [27] D. Winklehner, J. M. Conrad, J. Smolsky, *et al.*, “High-current H<sub>2</sub><sup>+</sup> beams from a filament-driven multicusp ion source,” *Review of Scientific Instruments*, vol. 92, no. 12, p. 123301, Dec. 2021, Publisher: American Institute of Physics, ISSN: 0034-6748. DOI: 10.1063/5.0063301. [Online]. Available: <https://aip.scitation.org/doi/10.1063/5.0063301> (visited on 01/08/2022).
- [28] D. Winklehner, J. Conrad, J. Smolsky, *et al.*, “New Commissioning Results of the MIST-1 Multicusp Ion Source,” in *Journal of Physics: Conference Series*, vol. 2244, no. 1, p. 012013, Apr. 2022, Publisher: IOP Publishing, ISSN: 1742-6596. DOI: 10.1088/1742-6596/2244/1/012013. [Online]. Available: <https://doi.org/10.1088/1742-6596/2244/1/012013> (visited on 05/31/2022).
- [29] P. Weigel, M. Busza, A. Namazov, *et al.*, “The EPICS control system for IsoDAR,” *Nuclear Instruments and Methods in Physics Research Section A: Accelerators, Spectrometers, Detectors and Associated Equipment*, vol. 1056, p. 168590, Nov. 2023, ISSN: 0168-9002. DOI: 10.1016/j.nima.2023.168590. [Online]. Available: <https://www.sciencedirect.com/science/article/pii/S0168900223005806> (visited on 10/11/2023).
- [30] K. Ehlers and K. Leung, “High-concentration H<sub>2</sub><sup>+</sup> or D<sub>2</sub><sup>+</sup> ion source,” *Review of Scientific Instruments*, vol. 54, no. 6, pp. 677–680, 1983.

- [31] L. Waites, “High Power Cyclotrons: The Bridge Between Beyond the Standard Model Physics, Computation, and Medical Applications,” PhD, Massachusetts Institute of Technology, Cambridge, 2022. [Online]. Available: <https://arxiv.org/abs/2212.11114>.
- [32] T. Kalvas, O. Tarvainen, T. Ropponen, *et al.*, “IBSIMU: A three-dimensional simulation software for charged particle optics,” *Review of Scientific Instruments*, vol. 81, no. 2, 02B703, Feb. 2010, Publisher: American Institute of Physics, ISSN: 0034-6748. DOI: 10.1063/1.3258608. [Online]. Available: <https://aip.scitation.org/doi/full/10.1063/1.3258608> (visited on 08/18/2020).
- [33] J.-L. Vay, D. P. Grote, R. H. Cohen, *et al.*, “Novel methods in the Particle-In-Cell accelerator Code-Framework Warp,” en, *Computational Science & Discovery*, vol. 5, no. 1, p. 014019, Dec. 2012, Publisher: IOP Publishing, ISSN: 1749-4699. DOI: 10.1088/1749-4699/5/1/014019. [Online]. Available: <https://dx.doi.org/10.1088/1749-4699/5/1/014019> (visited on 10/29/2023).
- [34] J. Alonso, S. Axani, L. Calabretta, *et al.*, “The IsoDAR high intensity  $H_2^+$  transport and injection tests,” en, *Journal of Instrumentation*, vol. 10, no. 10, T10003, 2015, ISSN: 1748-0221. DOI: 10.1088/1748-0221/10/10/T10003. [Online]. Available: <http://stacks.iop.org/1748-0221/10/i=10/a=T10003> (visited on 10/16/2018).
- [35] L. Waites, J. Conrad, J. Smolsky, *et al.*, “Matching of an RFQ and Multicusp Ion Source with Compact LEBT,” en, in *Proceedings of the 12th International Particle Accelerator Conference*, Artwork Size: 4 pages, 0.731 MB Medium: PDF, vol. IPAC2021, JACoW Publishing, Geneva, Switzerland, 2021, 4 pages, 0.731 MB, ISBN: 978-3-95450-214-1. DOI: 10.18429/JACOW-IPAC2021-MOPAB159. [Online]. Available: <https://jacow.org/ipac2021/doi/JACoW-IPAC2021-MOPAB159.html> (visited on 11/29/2021).
- [36] L. Waites, J. Conrad, and D. Winklehner, “A Low Energy Beam Transport to Match a Multicusp Ion Source to an RFQ,” en, *Journal of Physics: Conference Series*, vol. 2244, no. 1, p. 012086, Apr. 2022, Publisher: IOP Publishing, ISSN: 1742-6596. DOI: 10.1088/1742-6596/2244/1/012086. [Online]. Available: <https://doi.org/10.1088/1742-6596/2244/1/012086> (visited on 05/31/2022).
- [37] “2562 Notre Dame steering coil 2,” Alpha Magnetics, Inc. (), [Online]. Available: <https://www.alphamag.com/communications-radar-lab-magnets/2562-notre-dame-steering-coil-2/> (visited on 03/07/2025).
- [38] *ACCT: Precise Waveform Measurement of Long Pulses*, <https://www.bergoz.com/products/acct/>, Accessed: 2010-09-30.
- [39] D. Winklehner and D. Leitner, “A space charge compensation model for positive DC ion beams,” *Journal of Instrumentation*, vol. 10, no. 10, T10006, 2015, ISSN: 1748-0221. DOI: 10.1088/1748-0221/10/10/T10006. [Online]. Available: <http://stacks.iop.org/1748-0221/10/i=10/a=T10006> (visited on 10/17/2018).
- [40] U. Ratzinger, H. Podlech, M. Schütt, *et al.*, “Technical Design Report RFQ for IsoDAR,” English, Bevatech, GmbH, Technical Report, 2020, p. 60.





- [50] C. Geuzaine and J.-F. Remacle, “Gmsh: A 3-d finite element mesh generator with built-in pre- and post-processing facilities,” *International Journal for Numerical Methods in Engineering*, vol. 79, pp. 1309–1331, Sep. 2009. DOI: 10.1002/nme.2579.
- [51] W. Smigaj, T. Betcke, S. Arridge, *et al.*, “Solving boundary integral problems with bem++,” *ACM Trans. Math. Softw.*, vol. 41, Feb. 2015. DOI: 10.1145/2590830.
- [52] J. P. Boris, “Relativistic plasma simulation-optimization of a hybrid code,” *Proceeding of Fourth Conference on Numerical Simulations of Plasmas*, Nov. 1970.
- [53] P. Weigel, “Design and Simulation of the IsoDAR RFQ Direct Injection System and Spiral Inflector,” in *Meeting of the APS Division of Particles and Fields*, Oct. 2017. arXiv: 1710.00441 [physics.acc-ph].
- [54] D. Koser, L. Waites, D. Winklehner, *et al.*, “Input beam matching and beam dynamics design optimizations of the isodar rfq using statistical and machine learning techniques,” *Frontiers in Physics*, vol. 10, 2022, ISSN: 2296-424X. DOI: 10.3389/fphy.2022.875889. [Online]. Available: <https://www.frontiersin.org/journals/physics/articles/10.3389/fphy.2022.875889>.
- [55] A. H. Barnard, J. I. Broodryk, J. L. Conradie, *et al.*, “Longitudinal and vertical focusing with a field gradient spiral inflector,” *Phys. Rev. Accel. Beams*, vol. 24, p. 023501, 2 Feb. 2021. DOI: 10.1103/PhysRevAccelBeams.24.023501. [Online]. Available: <https://link.aps.org/doi/10.1103/PhysRevAccelBeams.24.023501>.
- [56] A. Edelen, N. Neveu, M. Frey, *et al.*, “Machine learning for orders of magnitude speedup in multiobjective optimization of particle accelerator systems,” *Phys. Rev. Accel. Beams*, vol. 23, p. 044601, 4 Apr. 2020. DOI: 10.1103/PhysRevAccelBeams.23.044601. [Online]. Available: <https://link.aps.org/doi/10.1103/PhysRevAccelBeams.23.044601>.
- [57] D. Koser, L. Waites, D. Winklehner, *et al.*, “Input Beam Matching and Beam Dynamics Design Optimizations of the IsoDAR RFQ Using Statistical and Machine Learning Techniques,” *Front. in Phys.*, vol. 10, p. 875889, 2022. DOI: 10.3389/fphy.2022.875889. arXiv: 2112.02579 [physics.acc-ph].
- [58] J. Villarreal, D. Winklehner, D. Koser, *et al.*, “Neural networks as effective surrogate models of radio-frequency quadrupole particle accelerator simulations,” *Machine Learning: Science and Technology*, vol. 5, Apr. 2024. DOI: 10.1088/2632-2153/ad3a30.
- [59] M. Conjat and P. Mandrillon, “Central Region studies for the IsoDAR test cyclotron,” AIMA Developpement, Tech. Rep., 2018.
- [60] C. Baumgarten, “Factors Influencing the Vortex Effect in High-Intensity Cyclotrons,” *Proceedings of the 22nd International Conference on Cyclotrons and their Applications*, vol. Cyclotrons2019, 5 pages, 0.661 MB, 2020, Artwork Size: 5 pages, 0.661 MB ISBN: 9783954502059 Medium: PDF Publisher: JACoW Publishing, Geneva, Switzerland. DOI: 10.18429/JACoW-CYCLOTRONS2019-WEB03. [Online]. Available: <http://jacow.org/cyclotrons2019/doi/JACoW-Cyclotrons2019-WEB03.html> (visited on 01/29/2021).
- [61] “Precision Polymer & Metal Seals — Custom Engineering.” (), [Online]. Available: <https://www.omniseal-solutions.com/> (visited on 03/09/2025).

- [62] CST. “CST Microwave Studio - 3D EM Simulation Software.” (), [Online]. Available: <https://www.cst.com/Products/CSTMWS> (visited on 09/01/2015).
- [63] S. H. Vacuum. “Modules UHV.” en-US. (2024), [Online]. Available: <https://www.saesgetters.com/highvacuum/solution/modules-uhv/> (visited on 07/24/2024).
- [64] J.-W. Kim, “Magnetic fields and beam optics studies of a 250 MeV superconducting proton radiotherapy cyclotron,” *Nuclear Instruments and Methods in Physics Research Section A: Accelerators, Spectrometers, Detectors and Associated Equipment*, vol. 582, no. 2, pp. 366–373, 2007. [Online]. Available: <https://www.sciencedirect.com/science/article/pii/S0168900207019262> (visited on 03/07/2025).
- [65] Y. Kim and H. S. Lee, “Yemilab, a new underground laboratory in Korea,” *AAPPS Bulletin*, vol. 34, no. 1, p. 25, Sep. 16, 2024, ISSN: 2309-4710. DOI: 10.1007/s43673-024-00132-8. [Online]. Available: <https://doi.org/10.1007/s43673-024-00132-8> (visited on 03/07/2025).
- [66] Mouvers. “SPMT Voyager.” (2024), [Online]. Available: <https://www.mouvers.it/en/self-propelled-modular-transporter/> (visited on 02/21/2024).
- [67] J. R. Alonso, K. M. Bang, R. Barlow, *et al.*, *IsoDAR@Yemilab: A Conceptual Design Report for the Deployment of the Isotope Decay-At-Rest Experiment in Korea’s New Underground Laboratory, Yemilab*, arXiv:2110.10635 [hep-ex, physics:physics], Dec. 2021. DOI: 10.48550/arXiv.2110.10635. [Online]. Available: <http://arxiv.org/abs/2110.10635> (visited on 02/23/2024).
- [68] *The Present Status of TRIUMF*, vol. Proceedings of 1972 Cyclotron Conference, 1972.
- [69] “GH Cranes.” (), [Online]. Available: <https://www.ghcranes.com/en/> (visited on 02/22/2024).